Summer 9-1-2014

Image Reconstruction in Photoacoustic Computed Tomography with Acoustically Heterogeneous Media

Chao Huang
Washington University in St. Louis

Recommended Citation

Huang, Chao, "Image Reconstruction in Photoacoustic Computed Tomography with Acoustically Heterogeneous Media" (2014). *All Theses and Dissertations (ETDs)*. 1308.
https://openscholarship.wustl.edu/etd/1308

Washington University in St. Louis

School of Engineering and Applied Science

Department of Biomedical Engineering

Dissertation Examination Committee:
Mark Anastasio, Chair
Joseph Culver
James Miller
Joseph O'Sullivan
Robert Pless
Lihong Wang

Image Reconstruction in Photoacoustic Computed Tomography with Acoustically Heterogeneous Media

by

Chao Huang

A dissertation presented to the Graduate School of Arts and Sciences
of Washington University in partial fulfillment of the
requirements for the degree of

Doctor of Philosophy

August 2014
Saint Louis, Missouri

Contents

List of Figures

List of Tables

Acknowledgments

Foremost, I would like to express my sincere gratitude to my advisor, Prof. Mark A. Anastasio, for his advice, encouragement and mentorship. His immense knowledge, high research standard and inspiring guidance have shaped me as a research scientist. This dissertation would not have been possible without his support.

Besides my advisor, I would like to thank the rest of my thesis committee: Prof. Joseph Culver, Prof. James Miller, Prof. Joseph O'Sullivan, Prof. Robert Pless and Prof. Lihong Wang, for their insightful comments and suggestions. Special thanks goes to Prof. Wang, who leads me working on exciting projects and enlightens me as if my co-advisor.

I also would like to thank my fellow labmates in the Computational Bioimaging Laboratory: Dr. Robert Schoonover, Dr. Kun Wang, Dr. Fatima Anis, Dr. Alfred Garson, Mr. Qiaofeng Xu, Mr. Kenji Mitsuhashi, Mr. Yang Lou, and Mr. Huifeng Guan, for the companionship and camaraderie. In particular, I am grateful to Dr. Robert Schoonover and Dr. Kun Wang for the simulating conversation and generous help.

I appreciate the discussions and collaborations with Dr. Liming Nie, Dr. Alejandro Garcia-Uribe, Dr. Konstantin Maslov, Dr. Zijian Guo from the Optical Imaging Laboratory and Dr. Alexander A. Oraevsky, Dr. Sergey A. Ermilov, Mr. Richard Su from the TomoWave Laboratories.

Last but not the least, I would like to thank my parents for their everlasting love, caring and support.

Chao Huang

Washington University in Saint Louis
August 2014

ABSTRACT OF THE DISSERTATION

Image Reconstruction in Photoacoustic Computed Tomography
with Acoustically Heterogeneous Media
by
Chao Huang
Doctor of Philosophy in Biomedical Engineering
Washington University in St. Louis, August 2014
Professor Mark Anastasio, Chair

Photoacoustic computed tomography (PACT), also known as optoacoustic or thermoacoustic tomography, is a rapidly emerging hybrid imaging modality that combines optical image contrast with ultrasound detection. The majority of currently available PACT image reconstruction algorithms are based on idealized imaging models that assume a lossless and acoustically homogeneous medium. However, in many applications of PACT these assumptions are violated and the induced photoacoustic (PA) wavefields are scattered and absorbed as they propagate to the receiving transducers. In those applications of PACT, the reconstructed images can contain significant distortions and artifacts if the inhomogeneous acoustic properties of the object are not accounted for in the reconstruction algorithm. In this dissertation, we develop and investigate a full-wave approach to iterative image reconstruction in PACT with acoustically heterogeneous lossy media. A key contribution of this work is the establishment of a discrete imaging model that is based on the exact PA wave equation and a procedure to implement an associated matched discrete forward and back-projection operator pair, which permits application of a variety of modern iterative image reconstruction algorithms that can mitigate the effects of noise, data incompleteness and model errors. Another key contribution is the development of an optimization approach to joint reconstruction (JR) of absorbed optical energy density and speed of sound in PACT, which is utilized to investigate the numerical properties of the JR problem and its feasibil-ity in practice. We also develop a TR-based methodology to compensate for heterogeneous acoustic attenuation that obeys a frequency power law. In addition, we propose a image reconstruction methodology for transcranial PACT that employs detailed subject-specific descriptions of the acoustic properties of the skull to mitigate skull-induced distortions in the reconstructed image.

Chapter 1

Introduction

1.1 Motivation of the Dissertation

Photoacoustic computed tomography (PACT), also known as optoacoustic or thermoacoustic tomography, is a rapidly emerging hybrid imaging modality that combines optical image contrast with ultrasound detection. [83,155,160,169] In PACT, the to-be-imaged object is illuminated with a pulsed optical wavefield. Under conditions of thermal confinement [42,83], the absorption of the optical energy results in the generation of acoustic wavefields via the thermoacoustic effect. These wavefields propagate out of the object and are measured by use of wide-band ultrasonic transducers. From these measurements, a tomographic reconstruction algorithm is employed to obtain an image that depicts the spatially variant absorbed optical energy density distribution within the object, which will be denoted by the function $A(\mathbf{r})$ in this dissertation. Because the optical absorption properties of tissue are highly related to its hemoglobin concentration and molecular constitution, PACT holds great potential for a wide-range of anatomical, functional, and molecular imaging tasks in preclinical and clinical medicine [25,44,70,160,170].

The majority of currently available PACT reconstruction algorithms are based on idealized imaging models that assume a lossless and acoustically homogeneous medium. However, in many applications of PACT these assumptions are violated and the induced photoacoustic (PA) wavefields are scattered and absorbed as they propagate to the receiving transducers. In small animal imaging applications of PACT, for example, the presence of bone and/or gas pockets can strongly perturb the PA wavefield. Another example is transcranial PACT brain imaging of primates [52], in which the PA wavefields can be strongly aberrated and attenuated [37, 53, 59] by the skull. In these and other biomedical applications of PACT, the reconstructed images can contain significant distortions and artifacts if the inhomogeneous acoustic properties of the object are not accounted for in the reconstruction algorithm.

Several PACT image reconstruction methods have been developed to compensate for the effects of acoustic heterogeneities. Those methods can be categorized into two approaches: ray-based approaches and full-wave approaches. The ray-based approaches are based on a geometrical acoustics (GA) approximation, which utilizes the Eikonal equation to model acoustic wave front propagation. However, the GA approximation is based on the assumption that the length scale of the speed of sound, $c(\mathbf{r})$, variation is much greater than the acoustic wavelength, which can be violated when the media process strong acoustic heterogeneities. The full-wave approaches are based on solutions to the exact wave equation, which permits a broader domain of applicability, they also possess certain practical limitations. For example, finite element methods (FEMs) have intensive computational burden, which is especially problematic for three-dimensional (3D) applications of PACT. Although time-reversal (TR) methods are mathematically exact in their continuous forms in 3D homogeneous media, they are predicated on the assumption that the measurement surface encloses the object, which is often impractical in biomedical applications of PACT. In addition, transducer impulse responses are not readily incorporated into those methods.

In this dissertation, we develop and investigate a full-wave approach to iterative image reconstruction in PACT with acoustically heterogeneous lossy media. A key contribution of this work are the establishment of a discrete imaging model that is based on the exact PA wave equation and a procedure to implement an associated matched discrete forward and backprojection operator pair, which permits application of a variety of modern iterative image reconstruction algorithms that can mitigate the effects of noise, data incompleteness and model errors. Another key contribution is the deveopment of an optimization approach to joint reconstruction (JR) of $A(\mathbf{r})$ and $c(\mathbf{r})$ in PACT, which is utilized to investigate the numerical properties of the JR problem and its feasibility in practice. We also develop a TR-based methodology to compensate for heterogeneous acoustic attenuation that obeys a frequency power law. In addition, we propose a image reconstruction methodology for transcranial PACT that employs detailed subject-specific descriptions of the acoustic properties of the skull to mitigate skull-induced distortions in the reconstructed image.

1.2 Outline of the Dissertation

In Chapter 2, we provide the background knowledge of PACT and lay foundations for later chapters. We review the imaging physics of PACT in its continuous and discrete formulations. We also briefly describe the PACT image reconstruction based on the discrete imaging model and the time-reversal principle.

In Chapter 3, we present an investigation of image reconstruction in PACT with acoustically heterogeneous lossy media. A TR-based reconstrution algorithm is utilized to compensate for acoustic heterogeneity and attenuation that is described by a frequency power law.

In Chapter 4, we develop a subject-specific image reconstruction methodology for transcranial PACT to compensate for aberrations in the measured PA data induced by the skull. Adjunct x-ray CT data are employed to infer the spatially variant SOS and density distributions of the skull, which are subsequently utizlied by the TR image reconstruction algorithm to mitigate skull-induced distortions in the reconstructed image.

In Chapter 5, we develop and investigate a discrete imaging model for PACT that is based on the exact PA wave equation. The k-space pseudospectral method is adopted for implementing the forward and backprojection operators associated with the discrete imaging model. By use of the projection operators, an iterative image reconstruction algorithm is implemented and investigated in computer-simulation and experimental studies of PACT in inhomogeneous acoustic media.

In Chapter 6, we develop an optimization-based reconstruction approach to JR of $A(\mathbf{r})$ and $c(\mathbf{r})$ that is based on the wave equation. The developed reconstruction method is utilized to investigate the numerical properties of the JR problem and its feasibility in practice.

The dissertation concludes with a summary in Chapter 7.

Chapter 2

Background

In this chapter, we review descriptions of photoacoustic wavefield generation and propagation in their continuous and discrete forms. The discrete description is based on the k-space pseudospectral method [24, 82, 144]. We present the pseudospectral k-space method by use of matrix notation, which facilitates the establishment of a discrete PACT imaging model in Chapter 5. We also summarize a discrete formulation of the image reconstruction problem for PACT in acoustically inhomogeneous media. The time-reversal image reconstruction algorithm is reviewed at the end of this chapter. Unless otherwise indicated, lowercase and uppercase symbols in bold font will denote vectors and matrices, respectively.

2.1 Photoacoustic wavefield propagation: Continuous formulation

Let $p(\mathbf{r}, t)$ denote the thermoacoustically-induced pressure wavefield at location $\mathbf{r} \in \mathbb{R}^3$ and time $t \geq 0$. Additionally, let $A(\mathbf{r})$ denote the absorbed optical energy density within the object, $\Gamma(\mathbf{r})$ denote the dimensionless Grueneisen parameter, $\mathbf{u}(\mathbf{r}, t) \equiv (u^1(\mathbf{r}, t), u^2(\mathbf{r}, t), u^3(\mathbf{r}, t))$ denote the vector-valued acoustic particle velocity, $c_0(\mathbf{r})$ denote the medium's SOS distribution, and $\rho(\mathbf{r}, t)$ and $\rho_0(\mathbf{r})$ denote the distributions of the medium's acoustic and ambient densities, respectively. The object function $A(\mathbf{r})$ and all quantities that describe properties of the medium are assumed to be represented by bounded functions possessing compact support.

In many applications, acoustic absorption is not negligible [16, 29, 86, 118, 144]. For a wide variety of lossy materials, including biological tissues, the acoustic attenuation coefficient α can be described by a frequency power law of the form [138]

$$\alpha(\mathbf{r}, f) = \alpha_0(\mathbf{r}) f^y, \tag{2.1}$$

where f is the temporal frequency in MHz, α_0 is the frequency-independent attenuation coefficient in dB MHz^{-y} cm^{-1}, and y is the power law exponent which is typically in the range of 0.9-2.0 in tissues [139].

In a heterogeneous lossy fluid medium in which the acoustic absorption is described by the frequency power law, the propagation of $p(\mathbf{r}, t)$ can be modeled by the following three coupled equations [87, 144]

$$\frac{\partial}{\partial t}\mathbf{u}(\mathbf{r}, t) = -\frac{1}{\rho_0(\mathbf{r})}\nabla p(\mathbf{r}, t), \tag{2.2}$$

$$\frac{\partial}{\partial t}\rho(\mathbf{r}, t) = -\rho_0(\mathbf{r})\nabla \cdot \mathbf{u}(\mathbf{r}, t), \tag{2.3}$$

$$p(\mathbf{r}, t) = c_0(\mathbf{r})^2 \big\{1 - \mu(\mathbf{r})\frac{\partial}{\partial t}(-\nabla^2)^{y/2-1} - \eta(\mathbf{r})(-\nabla^2)^{(y-1)/2}\big\}\rho(\mathbf{r}, t), \tag{2.4}$$

subject to the initial conditions:

$$p_0(\mathbf{r}) \equiv p(\mathbf{r}, t)|_{t=0} = \Gamma(\mathbf{r})A(\mathbf{r}), \qquad \mathbf{u}(\mathbf{r}, t)|_{t=0} = 0, \tag{2.5}$$

where the quantities $\mu(\mathbf{r})$ and $\eta(\mathbf{r})$ describe the acoustic absorption and dispersion proportionality coefficients that are defined as

$$\mu(\mathbf{r}) = -2\alpha_0 c_0(\mathbf{r})^{y-1}, \qquad \eta(\mathbf{r}) = 2\alpha_0 c_0(\mathbf{r})^y \tan(\pi y/2). \tag{2.6}$$

Note that acoustic absorption and dispersion are modeled by the second and third terms in the bracket, which employ two lossy derivative operators based on the fractional Laplacian to separately account for the acoustic absorption and dispersion in a way that is consistent with Eqn. (2.1). When acoustic attenuation can be neglected, $\mu(\mathbf{r}) = 0$ and $\eta(\mathbf{r}) = 0$, and Eqn. (2.4) reduces to

$$p(\mathbf{r}, t) = c_0(\mathbf{r})^2 \rho(\mathbf{r}, t). \tag{2.7}$$

2.2 Photoacoustic wavefield propagation: Discrete formulation

The k-space pseudospectral method can be employed to propagate a photoacoustic wavefield forward in space and time by computing numerical solutions to the coupled equations described by Eqn. (2.2), (2.3), (2.4), and (2.5). This method can be significantly more computationally efficient than real space finite-element and finite-difference methods because it employs the fast Fourier transform (FFT) algorithm to compute the spatial partial derivatives and possesses less restrictive spatial and temporal sampling requirements. Applications of the k-space pseudospectral method in studies of PACT can be found in references [24, 52, 53, 144].

The salient features of the k-space pseudospectral method that will underlie the discrete PACT imaging model are described below. Additional details regarding the application of this method to PACT have been published by Treeby and Cox in references [24, 144]. Let $\mathbf{r}_1, \cdots, \mathbf{r}_N \in \mathbb{R}^3$ specify the locations of the $N = N_1 N_2 N_3$ vertices of a 3D Cartesian grid, where N_i denotes the number of vertices along the i-th dimension. Additionally, let $m\Delta t$, $m \in \mathbb{Z}^*$, $\Delta t \in \mathbb{R}^+$, denote discretized values of the temporal coordinate t, where Z^* and $\mathbb{R}^+$ denote the sets of non-negative integers and positive real numbers. The sampled values of $p(\mathbf{r}, t = m\Delta t)$ and $u^i(\mathbf{r}, t = m\Delta t)$, $i = 1, 2$ or 3, corresponding to spatial locations on the 3D Cartesian grid will be described by the 3D matrices $\mathbf{P}_m$ and $\mathbf{U}^i_m$, respectively, where the subscript m indicates that these quantities depend on the temporal sample index. Unless otherwise indicated, the dimensions of all 3D matrices will be $N_1 \times N_2 \times N_3$. Lexicographically ordered vector representations of these matrices will be denoted as

$$\mathbf{u}^i_m \equiv (u^i(\mathbf{r}_1, m\Delta t), \cdots, u^i(\mathbf{r}_N, m\Delta t))^{\mathrm{T}}, \tag{2.8}$$

and

$$\mathbf{p}_m \equiv (p(\mathbf{r}_1, m\Delta t), \cdots, p(\mathbf{r}_N, m\Delta t))^{\mathrm{T}}. \tag{2.9}$$

The sampled values of the ambient density $\rho_0(\mathbf{r})$ and squared SOS distribution $c_0^2(\mathbf{r})$ will be represented as

$$\mathbf{Q} \equiv \mathrm{diag}(\rho_0(\mathbf{r}_1), \cdots, \rho_0(\mathbf{r}_N)), \tag{2.10}$$

and

$$\mathbf{C} \equiv \mathrm{diag}(c_0^2(\mathbf{r}_1), \cdots, c_0^2(\mathbf{r}_N)), \tag{2.11}$$

where $\mathrm{diag}(a_1, ..., a_N)$ defines a diagonal 2D matrix whose diagonal entries starting in the upper left corner are $a_1, ..., a_N$.

In the k-space pseudospectral method, the 1D discrete spatial derivatives of the sampled fields with respect to the i-th dimension ($i = 1, 2$, or 3) are computed in the Fourier domain as

$$\boldsymbol{\nabla}_i^{\mathrm{Mat}} \mathbf{P}_m \equiv \mathbf{F}^{-1}\{j\mathbf{K}^i \circ \boldsymbol{\kappa} \circ \mathbf{F}\{\mathbf{P}_m\}\}, \tag{2.12}$$

and

$$\boldsymbol{\nabla}_i^{\mathrm{Mat}} \mathbf{U}_m^i \equiv \mathbf{F}^{-1}\{j\mathbf{K}^i \circ \boldsymbol{\kappa} \circ \mathbf{F}\{\mathbf{U}_m^i\}\}, \tag{2.13}$$

where $j \equiv \sqrt{-1}$, the superscript 'Mat' indicates that the 1D discrete derivative operator $\boldsymbol{\nabla}_i^{\mathrm{Mat}}$ acts on a 3D matrix, $\mathbf{F}$ and $\mathbf{F}^{-1}$ denote the 3D forward and inverse discrete Fourier transforms (DFTs), and $\circ$ denotes Hadamard product. The elements of the 3D matrix $\mathbf{K}^i$ ($i = 1, 2, 3$) are given by

$$\begin{aligned}
\mathbf{K}^1_{n_1 n_2 n_3} &= 2\pi \frac{n_1 - 1}{L_1}, \\
\mathbf{K}^2_{n_1 n_2 n_3} &= 2\pi \frac{n_2 - 1}{L_2}, \\
\mathbf{K}^3_{n_1 n_2 n_3} &= 2\pi \frac{n_3 - 1}{L_3},
\end{aligned} \tag{2.14}$$

where $n_i = 1, \cdots, N_i$ ($i = 1, 2, 3$), and L_i denotes the length of the spatial grid in the i-th dimension.

The 3D matrix $\boldsymbol{\kappa} = \mathrm{sinc}(\frac{1}{2}\Delta t c_{\mathrm{min}} \mathbf{K})$ is the k-space operator, where $\mathrm{sinc}(x) = \frac{\sin(x)}{x}$, c_{min} is the minimum of $c_0(\mathbf{r})$, $\mathbf{K}$ is a 3D matrix defined as

$$\mathbf{K} \equiv \sqrt{\sum_{i=1}^{3} \mathbf{K}^i \circ \mathbf{K}^i}, \tag{2.15}$$

and the sinc function and square root function are both element-wise operations.

Consider the operators $\mathbf{\Phi}_i^{\mathrm{Mat}}$ and $\mathbf{\Psi}_i^{\mathrm{Mat}}$ that are defined as

$$\mathbf{\Phi}_i^{\mathrm{Mat}}\mathbf{P}_m \equiv -\Delta t\, \mathbf{Q}^{-1}\boldsymbol{\nabla}_i^{\mathrm{Mat}}\mathbf{P}_m, \tag{2.16}$$

and

$$\mathbf{\Psi}_i^{\mathrm{Mat}}\mathbf{U}_m \equiv -\Delta t\, \mathbf{Q}\boldsymbol{\nabla}_i^{\mathrm{Mat}}\mathbf{U}_m^i. \tag{2.17}$$

It will prove convenient to introduce the $N \times N$ matrices $\mathbf{\Phi}_i$ and $\mathbf{\Psi}_i$ that act on the vector representations of the matrices $\mathbf{P}_m$ and $\mathbf{U}_m^i$, respectively. Specifically, $\mathbf{\Phi}_i$ and $\mathbf{\Psi}_i$ are defined such that $\mathbf{\Phi}_i\mathbf{p}_m$ and $\mathbf{\Psi}_i\mathbf{u}_m^i$ are lexicographically ordered vector representations of the matrices $\mathbf{\Phi}_i^{\mathrm{Mat}}\mathbf{P}_m$ and $\mathbf{\Psi}_i^{\mathrm{Mat}}\mathbf{U}_m^i$, respectively. In terms of these quantities, the discretized forms of Eqn. (2.2), (2.3), and (2.4) can be expressed as

$$\mathbf{u}_{m+1}^i = \mathbf{u}_m^i + \mathbf{\Phi}_i\mathbf{p}_m, \tag{2.18}$$

$$\boldsymbol{\rho}_{m+1}^i = \boldsymbol{\rho}_m^i + \mathbf{\Psi}_i\mathbf{u}_{m+1}^i, \tag{2.19}$$

where $\boldsymbol{\rho}_m^i$ is an $N \times 1$ vector whose elements are defined to be zero for $m = 0$, and

$$\mathbf{p}_{m+1} = \mathbf{C}\sum_{i=1}^{3}\{\boldsymbol{\rho}_{m+1}^i + \mathbf{B}_u\mathbf{u}_{m+1}^i + \mathbf{B}_\rho\boldsymbol{\rho}_{m+1}^i\}. \tag{2.20}$$

The quantities $\mathbf{B}_u\mathbf{u}_{m+1}^i$ and $\mathbf{B}_\rho\rho_{m+1}^i$ in Eqn. (2.20) represent the absorption and dispersion terms in the equation of state. They are defined as lexicographically ordered vector representations of $\mathbf{B}_u^{\mathrm{Mat}}\mathbf{U}_{m+1}^i$ and $\mathbf{B}_\rho^{\mathrm{Mat}}\mathbf{N}_{m+1}^i$, which are defined in analogy to Eqn. (2.4) as

$$\mathbf{B}_u^{\mathrm{Mat}}\mathbf{U}_{m+1}^i \equiv \boldsymbol{\mu}\mathbf{F}^{-1}\left\{\mathbf{K}^{y-2}\mathbf{F}\Big\{\mathbf{Q}\sum_{i=1}^{3}\boldsymbol{\nabla}_i^{\mathrm{Mat}}\mathbf{U}_{m+1}^i\Big\}\right\}, \tag{2.21}$$

$$\mathbf{B}_\rho^{\mathrm{Mat}}\mathbf{N}_{m+1}^i \equiv \boldsymbol{\eta}\mathbf{F}^{-1}\left\{\mathbf{K}^{y-1}\mathbf{F}\Big\{\sum_{i=1}^{3}\mathbf{N}_{m+1}^i\Big\}\right\}, \tag{2.22}$$

where $\mathbf{N}_{m+1}^i$ is the 3D matrix form of $\boldsymbol{\rho}_m^i$, and $\boldsymbol{\mu}$ and $\boldsymbol{\eta}$ are defined as

$$\boldsymbol{\mu} \equiv \mathrm{diag}(\mu_0(\mathbf{r}_1), \cdots, \mu_0(\mathbf{r}_N)), \tag{2.23}$$

$$\boldsymbol{\eta} \equiv \mathrm{diag}(\eta_0(\mathbf{r}_1), \cdots, \eta_0(\mathbf{r}_N)), \tag{2.24}$$

and $\mathbf{K}^{y-2}$ and $\mathbf{K}^{y-1}$ are powers of $\mathbf{K}$ that are computed on an element-wise basis.

2.3 The image reconstruction problem

Here, for simplicity, we neglect the acousto-electrical impulse response (EIR) of the ultrasonic transducers and assume each transducer is point-like. However, a description of how to take into account the transducer responses in PACT image reconstrution will be provided in later chapters. With these assumptions, we can define $\hat{\mathbf{p}}_m \equiv (p(\mathbf{r}_1^d, m\Delta t), \cdots, p(\mathbf{r}_L^d, m\Delta t))^{\mathrm{T}}$ as the measured pressure wavefield data at time $t = m\Delta t$ ($m = 0, \cdots, M-1$), where M is the total number of time steps and $\mathbf{r}_l^d \in \mathbb{R}^3$ ($l = 1, \cdots, L$) denotes the positions of the L ultrasonic transducers that reside outside the support of the object. The PACT image reconstruction problem we address is to obtain an estimate of $p_0(\mathbf{r})$ or, equivalently, $A(\mathbf{r})$, from knowledge of $\hat{\mathbf{p}}_m$, $m = 0, \cdots, M-1$, $c_0(\mathbf{r})$, $\rho_0(\mathbf{r})$, $\alpha_0(\mathbf{r})$, and y. The development of image reconstruction methods for addressing this problem is an active area of research [24, 50, 52, 54, 133].

2.3.1 Image reconstruction based on discrete formulation

The discrete form of the imaging model for PACT can be expressed generally as

$$\hat{\mathbf{p}} = \mathbf{H}\mathbf{A}, \tag{2.25}$$

where the $LM \times 1$ vector

$$\hat{\mathbf{p}} \equiv \begin{bmatrix} \hat{\mathbf{p}}_0 \\ \hat{\mathbf{p}}_1 \\ \vdots \\ \hat{\mathbf{p}}_{M-1} \end{bmatrix}, \tag{2.26}$$

represents the measured pressure data corresponding to all transducer locations and temporal samples, and the $N \times 1$ vector $\mathbf{A}$ is the discrete representation of the sought-after absorbed optical energy density distribution $A(\mathbf{r})$ within the object. The $LM \times N$ matrix $\mathbf{H}$ represents the discrete imaging operator, also referred to as the system matrix.

The image reconstruction task is to determine an estimate of $\mathbf{A}$ from knowledge of the measured data $\hat{\mathbf{p}}$. This can be accomplished by computing an appropriately regularized inversion of Eqn. (2.25). When iterative methods are employed to achieve this by minimizing a penalized least squares cost function [35], the action of the operators $\mathbf{H}$ and its adjoint $\mathbf{H}^\dagger$ must be computed. Methods for implementing these operators are described in Chapter 5.

2.3.2 Image reconstruction based on time-reversal

Alternatively, when the measured PA signals are densely sampled on a measurement surface that encloses the object, the time-reversal algorithm can be employed to reconstruct images in PACT [50, 143]. The reconstruction algorithm operates by iteratively solving Eqn. (2.18) - (2.20) backward in time with initial and boundary conditions specified as:

$$\mathbf{u}_M^i = \mathbf{0}_{N\times 1}, \quad \mathbf{p}_M = \hat{\mathbf{p}}_M, \quad \boldsymbol{\rho}_M^i = \frac{1}{3}\mathbf{C}^{-1}\mathbf{p}_M, \quad \mathbf{p}_m = \hat{\mathbf{p}}_m, \tag{2.27}$$

where $i = 1, 2, 3$, $\mathbf{0}_{N\times 1}$ is $N \times 1$ zero vector.

The time-reversal reconstruction algorithm is based on a full-wave solution to the acoustic wave equation for heterogeneous lossy media, and can therefore compensate for scattering due to variations in SOS and mass density. It can also compensate for acoustic absorption and dispersion by reversing the absorption proportionality coefficient μ in sign but leaving the equivalent dispersion parameter η unchanged during reconstruction [143].

Chapter 3

Photoacoustic Computed Tomography Correcting for Heterogeneity and Attenuation

3.1 Introduction

The thermoacoustically-induced pressure signals measured in PACT are broadband and acoustic attenuation is frequency-dependent. It has been demonstrated [118] that the fidelity of reconstructed images can degrade if acoustic attenuation is not compensated for in the PACT reconstruction algorithm. However, relatively few tomographic reconstruction algorithms are available for such compensation for acoustic attenuation [16, 29, 86, 118, 144]. Moreover, all of the previously investigated methods have assumed that the acoustic attenuation properties of the object are homogeneous. An important biomedical application in which that assumption will be grossly violated is transcranial PACT [90], in which the models of acoustic attenuation in soft-tissue and skull bone have distinct forms.

In this chapter, we report an investigation of PACT reconstruction of optical absorbers embedded in a heterogeneous, lossy medium. A time-reversal-based reconstruction algorithm described in Section 2.3.2, which was previously demonstrated for media possessing homogeneous acoustic absorption properties, is modified for acoustically heterogeneous and lossy acoustic media obeying a power law attenuation model. As described below, in general the attenuation coefficient component of the power law is permitted to be spatially variant, while the power law exponent is required to be constant. When the object contains materials, such as bone and soft-tissue, that are modeled using power law attenuation models with distinct exponents, we demonstrate that the effects of acoustic attenuation due to the most strongly attenuating material (e.g., bone) can be compensated for if the attenuation due to the other less attenuating material(s) (e.g., soft-tissue) is neglected. Experiments with phantom objects are conducted to corrorborate our findings.

3.2 Compensation for Heterogeneous Absorption

We employed the time-reversal image reconstruction algorithm described in Section 2.3.2 to compensate for acoustic attenuation corresponding to the power law model. However, the original implementation of the time-reversal algorithm can only compensate for homogeneous acoustic attenuation [143]; i.e. the acoustic attenuation is described by a fixed power law with a constant attenuation coefficient α_0 and power law exponent y.

We modified the original implementation of the k-space model for use with heterogeneous lossy media. Specifically, two modifications were implemented: (1) The k-space adjustment parameter κ in Eq. (15) in Ref. [144] was removed. This parameter is not required because the equation of state [Eq. (2.4)] does not involve temporal derivatives, and k-space adjustment is only used to improve the stability and accuracy of the computation of temporal derivatives in the k-space method; and (2) The implementation was modified to permit α_0 in Eq. (2.6) to be a spatially varying quantity $\alpha_0(\mathbf{r})$ [1].

Note that although $\alpha_0(\mathbf{r})$ can be spatially variant, the power law exponent y is required to be a constant in the k-space time-reversal method. When the object is composed of soft tissues, the assumption of a constant power law exponent is justified. However, when the object contains regions corresponding to distinct power law exponents, which occurs, for example, in the presence of both bone and soft-tissue, the reconstruction method must be modified to avoid image blurring and distortions due to use of a fixed power law exponent. When acoustic attenuation of a single power law exponenet is dominant, e.g., the skull attenuation in transcranial PACT, we propose a simple strategy for circumventing this problem. Namely,

---

[1] Those modifications have been incorporated into the latest version of k-Wave.

the acoustic attenuation effects due to the most strongly attenuating component (e.g., bone) can be compensated for by use of the correct power law parameters, while the less important attenuation effects due to the other components(s) are neglected. Let V_s denote the region of support of the most strongly attenuating object component and let $\alpha_{0,s}(\mathbf{r})$ and y_s denote the quantities that specify the power law in Eq. (2.1) for this component. If one specifies $y = y_s$ and $\alpha_0(\mathbf{r}) = \alpha_{0,s}(\mathbf{r})$ for $\mathbf{r} \in V_s$ and $\alpha_0(\mathbf{r}) = 0$ otherwise, the k-space time-reversal reconstruction method described above will compensate for acoustic attenuation resulting from the most strongly attenuating component.

3.3 Computer Simulations

To corroborate the correctness of the modified wave solver code for use with acoustically heterogeneous, lossy media, a computer-simulation study was conducted. The modified wave solver was employed to simulate the propagation of a monopolar pulsed acoustic plane-wave through a one-dimensional heterogeneous lossy medium. The assumed propagation medium consisted of an acoustically absorbing structure of length $L = 10$ mm that was embedded in an infinite homogeneous lossless medium with a SOS and density corresponding to water at room temperature. The SOS and density of the absorbing structure were 3000 m s^{-1} and 2000 kg m^{-3}, and its acoustic attenuation was assumed to be described by the power law $\alpha_s(f) = \alpha_{0,s} f^{y_s}$ with $\alpha_{0,s} = 1$ dB MHz^{-y_s} cm^{-1} and $y_s = 1.5$. When solving Eqs. (2.2)-(**??**) the k-space wave solver employed a computational grid of dimension 1×512 pixels (51.2 mm), a time step of 1 ns, and a total simulation time of 40 μs.

The pressure wavefield that was propagated through the acoustically inhomogeneous medium was computed as a function of time at the edge of the computational grid. Samples of the magnitude of its 1D Fourier transform $A_s(f)$ were computed by use of the discrete Fourier transform. The pressure wavefield was also computed at the same location for the case when the acoustic heterogeniety was absent, with the corresponding Fourier magnitude spectrum being denoted as $A_w(f)$. The frequency-dependent attenuation coefficient was estimated from the simulated measurements as [47]:

$$u(f) = \alpha_s(f) - \alpha_s(f_0) = \frac{1}{L}\ln\left[\frac{A_w(f)A_s(f_0)}{A_s(f)A_w(f_0)}\right], \tag{3.1}$$

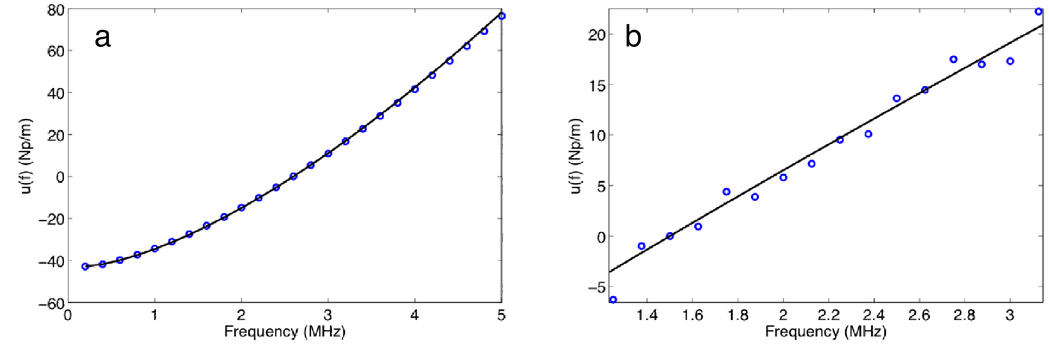

Figure 3.1: (Color online) A plot of the simulated data function $u(f)$ (blue circles) and the expected function $u^*(f)$ (solid line) from 0 to 5 MHz (panel a). This curve corresponds to $\alpha_0 = 1$ dB MHz^{-y} cm^{-1} and $y = 1.5$. A plot of the experimentally determined data function $u(f)$ (blue circles) and the best fit curve (solid line) (panel b). This curve corresponds to α_0 = 1.3 dB MHz^{-y} cm^{-1} and $y = 0.9$.

where f_0 is a reference frequency. The estimated $u(f)$ and the corresponding true values given by $u_{true}(f) = \alpha_0(f^y - f_0^y)$ were plotted together in Fig. 3.1(a) and found to be nearly identical. The mean square error between the curves was 0.48.

3.4 Experimental Validation

An experimental PACT study was conducted to demonstrate the use of the modified time-reversal image reconstruction method for use with acoustically heterogeneous, lossy media. A well-characterized phantom, displayed in Fig. 3.2, represented the to-be-imaged object. The phantom contained 6 optically absorbing structures (pencil leads) embedded in agar. These structures were surrounded by an acrylic cylinder that had inner and outer radii of 7.1 and 7.6 cm, respectively, and a height of 3 cm. The density and SOS of the acrylic were measured and found to be 1200 kg m^{-3} and 3100 m s^{-1}.

The optical absorbers and acrylic cylinder were immersed in water and irradiated by a laser beam from the top. Light from a tunable dye laser (NS, Sirah), pumped by a Q-switched Nd:YAG laser (PRO-350-10, Newport) at 630 nm was used as the illumination source, and the incident laser fluence on the target surface was 8 mJ/cm^2 with a 10 Hz pulse repetition rate.

Figure 3.2: (Color online) A photograph of the pencil leads held in agar and surrounded by an acrylic cylindrical shell.

The photoacoustic (PA) signals were detected by use of a single ultrasound transducer that was scanned along a circular trajectory of radius 9.5 cm. The transducer was cylindrically focused and therefore the reconstruction problem was treated as a two-dimensional (2D) one. The photoacoustic signals were recorded with 20 MHz sampling rate at 1000 equally spaced locations on the scanning circle and were amplified by a 50-dB amplifier (5072 PR, Panametrics, Waltham, MA). It has been demonstrated that the 2D time reversal algorithm can yield accurate reconstructed images if the maximum time of signal recording time T is sufficiently large [50]. Therefore, 20,000 temporal samples were acquired at each recording location to ensure that the magnitudes of the PA signals at the cut-off time T were sufficient small (approximately at the noise level).

In the image reconstruction procedure we sought to compensate for acoustic attenuation of the PA signals due to the the acrylic cylinder, which represented the dominant acoustic absorber in the object. To determine the absorption parameters α_0 and y of acrylic, a transmission experiment was conducted by use of a modified broadband through-transmission technique proposed by He [47]. A flat acrylic specimen of thickness 11 mm was employed, whose composition was identical to the acrylic cylinder. The transmitting and receiving transducers employed were both Panametrics V306, having a central frequency of 2.25 MHz with a bandwidth of 70%. From transmission measurements with and without the acrylic specimen present, the corresponding amplitude spectra $A_w(f)$ and $A_s(f)$ were computed and used to calculate the measured values $u(f)$ in Eq. (3.1). A nonlinear least squares method was used to fit the measured data to the frequency power law. Figure 3.1(b) displays the measured values $u(f)$ (blue circles) and the fitted curve $u^*(f)$ (solid line). The estimated absorption parameters were found to be $\alpha_0 = 1.3$ dB MHz^{-y} cm^{-1} and $y = 0.9$.

For use in the time-reversal reconstruction code, the 2D SOS map $c_0(\mathbf{r})$, density map $\rho_0(\mathbf{r})$, and attenuation coefficient $\alpha_0(\mathbf{r})$ were constructed. The maps $c_0(\mathbf{r})$ and $\rho_0(\mathbf{r})$ were assigned the values for acrylic within the annular region occupied by that material and assigned the values 1480 m s^{-1} and 1000 kg m^{-3} elsewhere. Similarly, the map $\alpha_0(\mathbf{r})$ was assigned the value $\alpha_0 = 1.3$ dB MHz^{-y} cm^{-1} within the annular region occupied by the acrylic and was set to zero elsewhere, reflecting that we neglected the relatively weak acoustic attenuation due to the water bath and agar. The power law exponent was set at $y = 0.9$, as determined above.

The measured PA signals were pre-processed by a curvelet denoising technique prior to application of the image reconstruction algorithm. The images were reconstructed on a grid of 500×500 pixels of dimension 0.5 mm. To mitigate noise amplification in the reconstructed images, the time-reversed pressure signals were subjected to a low-pass filter specified by a tapered cosine window. The filter cutoff frequency corresponded to the frequency at which the value of average power spectrum of PA signals matched the noise level.

Two additional images were reconstructed to demonstrate the relative importance of compensating for the SOS and density heterogeneities vs. acoustic attenuation. One image was reconstructed by employing a constant SOS value of 1520 m s^{-1} and constant density value of 1000 kg m^{-3} in the reconstruction algorithm, but propertly compensated for the attenuation in the acrylic cylinder. The second image was reconstructed by properly incorporating the spatially variant SOS and density distributions in the reconstruction algorithm, but ignored acoustic attenuation.

The reconstructed images are displayed in Fig. 3.3. Figure 3.3(a) displays the reference image corresponding to the case where the acrylic cylinder was absent. Figures 3.3(b)-(d) display images of the phantom when the acrylic cylinder was present: Fig. 3.3(b) displays the image obtained by assuming the constant SOS and mass density values described above but compensating for the acoustic attenuation due to the acrylic; Fig. 3.3(c) displays the image reconstructed by properly compensating for the spatially variant SOS and density distributions but neglecting acoustic attenuation; The image in Fig. 3.3(d) was reconstructed

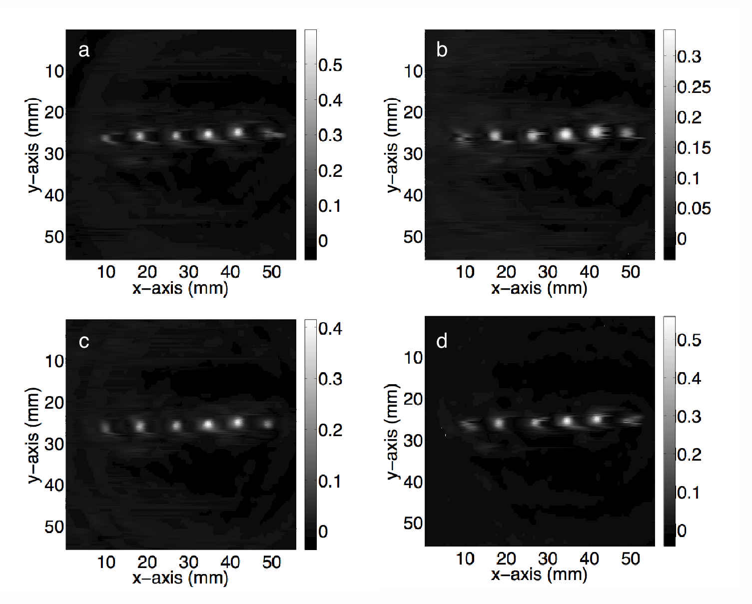

Figure 3.3: The reconstructed image depicting the six optical absorbers in four cases: (a) the acrylic shell was absent during imaging (reference image); (b) the acrylic shell was present and the SOS and density heterogeneities were ignored in the reconstruction method but acoustic attenuation was compensated for; (c) the acrylic shell was present and the SOS and density heterogeneities were compensated for in the reconstrution method but the acoustic attenuation was ignored; and (d) the acrylic shell was present and the SOS and density heterogeneities and acoustic attenuation were compensated for in the reconstruction method.

by properly compensating for both the spatially variant SOS and density distributions and acoustic attenuation due to the acrylic cylinder.

We found that compensation for SOS and density heterogenties without attenuation compensation Fig. 3.3(c) yields better spatial resoultion than compensation for only attenuation Fig. 3.3(b). Specifically, the average full-width-at-half-maximum (FWHM) of the optical absorbers in Fig. 3.3(c) was 25% less than the average FWHM in Fig. 3.3(b). These results confirm that, for the object studied, SOS and mass density heterogeneities influence the reconstructed image more strongly than acoustic attenuation [29]. However, as expected, Fig. 3.3(d) reveals that compensation for both SOS and density heterogeneties along with acoustic attenuation yields the image that possesses the best spatial resolution. This is most noticeable for the optical absorber closest to the acrylic cylinder (far left absorber in the reconstructed images). For that structure, the FWHM in the vertical direction was further

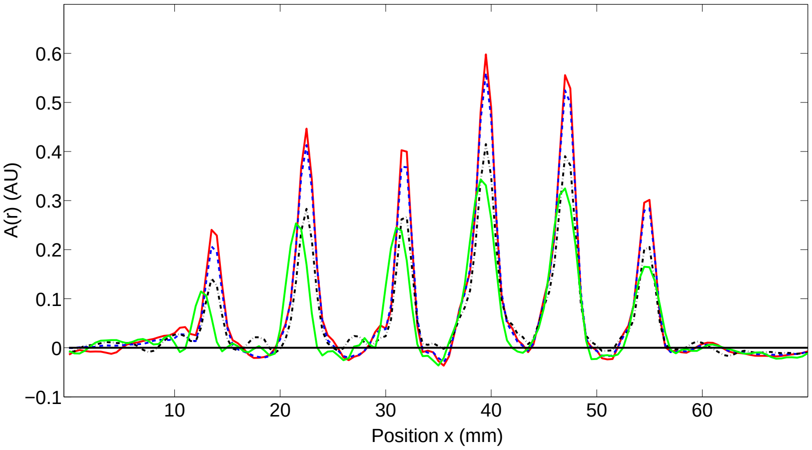

Figure 3.4: Profiles through the centers of the reconstructed images. The profiles depicted as solid red, solid green, dotted black, and dashed blue lines correspond to the images in Fig. 3.3(a)-(d), respectively.

reduced by 40% over the FWHM corresponding to Fig. 3.3(c). This can be explained by the fact that the average acoustic path length through the acrylic cylinder for PA waves generated from the optical absorber closest to the cylinder is longer than for PA waves generated from the other optical absorbers.

Profiles through the centers of the reconstructed images are displayed in in Fig. 3.4. The profiles denoted by solid red, solid green, dotted black, and dashed blue lines correspond to the images in Fig. 3.3(a)-(d), respectively. The averaged peak magnitude of the six optical absorbers in the reconstructed image with compensation of both SOS and density heterogeneities along with acoustic attenuation (dashed blue line) is 92% of that corresponding to the reference image (solid red line). The averaged peak magnitude in the reconstructed image that compensated only for SOS and density heterogeneities and neglected acoustic attenuation (dotted black line) was 64% of the averaged peak magnitude in the reference image (solid red line), while the reconstructed image that only compensated for acoustic attenuation (solid green) was 57% of that corresponding to the reference image. One notes that in the reconstructed image that only compensates for attenuation (solid green), not only is the peak magnitude underestimated, but the peak positions are also shifted as compared to the reference image. These shifts are larger for the optical absorbers closer to the acrylic cylinder. This demonstrates that, even for relatively simple heterogenous SOS distributions, using a constant effective SOS value in the reconstruction algorithm can result in image distortions.

3.5 Summary

In this chapter, we investigated the use of a time-reversal algorithm for PACT image reconstruction that can compensate for acoustic attenuation in heterogeneous lossy acoustic media. For applications in which acoustic attenuation in a multi-component object is described by frequency power laws having distinct exponents, we demonstrated that the acoustic attenuation due to the most strongly attenuating component can be effectively compensated for. The transmission experiment outlined in this chapter to estimate the acoustic attenuation properties of the cylinder is impractical for in-vivo imaging applications. In that case, adjunct imaging data, such as a CT image of the skull [9, 108], may provide a means of estimating $\alpha(\mathbf{r}, f)$, as well as information about the skull geometry, for use with the time-reversal algorithm. Our findings will facilitate the further development of PACT for important applications including transcranial brain imaging, which will be described in the next chapter.

Chapter 4

Aberration Correction for Transcranial PACT of Primates

4.1 Introduction

Transcranial brain imaging represents an important application that may benefit significantly by the development of PACT methods. Existing high-resolution human brain imaging modalities such as X-ray computed tomography (CT) and magnetic resonance imaging (MRI) are expensive and employ bulky and generally non-portable imaging equipment. Moreover, X-ray CT employs ionizing radiation and is therefore undesirable for use with patients who require frequent monitoring of brain diseases or injuries. Ultrasonography is an established portable pediatric brain imaging modality, but its image quality degrades severely when employed after the closure of the fontanels. The photoacoustic (PA) signals recorded in a PACT experiment experience only a one-way transmission through the skull. Accordingly, they are generally less attenuated and aberrated than the echo data recorded in transcranial ultrasound imaging, which are contaminated by the the effects of a two-way transmission through the skull. Moreover, a majority of the broadband PA signal energy resides at frequencies less than 1 MHz, and these relatively low-frequencies interact less strongly with skull bone [37] than do higher frequency ultrasound beams that are typically employed in pure ultrasound imaging.

Transcranial PACT studies have revealed structure and hemodynamic responses in small animals [156, 170] and anatomical structure in human infant brains have been conducted [59, 90, 167, 170, 172]. Because the skulls in those studies were relatively thin ($\sim$1 mm), they did not significantly aberrate the PA signals and conventional backprojection methods were employed for image reconstruction. However, PA signals can be significantly aberrated by thicker skulls present in adolescent and adult primates. To render PACT an effective modality for use with transcranial imaging in large primates, including humans, it is necessary to develop image reconstruction methodologies that can accurately compensate for skull-induced aberrations of the recorded PA signals.

Towards this goal, Xing *et al.* [59] proposed an image reconstruction method that sought to compensate for PA signal aberration associated with acoustic wave reflection and refraction within the skull. In that method, the skull was assumed to be acoustically homogeneous. Accordingly, the method could not explicitly account for scattering effects that arise from heterogeneities in the skull. As a result of the simplified skull model employed, only modest improvements in image quality were observed as compared to use of a standard backprojection-based reconstruction algorithm. Therefore, there remains an important need for the development of improved image reconstruction methodologies for transcranial PACT that are based upon more accurate models of the skull's heterogeneous acoustic properties.

In this chapter, we propose and investigate a reconstruction methodology for transcranial PACT that employs detailed subject-specific descriptions of the acoustic properties of the skull to mitigate skull-induced blurring and distortions in the reconstructed image. The reconstruction methodology is comprised of two primary steps. In the first step, the spatially varying speed-of-sound (SOS) and mass density distributions of the to-be-imaged subject's skull are determined by use of adjunct X-ray CT data. This is accomplished by use of a method that was developed previously to facilitate transcranial adaptive acoustic focusing for minimally invasive brain surgery [9]. In the second step, the subject-specific SOS and density distributions are employed with a time-reversal image reconstruction method [144] for estimation of the spatially variant initial amplitude of the thermoacoustically-induced pressure signals within the brain.

The chapter is organized as follows. In Section 4.2, the image reconstruction methodology is given, which includes a description of how the SOS and density maps of a skull are computed from adjunct X-ray CT data. Section 4.3 gives the description of the image reconstruction studies that employ a well-characterized phantom and a primate brain, both enclosed in a skull. Section 4.4 describes the results of the image reconstruction studies The chapter concludes with a summary and discussion of future work in Section 4.5.

4.2 Image reconstruction methodology

Our methodology for aberration correction in transcranial PACT image reconstruction is comprised of two primary steps. First, the spatially varying SOS and density distributions of the to-be-imaged subject's skull are determined by use of adjunct X-ray CT data. These distributions are subsequently employed with the time-reversal image reconstruction method [144] described in Section 2.3.2 for estimation of absorbed optical energy density distribution within the brain tissue from knowledge of the measured data.

4.2.1 Estimation of the skull's SOS and mass density distributions from CT data

The wavefront aberration problem encountered in transcranial PACT is conjugate to one encountered in transcranial focusing of high-intensity ultrasound [22, 137, 142] for therapy applications. Both problems involve a one-way propagation of ultrasound energy through the skull and both require that the wavefront aberrations induced by the skull be corrected. The problems differ in the direction of the propagating acoustic wavefields. The feasibility of utilizing skull information derived from adjunct X-ray CT image data to correct for wavefield aberrations in transcranial focusing applications has been demonstrated [9]. As described below, we adopted this method for determining estimates of $c_0(\mathbf{r})$ and $\rho_0(\mathbf{r})$, characterizing the acoustic properties of subject's skull, from adjunct X-ray CT data.

Theory: As described by Aubry, *et al.* [9], the SOS and density maps of the skull can be estimated from a porosity map using mixture laws in a biphasic medium (bone/water). Let H_k denote the value of the *k-th* voxel in the X-ray CT image, which is measured in Hounsfield Units. A voxel-based representation of the porosity map, denoted as Φ_k, can be established from knowledge of H_k as [9,107]

$$\Phi_k = 1 - \frac{H_k}{H_k^{Max}}, \tag{4.1}$$

where H_k^{Max} is the maximum value of H in the CT image.

Let ρ_k and c_k denote voxel-based representations of the skull's mass density and SOS distributions. The density map ρ_k can be estimated from the porosity map as

$$\rho_k = \Phi_k \rho^w + (1 - \Phi_k)\rho^s, \tag{4.2}$$

where $\rho^w = 1000$ kg/m^3 is the density of water, and $\rho^s = 2100$ kg/m^3 is the density of skull as determined by ultrasound experiments [9,37]. According to Carter and Hayes [17], the elastic modulus of bone is proportional to the apparent density cubed as a first order approximation. This suggests a linear relationship between the speed of sound and the porosity:

$$c_k = \Phi_k c^w + (1 - \Phi_k)c^s, \tag{4.3}$$

where $c^w = 1480$ m/s is the speed of sound in water, and $c^s = 2900$ m/s is the speed of sound of skull bone as determined by previous ultrasound experiments [9,37].

Experimental methods: The monkey skull phantom described in Section 4.3.1 was imaged using an X-ray CT scanner (Philips Healthcare, Eindhoven, The Netherlands) located at Washington University in St. Louis. Details regarding this system can be found in reference [121]. Prior to imaging, three fiducial markers were attached to the skull to facilitate co-registration of the determined SOS and density maps with the reference frame of the PACT imaging system. The three fiducial markers (see Fig. 4.1-(a)) were iron balls of diameter of 1.5 mm, and were carefully attached to the outer surface of the skull. The fiducial markers were located in a transverse plane that corresponded to the to-be-imaged 2D slice in the PACT imaging studies described below. In the X-ray CT studies, the tube voltage was set at 130 kV and a tube current of 60 μA was employed. Images were reconstructed on a grid of 700 by 700 pixels of dimension $d = 0.1$ mm. This pixel size is much less than the smallest wavelength (0.5 mm) detected by the ultrasound transducer used in the PACT imaging studies described below. This precision is sufficient to to accurately model acoustic

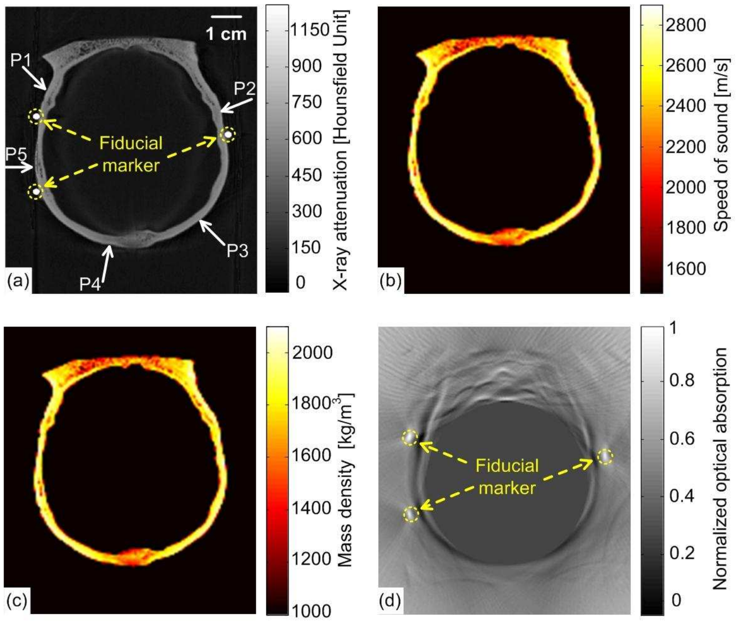

Figure 4.1: (a) A two dimensional slice through the PA imaging plane of the CT of the skull with fiducial markers labeled. (b & c)Speed of sound and density maps derived from the CT data using Eqs. (4.3) and (4.2) in the PA imaging plane. (d) The PACT image of monkey head phantom (with brain present) reconstructed by use of the half-time algorithm

wave propagation in the skull by using the k-space pseudospectral methods [24, 144]. The reconstructed CT image is displayed in Fig. 4.1(a).

From knowledge of the CT image, the porosity map Φ_k was computed according to Eqn. (4.1). Subsequently, the density and SOS maps ρ_k and c_k were computed according to Eqns. (4.2) and (4.3). Images of the estimated c_k and ρ_k maps are displayed in Figs. 4.1-(b) and (c). To corroborate the accuracy of the adopted method for estimating the skull's SOS and density distributions from X-ray CT data (i.e., Eqns. (4.2) and (4.3)), direct measurements, of the skull's average SOS along ray-paths perpendicular to the skull surface at five locations were acquired. This was accomplished by use of a photoacoustic measurement technique depicted in Fig. 4.2-(a). Additionally, the average density of the skull was computed and compared to the average computed from the values estimated from the X-ray CT data. The results show that the directly measured average SOS and density are very close (about 1-6%) to the estimated values from CT data. These results corrorborate the adopted method for estimating the skull's SOS and density distributions from adjunct X-ray CT data. Details regarding these studies are contained in the Appendix A.

4.2.2 Image reconstruction

Image reconstruction was accomplished in two steps: (1) Registration of the SOS and density maps of the skull to the PACT coordinate system; and (2) Utilization of a time-reversal method for PACT image reconstruction in the corresponding acoustically heterogeneous medium.

The estimated SOS and density maps c_k and ρ_k were registered to the frame-of-reference of the PACT imaging as follows. From knowledge of the PACT measurement data, a scout image was reconstructed by use of a half-time reconstruction algorithm [7]. This reconstruction algorithm can mitigate certain image artifacts due to acoustic aberrations, but the resulting images will, in general, still contain significant distortions. The PACT image of monkey head phantom (with brain present) reconstructed by use of the half-time algorithm is displayed in Fig. 4.1(d). Although the image contains distortions, the three fiducial markers are clearly visible. As shown in Fig. 4.1(a), the fiducial markers were also clearly visible in the X-ray CT image that was employed to estimate the SOS and density maps of the skull. The centers of the fiducial markers in the X-ray CT and PACT images were determined manually. From this information, the angular offset of the X-ray CT image relative to the PACT image was computed. The SOS and density maps were downsampled by a factor of two, to match the pixel size of the PACT images, and rotated by this angle to register them with the PACT images.

The re-orientated SOS and density maps were employed with the k-space time-reversal PACT image reconstruction algorithm described in Section 2.3.2. The numerical implementation of this algorithm provided in the Matlab k-Wave Toolbox [143] was employed. The measured PA signals were pre-processed by a curvelet denoising technique prior to application of the image reconstruction algorithm [132]. The absorbed optical energy density distribution $\mathbf{A}$ was reconstructed on a grid of 1000 × 1000 pixels of dimension 0.2 mm. For comparison, images were also reconstructed on the same grid by use of the back-projection reconstruction algorithm. This procedure was repeated to reconstruct images of both phantoms and the corresponding control phantoms (phantoms with skulls removed).

4.3 Image reconstruction studies

4.3.1 Description of biological phantoms

Two biological phantoms that employed a monkey skull were employed in the experimental studies. The first phantom was the head of an 8 month old rhesus monkey that was obtained from the Wisconsin National Primate Research Center. The hair and scalp were removed from the skull. A second, more simple, phantom was constructed by removing the brain of the monkey and replacing it by a pair of iron needles of diameter 1 mm that were embedded in agar. This was accomplished by cutting off the calvaria to gain access to the brain cavity.

4.3.2 PACT imaging studies: Data acquisition

After the skull's SOS and density distributions were estimated from the adjunct X-ray CT data, the two phantoms (that included the skulls) were imaged by use of a PACT imaging system in the Optical Imaging Laboratory, as shown in Fig. 4.2(b). Images of the two phantoms with the skull removed, i.e., images of the extracted monkey brain and crossed needles embedded in agar, were also acquired, which will serve as control images. The imaging system employed a 2D scanning geometry and has been employed in previous studies of PACT imaging of monkey brains. [90] The imaging plane and fiducial markers were chosen to be about 2 cm below the top of the skull, such that the imaging plane was approximately normal to the skull surface at that plane. The phantoms (crossed needles and the primate cortex) were moved to the imaging plane,so that the amount of acoustic energy refracted out of the imaging plane was minimized. Additionally, the system was aligned to ensure the scanning plane and the imaging plane coincided.

The phantoms were immersed in a water bath and irradiated by use of a tunable dye laser from the top (through the skull for the cases when it was present) to generate PA signals. The laser (NS, Sirah), was pumped by a Q-switched Nd:YAG laser (PRO-350-10, Newport), operating at a wavelength of 630 nm with a pulse repetition rate of 10 Hz, was employed as the energy source. The laser beam was expanded by use of a piece of concave lens and homogenized by a piece of ground glass before illuminating the target. The energy density

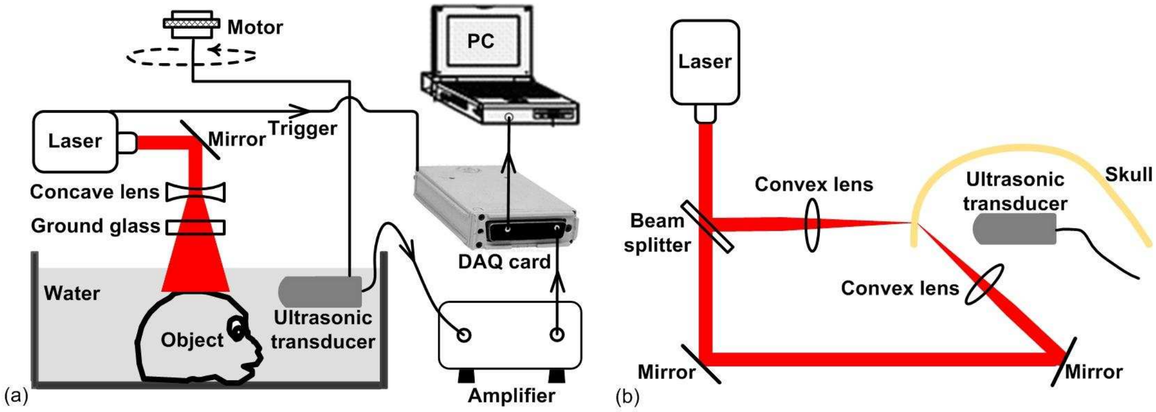

Figure 4.2: (a) Schematic of the transcranial PACT system. (b) Schematic of the PA system for validating the SOS map of the skull.

of the laser beam on the skull was controlled to 8 mJ/cm^2 (within the ANSI standard), which was further attenuated and homogenized by the skull before the laser beam reaching the object.

As shown in Fig. 4.2, a circular scanning geometry with a radius of 9 cm was employed to record the PA signals. A custom-built virtual point ultrasonic transducer was employed that had a central frequency of 2.25 MHz and a one-way bandwidth of 70% at -6 dB. Additional details regarding this transducer have been published elsewhere. [90] The position of the transducer was varied on the circular scan trajectory by use of a computer-controlled step motor. The angular step size was 0.9 degrees, resulting in measurement at 400 locations on the scanning circle.

The PA signals received by the transducer were amplified by a 50-dB amplifier (5072 PR, Panametrics, Waltham, MA), then directed to a data-acquisition (DAQ) card (Compuscope 14200; Gage Applied, Lockport, IL). The DAQ card was triggered by the Q-switch signal from the laser to acquire the photoacoustic signals simultaneously. The DAQ card features a high-speed 14-bit analog-to-digital converter with a sampling rate of 50 MS/s. The raw data transferred by the DAQ card was then stored in the PC for imaging reconstruction.

4.4 Image reconstruction results

4.4.1 Images of needle phantom

The reconstructed images corresponding to the head phantom containing the needles are displayed in Fig. 4.3. Figure 4.3(a) displays the control image of the needles, without the skull present, reconstructed by use of the back-projection algorithm. Figures 4.3(b) and (c) display reconstructed images of the phantom when the skull was present, corresponding to use of back-projection and time-reversal reconstruction algorithms, respectively. All images have been normalized to their maximum pixel value, and are displayed in the same grey-scale window. Due to the skull-induced attenuation of the high-frequency components of the PA signals, which was not compensated for in the reconstruction process, the spatial resolution of the control image in Fig. 4.3(a) appears higher than the images in Figs. 4.3(b) and (c). However, the image reconstructed by use of the time-reversal algorithm in Fig. 4.3(c) contains lower artifact levels and has an appearance closer to the control image than the image reconstructed by use of the back-projection algorithm in Fig. 4.3(b). This is expected, since the time-reversal algorithm compensates for variations in the SOS and density of the skull while the back-projection algorithm does not.

These observations are corrorborated by examination of profiles through the three images shown in Fig. 4.3(d), which correspond to the rows indicated by the superimposed dashed lines on the images. The solid black, dotted blue, and dashed red lines correspond to the reconstructed control image, and images reconstructed by use of the back-projection and time-reversal algorithms, respectively. The average full-width-at-half-maximum of the two needles in the images reconstructed by use of the time-reversal algorithm is reduced by 8% compared to the corresponding value computed from the images obtained via the back-projection algorithm.

4.4.2 Images of monkey brain phantom

The reconstructed images corresponding to the head phantom containing the brain are displayed in Fig. 4.4. Figure 4.4(a) displays photographs of the cortex and outer surface of

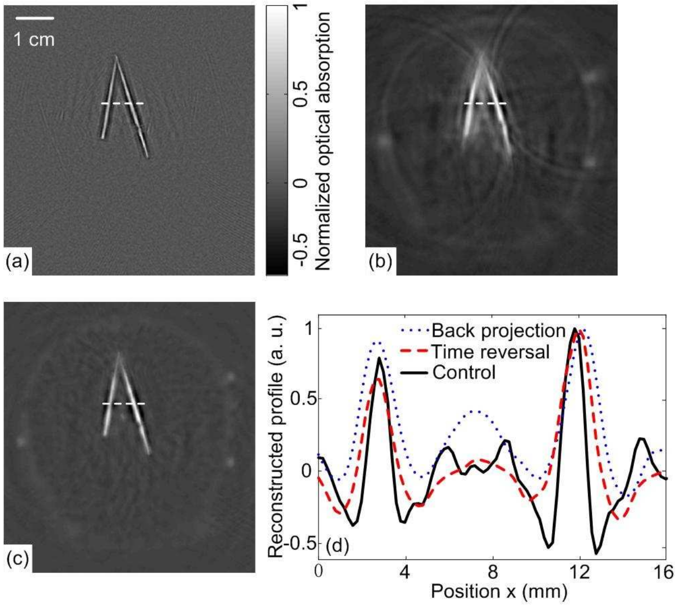

Figure 4.3: (a) The pin-phantom image reconstructed by use of the back- projection algorithm with no skull present. (b & c) The skull-present images reconstructed by use of the back-projection and time-reversal algorithms. (d) Profiles along the white dashed line in each of the three images are shown.

the skull. Figure 4.4(b) displays the control image (skull absent) reconstructed by use of the back-projection algorithm. The images of the complete phantom (skull present) reconstructed by use of the back-projection and time-reversal algorithms are shown in Figs. 4.4(c) and (d), respectively. All images have been normalized to their maximum pixel value, and are displayed in the same grey-scale window. As observed above for the needle phantom, the brain image reconstructed by use of the time-reversal algorithm in Fig. 4.4(d) contains lower artifact levels and has an appearance closer to the control image than the image reconstructed by use of the back-projection algorithm in Fig. 4.4(c).

This observation was quantified by computing error maps that represented the pixel-wise squared difference between the control and reconstructed images with the skull present. Figures 4.5(a) and (b) display the error maps between the control image and the images reconstructed by use of the back-projection and time-reversal algorithms, respectively. The error maps were computed within the region interior to the skull, which is depicted by the red contours superimposed on Figs. 4.4(b)-(d). Additionally, the root mean-squared difference (RMSD) was computed by computing the average values of the difference images. The

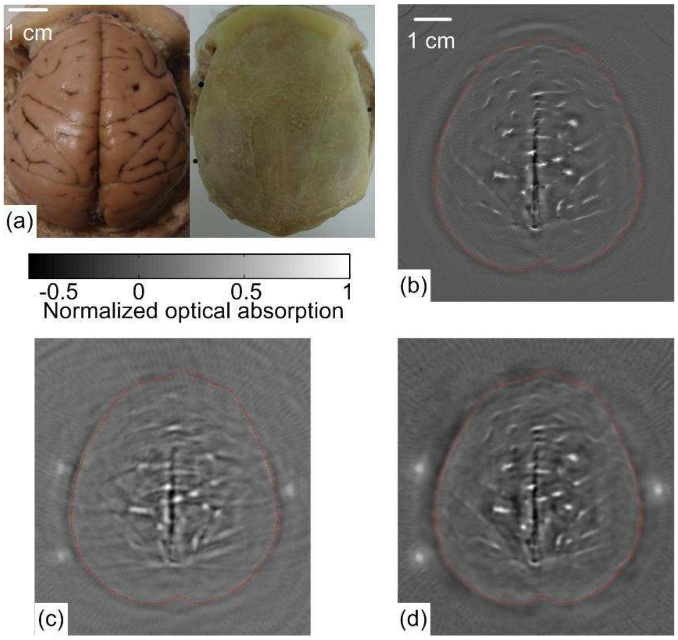

Figure 4.4: (a) A photograph of the brain specimen and skull. (b) The image reconstructed by use of the back-projection algorithm with no skull present. (c & d) The skull-present images reconstructed by use of the back-projection and time-reversal algorithms.

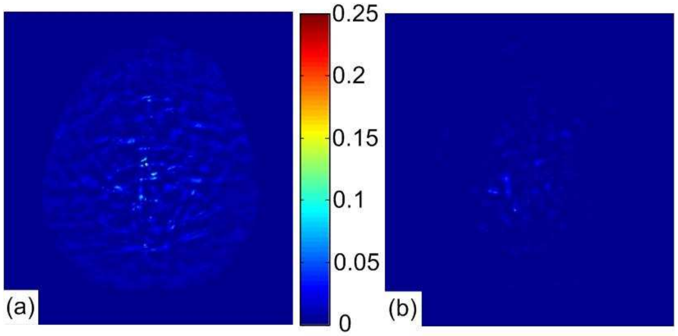

Figure 4.5: Difference images for the brain specimen for reconstructions using back-projection and time-reversal are shown in panel (a) and (b). In both cases, the reference image is the back-projection PACT reconstruction of the brain specimen with skull removed(see Fig. 4.4(b)).

RMSD corresponding to the back-projection and time-reversal results were 0.085 and 0.038. These results confirm that the image reconstructed by use of the time-reversal method, which compensated for the acoustic properties of the skull, was closer to the control image than the image produced by use of the back-projection algorithm.

4.5 Summary and discussion

In this chapter, we investigated a reconstruction methodology for transcranial PACT that employs detailed subject-specific descriptions of the acoustic properties of the skull to mitigate skull-induced distortions in the reconstructed image. Adjunct X-ray CT image data were employed to infer the spatially variant SOS and density distributions of the skull. Knowledge of these quantities was employed in a time-reversal image reconstruction algorithm to mitigate skull-induced aberrations of the measured PA signals. Our preliminary experimental results show that employed a primate skull demonstrated that the reconstruction methodology can produce images with improved fidelity and reduced artifact levels as compared to a previously employed back-projection algorithm. This is an important step towards the application of PACT for brain imaging in human subjects.

The use of X-ray CT image data for estimating the skull's SOS and density distributions was motivated by previous studies of transcranial ultrasound focusing [9]. Assuming that the skull size and shape does not change, only a single CT scan is required to estimate the SOS and density maps, and does not need to be repeated for subsequent PACT imaging studies of that patient. Because of this, it may be possible to safely monitor brain injuries or conduct other longitudinal studies without repeated exposure to ionizing radiation. Moreover, it may be possible to use adjunct image data produced by alternative modalities such as magnetic resonance imaging [49] or ultrasound tomography [175] to estimate the required SOS and density maps.

There remain several important topics for future study that may further improve image quality in transcranial PACT. In this preliminary study, to accommodate the 2D PACT imaging system and 2D image reconstruction algorithm, the phantoms were moved to the image plane, approximately 2 cm below the top of the skull. Note that this is not the plane in which the cortical vessels are normally found; the primate brain was moved to align the cortical vessels with the imaging plane. For in-vivo transcranial PACT applications in which the cortical structure is of interest, the geometry of the skull necessitates a full 3D treatment of the image reconstruction problem. The development of a robust image reconstruction algorithm for this task will be described in the next chapter. Additionally, accurate measurement of the transducer's electrical impulse response (EIR) and subsequent deconvolution of its effect on the measured data [149] would improve image reconstruction accuracy. Alternatives to the time-reversal image reconstruction algorithm employed in this study can also yield improvements in image quality, which will be described in the next chapter [51, 133].

In terms of the imaging physics, it is expected that development and utilization of image reconstruction algorithms that can compensate for the effects of acoustic attenuation and shear wave mode-conversion will further improve image resolution, particularly for thicker skulls. To date, the manner in which shear waves propagating in the skull affect PACT has only been investigated quantitatively for stratified planar media and planar detection surfaces [122] via computer-simulation studies. In that case, the effects were observed only in certain high-spatial resolution components of the imaged object. The effects of shear wave propagation and attenuation are both strongly dependent on the thickness of the skull. In this work, the average thickness of the skull was 3 mm and the distortions to the PA signal due to absorption and propagating shear waves were expected [122] to be of second-order effect as compared to the distortions due to the variations in the SOS and density. For adult human skulls, where the skull can be $\sim$7 mm thick, the relative importance of these effects in transcranial PACT remains to be investigated.

Chapter 5

Full-Wave Iterative Image Reconstruction in PACT

5.1 Introduction

Several image reconstruction methods have been proposed to compensate for weak variations in a medium's speed-of-sound (SOS) distribution [63, 85, 168]. These methods are based on geometrical acoustic approximations to the PA wave equation, which stipulate that the PA wavefields propagate along well-defined rays. For these ray-based propagation models to be valid, variations in the SOS distribution must occur on length scales that are large compared to the effective acoustic wavelength. These assumptions can be violated in preclinical and clinical applications of PACT. To compensate for strong SOS variations, a statistical approach has been proposed [28] to mitigate the artifacts in the reconstructed images caused by the wavefront distortions by use of *a priori* information regarding the acoustic heterogeneities. However, this method neglected variations in the medium's mass density and the effects of acoustic attenuation.

A few works have reported the development of full-wave PACT reconstruction algorithms that are based on solutions to the exact PA wave equation [50, 113, 133, 144, 173, 176]. While these methods are grounded in accurate models of the imaging physics and therefore have a broader domain of applicability than ray-based methods, they also possess certain practical limitations. Finite element methods (FEMs) have been applied for inverting the PA wave equation in both the time and temporal frequency domains [173, 176]. However, a very large computational burden accompanies these methods, which is especially problematic for three-dimensional (3D) applications of PACT. Image reconstruction methods based on time-reversal (TR) are mathematically exact in their continuous forms in homogeneous media for the 3D case [50]. While these methods possess significantly lower computational burdens then FEM-based approaches, they possess other limitations for use with practical PACT applications. For example, TR methods are predicated upon the assumption that the measured PA signals are densely sampled on a measurement surface that encloses the object, which is seldom achievable in biomedical applications of PACT. More recently, a Neumann series-based reconstruction method has been reported [113, 133] for media containing SOS variations that is based on a discretization of a mathematically exact inversion formula. The robustness of the method to practical sparse sampling of PA signals, however, has not been established.

In this chapter, we develop and investigate a full-wave approach to iterative image reconstruction in PACT with media possessing inhomogeneous SOS and mass density distributions as well as acoustic attenuation described by a frequency power law. The primary contributions of the work are the establishment of a discrete imaging model that is based on the exact PA wave equation and a procedure to implement an associated matched discrete forward and backprojection operator pair. The availability of efficient numerical procedures to implement these operators permits a variety of modern iterative reconstruction methods to be employed that can effectively mitigate image artifacts due to data incompleteness, noise, finite sampling , and modeling errors. Specifically, the k-space pseudospectral method is adopted [144] for implementing the forward operator and a numerical procedure for implementing the exact adjoint of this operator is provided. The k-space pseudospectral method possesses significant computational advantages over real space finite-difference and finite-element methods, as it allows fewer mesh points per wavelength and allows larger time steps without reducing accuracy or introducing instability [24]. An iterative image reconstruction algorithm that seeks to minimize a total variation (TV)-regularized penalized least squares (PLS) cost function is implemented by use of the developed projection operators and investigated in computer-simulation and experimental studies of PACT in inhomogeneous acoustic media. Also, the performance of this algorithm is compared to that of an existing TR method.

This chapter is organized as follows. In Section 5.2, an explicit formulation of the discrete imaging model is described. Section 5.3 gives a description of the numerical and experimental studies, which includes the implementation of the forward and backprojection operators, and the iterative reconstruction algorithm. The numerical and experimental results are given in Section 5.4. This chapter concludes with a summary and discussion in Section 5.5.

5.2 Explicit formulation of discrete imaging model

The k-space pseudospectral method for numerically solving the photoacoustic wave equation described in Section 2.2 will be employed to implement the action of the system matrix $\mathbf{H}$. In this section, we provide an explicit matrix representation of $\mathbf{H}$ that will subsequently be employed to determine $\mathbf{H}^{\dagger}$.

Equations (2.18) - (2.20) can be described by a single matrix equation to determine the updated wavefield variables after a time step Δt as

$$\mathbf{v}_{m+1} = \mathbf{W}\mathbf{v}_m, \tag{5.1}$$

where $\mathbf{v}_m = (\mathbf{u}_m^1, \mathbf{u}_m^2, \mathbf{u}_m^3, \boldsymbol{\rho}_m^1, \boldsymbol{\rho}_m^2, \boldsymbol{\rho}_m^3, \mathbf{p}_m)^{\mathrm{T}}$ is a $7N \times 1$ vector containing all the wavefield variables at the time step $m\Delta t$. The $7N \times 7N$ propagator matrix $\mathbf{W}$ is defined as

$$\mathbf{W} \equiv \begin{bmatrix} \mathbf{I}_{N\times N} & \mathbf{0}_{N\times N} & \mathbf{0}_{N\times N} & \mathbf{0}_{N\times N} & \mathbf{0}_{N\times N} & \mathbf{0}_{N\times N} & \boldsymbol{\Phi}_1 \\ \mathbf{0}_{N\times N} & \mathbf{I}_{N\times N} & \mathbf{0}_{N\times N} & \mathbf{0}_{N\times N} & \mathbf{0}_{N\times N} & \mathbf{0}_{N\times N} & \boldsymbol{\Phi}_2 \\ \mathbf{0}_{N\times N} & \mathbf{0}_{N\times N} & \mathbf{I}_{N\times N} & \mathbf{0}_{N\times N} & \mathbf{0}_{N\times N} & \mathbf{0}_{N\times N} & \boldsymbol{\Phi}_3 \\ \boldsymbol{\Psi}_1 & \mathbf{0}_{N\times N} & \mathbf{0}_{N\times N} & \mathbf{I}_{N\times N} & \mathbf{0}_{N\times N} & \mathbf{0}_{N\times N} & \boldsymbol{\Psi}_1\boldsymbol{\Phi}_1 \\ \mathbf{0}_{N\times N} & \boldsymbol{\Psi}_2 & \mathbf{0}_{N\times N} & \mathbf{0}_{N\times N} & \mathbf{I}_{N\times N} & \mathbf{0}_{N\times N} & \boldsymbol{\Psi}_2\boldsymbol{\Phi}_2 \\ \mathbf{0}_{N\times N} & \mathbf{0}_{N\times N} & \boldsymbol{\Psi}_3 & \mathbf{0}_{N\times N} & \mathbf{0}_{N\times N} & \mathbf{I}_{N\times N} & \boldsymbol{\Psi}_3\boldsymbol{\Phi}_3 \\ \mathbf{D}_1 & \mathbf{D}_2 & \mathbf{D}_3 & \mathbf{E} & \mathbf{E} & \mathbf{E} & \mathbf{G} \end{bmatrix}, \tag{5.2}$$

where $\mathbf{D}_i \equiv \mathbf{C}(\mathbf{B}_u + \boldsymbol{\Psi}_i + \mathbf{B}_\rho\boldsymbol{\Psi}_i)$ $(i = 1, 2, 3)$, $\mathbf{E} \equiv \mathbf{C} + \mathbf{C}\mathbf{B}_\rho$, $\mathbf{G} \equiv \mathbf{C}\sum_{i=1}^{3} \mathbf{B}_u\boldsymbol{\Phi}_i + (\mathbf{I} + \mathbf{B}_\rho)\boldsymbol{\Psi}_i\boldsymbol{\Phi}_i$, $\mathbf{I}_{N\times N}$ is the $N \times N$ identity matrix, and $\mathbf{0}_{N\times N}$ is the $N \times N$ zero matrix. Recall that $\boldsymbol{\Phi}_i$ and $\boldsymbol{\Psi}_i$ were defined below Eqn. (2.17).

The wavefield quantities can be propagated forward in time from $t = 0$ to $t = (M-1)\Delta t$ as

$$\begin{bmatrix} \mathbf{v}_0 \\ \mathbf{v}_1 \\ \vdots \\ \mathbf{v}_{M-1} \end{bmatrix} = \mathbf{T}_{M-1} \cdots \mathbf{T}_1 \begin{bmatrix} \mathbf{v}_0 \\ \mathbf{0}_{7N\times 1} \\ \vdots \\ \mathbf{0}_{7N\times 1} \end{bmatrix}, \tag{5.3}$$

where the $7NM \times 7NM$ matrices $\mathbf{T}_m$ $(m = 1, \cdots, M-1)$ are defined in terms of $\mathbf{W}$ as

$$\mathbf{T}_m = \begin{bmatrix} \begin{matrix} \mathbf{I}_{7N\times 7N} & \cdots & \mathbf{0}_{7N\times 7N} \\ \vdots & \ddots & \vdots \\ \mathbf{0}_{7N\times 7N} & \cdots & \mathbf{I}_{7N\times 7N} \\ \mathbf{0}_{7N\times 7N} & \cdots & \mathbf{W} \end{matrix} & \mathbf{0}_{(m+1)\cdot 7N\times (M-m)\cdot 7N} \\ \mathbf{0}_{(M-m-1)\cdot 7N\times m\cdot 7N} & \mathbf{0}_{(M-m-1)\cdot 7N\times (M-m)\cdot 7N} \end{bmatrix}, \tag{5.4}$$

with $\mathbf{W}$ residing between the $(7N(m-1)+1)$-th to $7Nm$-th rows and the $(7Nm+1)$-th to $7N(m+1)$-th columns of $\mathbf{T}_m$.

From the equation of state in Eqn. (2.7) and initial conditions Eqn. (2.5), the vector $(\mathbf{v}_0, \mathbf{0}, \cdots, \mathbf{0})^{\mathrm{T}}$ can be computed from the initial pressure distribution $\mathbf{p}_0$ as

$$\begin{bmatrix} \mathbf{v}_0 \\ \mathbf{0}_{7N\times 1} \\ \vdots \\ \mathbf{0}_{7N\times 1} \end{bmatrix} = \mathbf{T}_0 \mathbf{p}_0, \tag{5.5}$$

where

$$\mathbf{T}_0 \equiv (\boldsymbol{\tau}, \mathbf{0}_{7N\times N}, \cdots, \mathbf{0}_{7N\times N})^{\mathrm{T}}, \tag{5.6}$$

$$\boldsymbol{\tau} \equiv (\mathbf{0}_{N\times N}, \mathbf{0}_{N\times N}, \mathbf{0}_{N\times N}, \frac{1}{3}\mathbf{C}^{-1}, \frac{1}{3}\mathbf{C}^{-1}, \frac{1}{3}\mathbf{C}^{-1}, \mathbf{I}_{N\times N})^{\mathrm{T}}, \tag{5.7}$$

and $\mathbf{p}_0$ is the initial pressure distribution defined as

$$\mathbf{p}_0 \equiv \mathbf{\Gamma}\mathbf{A}, \tag{5.8}$$

where

$$\mathbf{\Gamma} \equiv \mathrm{diag}(\Gamma(\mathbf{r}_1), \cdots, \Gamma(\mathbf{r}_N)), \tag{5.9}$$

and

$$\mathbf{A} \equiv (A(\mathbf{r}_1), \cdots, A(\mathbf{r}_N))^{\mathrm{T}}, \tag{5.10}$$

represent the discrete representations of the Grueneisen parameter $\Gamma(\mathbf{r})$ and the sought-after absorbed optical energy density distribution $A(\mathbf{r})$ within the object, respectively.

In general, the transducer locations $\mathbf{r}_l^d$ at which the PA data $\hat{\mathbf{p}}$ are recorded will not coincide with the vertices of the Cartesian grid at which the values of the propagated field quantities are computed. The measured PA data $\hat{\mathbf{p}}$ can be related to the computed field quantities via an interpolation operation as

$$\hat{\mathbf{p}} = \mathbf{S} \begin{bmatrix} \mathbf{v}_0 \\ \mathbf{v}_1 \\ \vdots \\ \mathbf{v}_{M-1} \end{bmatrix}, \tag{5.11}$$

where

$$\mathbf{S} \equiv \begin{bmatrix} \mathbf{\Theta} & \mathbf{0}_{L\times 7N} & \cdots & \mathbf{0}_{L\times 7N} \\ \mathbf{0}_{L\times 7N} & \mathbf{\Theta} & \cdots & \mathbf{0}_{L\times 7N} \\ \vdots & \vdots & \ddots & \vdots \\ \mathbf{0}_{L\times 7N} & \mathbf{0}_{L\times 7N} & \cdots & \mathbf{\Theta} \end{bmatrix}. \tag{5.12}$$

Here, $\mathbf{\Theta} \equiv [\mathbf{s}_1, \cdots, \mathbf{s}_L]^{\mathrm{T}}$, where $\mathbf{s}_l$ $(l = 1, \cdots, L)$ is a $1 \times 7N$ row vector in which all elements are zeros except the 4 corresponding to acoustic pressure at 4 grid nodes $\mathbf{r}_{l,1}, \mathbf{r}_{l,2}, \mathbf{r}_{l,3}, \mathbf{r}_{l,4}$ that are nearest to the transducer location $\mathbf{r}_l^d$. In other words, these 4 entries are interpolation coefficients to compute the acoustic pressure at the l-th transducer, and their values are given by the barycentric coordinates of $\mathbf{r}_l^d$ with respect to $\mathbf{r}_{l,1}, \mathbf{r}_{l,2}, \mathbf{r}_{l,3}, \mathbf{r}_{l,4}$, which are determined by Delaunay triangulation [76].

By use of Eqns. (5.3), (5.5), (5.8), and (5.11), one obtains

$$\hat{\mathbf{p}} = \mathbf{H}\mathbf{A} \tag{5.13}$$

where the sought-after explicit form of the system matrix is identified as

$$\mathbf{H} \equiv \mathbf{S}\mathbf{T}_{M-1} \cdots \mathbf{T}_1 \mathbf{T}_0 \mathbf{\Gamma}. \tag{5.14}$$

Here, for simplicity, we neglect the acousto-electrical impulse response (EIR) of the ultrasonic transducers and assume each transducer is point-like. However, a description of how to incorporate the transducer responses in the developed imaging model is provided in Appendix B.

Commonly employed iterative image reconstruction methods involve use of a backprojection matrix $\mathbf{H}^\dagger$ that corresponds to the adjoint of the system matrix. Since $\mathbf{H}$ contains real-valued elements in our case, $\mathbf{H}^\dagger$ is equivalent to the transpose $\mathbf{H}^{\mathrm{T}}$. According to Eqn. (**??**), the explicit form of $\mathbf{H}^{\mathrm{T}}$ is given by

$$\mathbf{H}^{\mathrm{T}} = \mathbf{\Gamma}^{\mathrm{T}} \mathbf{T}_0^{\mathrm{T}} \mathbf{T}_1^{\mathrm{T}} \cdots \mathbf{T}_{M-1}^{\mathrm{T}} \mathbf{S}^{\mathrm{T}}. \tag{5.15}$$

The implementations of $\mathbf{H}$ and $\mathbf{H}^{\mathrm{T}}$ are described in Section 5.3.1. Note that, although the descriptions of $\mathbf{H}$ and $\mathbf{H}^{\mathrm{T}}$ above are based on the 3D PA wave equation, the two-dimensional formulation is contained as a special case.

5.3 Descriptions of numerical and experimental studies

Numerical studies were conducted to demonstrate the effectiveness and robustness of the proposed discrete imaging model in studies of iterative image reconstruction from incomplete data sets in 2D and 3D PACT. Specifically, the system matrix and its adjoint, as formulated in Section 5.2, were employed with an iterative image reconstruction algorithm that was designed to minimize a PLS cost function that contained a total variation (TV) penalty term. The performance of the reconstruction algorithm was compared to an existing TR-based reconstruction algorithm.

5.3.1 Implementation of the forward and backprojection operators

The k-space pseudospectral method for numerically solving the photoacoustic wave equation has been implemented in the MATLAB k-Wave toolbox [143]. This toolbox was employed to compute the action of $\mathbf{H}$. To prevent acoustic waves from leaving one side of the grid and re-entering on the opposite side, an anisotropic absorbing boundary condition called a perfectly matched layer (PML) was employed to enclose the computational grids. The performance of the PML was dependent on both the size and attenuation of the layer. A PML thickness of 10 grid points, together with a PML absorption coefficient of 2 nepers per meter, were found to be sufficient to reduce boundary reflection and transmission for normally incident waves [67, 140] and were employed in this study. To accurately and stably model wave propagation, the temporal and spatial steps were related by the Courant-Friedrichs-Lewy (CFL) number as [82, 143]

$$\Delta t \leq \frac{\mathrm{CFL}\Delta r_{\min}}{c_{\max}}, \tag{5.16}$$

where the $\Delta r_{\min}$ is the minimum grid spacing, and a CFL number of 0.3 typically provides a good compromise between computation accuracy and speed [140, 143]. A more detailed description of the implementation of the k-space pseudospectral method can be found in Refs. [140, 143].

The action of the backprojection matrix on the measured pressure data $\hat{\mathbf{p}}$ was implemented according to Eqn. (5.15). It can be verified that $\mathbf{p}^{\mathrm{bp}} = \mathbf{H}^{\mathrm{T}}\hat{\mathbf{p}}$ can be computed as

$$\mathbf{v}^{M-1} = \boldsymbol{\Theta}^{\mathrm{T}}\hat{\mathbf{p}}_{M-1}, \tag{5.17}$$

$$\mathbf{v}^{m-1} = \boldsymbol{\Theta}^{\mathrm{T}}\hat{\mathbf{p}}_{m-1} + \mathbf{W}^{\mathrm{T}}\mathbf{v}^{m}, \quad m = M-1, \cdots, 1 \tag{5.18}$$

$$\mathbf{p}^{\mathrm{bp}} = \boldsymbol{\Gamma}\boldsymbol{\tau}^{\mathrm{T}}\mathbf{v}^{0}. \tag{5.19}$$

Since $\boldsymbol{\Theta}$ and $\boldsymbol{\tau}$ are both sparse matrices that can be stored and transposed, $\boldsymbol{\Theta}^{\mathrm{T}}\hat{\mathbf{p}}_m$ and $\boldsymbol{\tau}^{\mathrm{T}}\mathbf{v}^1$ can be readily computed. Most of block matrices in the propagator matrix $\mathbf{W}$ are zero or identity matrices. Therefore, to compute $\mathbf{W}^{\mathrm{T}}\mathbf{v}^m$, we only need to compute the actions of transposed non-trivial block matrices in $\mathbf{W}$. To incorporate the PML boundary condition, both $\mathbf{W}$ and $\mathbf{W}^{\mathrm{T}}$ should be modified as described in Ref. [140].

5.3.2 Reconstruction algorithms

By use of the proposed discrete imaging model and methods for implementing $\mathbf{H}$ and $\mathbf{H}^{\mathrm{T}}$, a wide variety of iterative image reconstruction algorithms can be employed for determining estimates of $\mathbf{A}$. In this work, we utilized an algorithm that sought solutions of the optimization problem

$$\hat{\mathbf{A}} = \arg\min_{\mathbf{A}\geq 0} \|\hat{\mathbf{p}} - \mathbf{H}\mathbf{A}\|^2 + \lambda|\mathbf{A}|_{\mathrm{TV}}, \tag{5.20}$$

where λ is the regularization parameter, and a non-negativity constraint was employed. For the 3D case, the TV-norm is defined as

$$|\mathbf{A}|_{\mathrm{TV}} = \sum_{n=1}^{N} \left\{([\mathbf{A}]_n - [\mathbf{A}]_{n_1^-})^2 + ([\mathbf{A}]_n - [\mathbf{A}]_{n_2^-})^2 + ([\mathbf{A}]_n - [\mathbf{A}]_{n_3^-})^2\right\}^{\frac{1}{2}}, \tag{5.21}$$

where $[\mathbf{A}]_n$ denotes the n-th grid node, and $[\mathbf{A}]_{n_1^-}$, $[\mathbf{A}]_{n_2^-}$, $[\mathbf{A}]_{n_3^-}$ are neighboring nodes before the n-th node along the first, second and third dimension, respectively. The fast iterative shrinkage/thresholding algorithm (FISTA) [11, 150] was employed to solve Eqn. (5.20), and its implementation is given in Appendix C. The regularization parameter λ was empirically selected to have a value of 0.001 and was fixed for all studies.

A TR image reconstruction algorithm based on the k-space pseudospectral [144] method was also utilized in the studies described below. The TR reconstruction algorithm solves the discretized acoustic Eqns. (2.18) - (2.20) backward in time subject to initial and boundary conditions as described in reference [144]. The parameters of the PML boundary condition were the same with the ones employed in our system matrix construction.

For both algorithms, images were reconstructed on a uniform grid of 512×512 pixels with a pitch of 0.2 mm for the 2D simulation studies and on a $256 \times 256 \times 128$ grid with a pitch of 0.4 mm for the 3D studies. All simulations were computed in the MATLAB environment on a workstation that contained dual hexa-core Intel(R) Xeon(R) E5645 CPUs and a NVIDIA Tesla C2075 GPU. The GPU was equiped with 448 1.15 GHz CUDA Cores and 5 GB global memory. The Jacket toolbox [178] was employed to perform the computation of Eqns. (2.18) - (2.20) and (40) - (42) on the GPU.

5.3.3 Computer-simulation studies of 2D PACT

Scanning geometries: Three different 2D scanning geometries were considered to investigate the robustness of the reconstruction methods to different types and degrees of data incompleteness. A 'full-view' scanning geometry utilized 180 transducers that were evenly distributed on a circle of radius 40 mm. A 'few-view' scanning geometry utilized 60 transducers that were equally distributed on the circle. Finally, a 'limited-view' scanning geometry utilized 90 transducers that were evenly located on a semi-circle of radius 40 mm.

Numerical phantoms: The two numerical phantoms shown in Fig. 5.1-(a) and (b) were chosen to represent the absorbed optical energy density distribution **A** in the 2D computer-simulation studies. The blood vessel phantom shown in Fig. 5.1(a) was employed to investigate the robustness of the reconstruction methods with respect to different types and degrees of data incompleteness mentioned above. The low contrast disc phantom displayed in Fig. 5.1-(b) was employed to investigate the robustness of the reconstruction methods with respect to errors in the SOS and density maps introduced below.

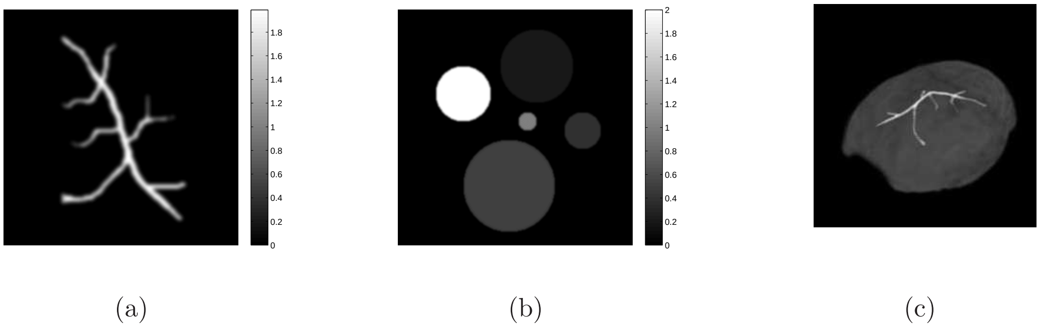

(a) (b) (c)

Figure 5.1: The (a) blood vessel and (b) disc numerical phantoms employed to represent **A** in the 2D computer-simulation studies. Panel (c) is the overlapped image with 3D vessel phantom and skull, which is only used to show the relative position of the phantom to the skull.

Measurement data: Assuming ideal point-like transducer and neglecting the transducer EIR and acoustic attenuation, simulated pressure data corresponding to the numerical phantoms were computed at the transducer locations by use of the k-space pseudospectral method for the 3 measurement geometries. To avoid committing an 'inverse crime' [66], a 1024×1024 grid with a pitch of 0.1 mm was employed in this computation. A total of 20,000 temporal samples were computed at each transducer location with time step $\Delta t = 30$ ns, all of which were employed by the TR image reconstruction method. However, only the first 1,500 temporal samples were employed by the iterative reconstruction method. The same procedure was repeated for noisy pressure data, where 3% (with respect to maximum value of noiseless data) additive white Gaussian noise (AWGN) was added to the simulated pressure data.

Investigation of systematic errors: The SOS and density maps employed in the simulation studies were representative of a monkey skull [52]. The dimensions of the skull were approximately 7 cm × 6 cm, and its thickness ranges from 2 to 4 mm. Figure 5.2(a) and (b) show a transverse slice of the SOS and density maps, which were used in the 2D simulations.

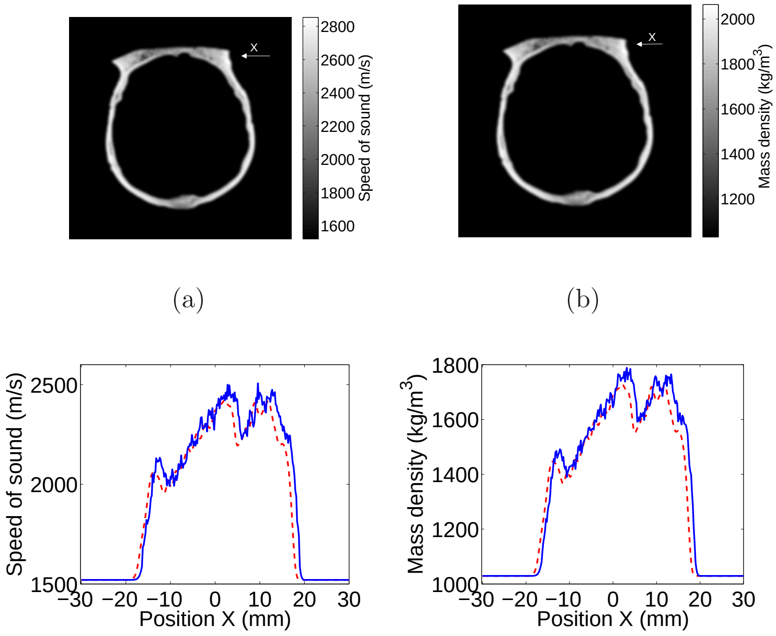

(a) (b)

(c) (d)

Figure 5.2: A slice of the SOS (a) and density (b) map deduced from the X-ray CT data of a monkey skull. Panel (c) and (d) display profiles of the SOS and density maps along the 'X'-axis indicated in Fig. 5.2, respectively. Red dashed lines are the profiles of the assumed maps, whereas the blue solid lines are the profiles of maps with errors.

Since errors in the estimated SOS and density maps are inevitable regardless in how they are determined, we investigated the robustness of the reconstruction methods with respect to the SOS and density map errors, which were generated in two steps. First, 1.3% (with respect to maximum value) uncorrelated Gaussian noise with mean value of 1.7% of the maximum value was added to the SOS and density maps to simulate inaccuracy of the SOS and density values. Subsequently, the maps were shifted by 7 pixels (1.4 mm) to simulate a registration error. Figure 5.2-(c) and (d) show profiles of the SOS and density maps with those errors along the 'X'-axis indicated by the arrows in Fig. 5.2(a) and (b), respectively.

5.3.4 Computer-simulation studies of 3D PACT

Because PACT is inherently a 3D method, we also conducted 3D simulation studies to evaluate and compare the iterative reconstruction method and the TR method. As in the 2D studies described above, the 3D SOS and density maps were representative of a monkey skull. A 3D blood vessel phantom was positioned underneath the skull to mimic the blood vessels on the cortex surface. To demonstrate this configuration, Figure 5.1(c) shows the overlapped images of the 3D phantom and the skull. The assumed scanning geometry was a hemispherical cap with radius of 46 mm, and 484 transducers were evenly distributed on the hemispherical cap by use of the golden section spiral method. The pressure data were computed on a $512 \times 512 \times 256$ grid with a pitch of 0.2 mm and a time step $\Delta t = 30$ ns. The simulated pressure data were then contaminated with 3% AWGN. The TR reconstruction method employed 2,000 temporal samples at each transducer location, whereas the iterative method employed 1,000 samples.

5.3.5 Studies utilizing experimental data

Since the acoustic absorption and dispersion were modeled by the system matrix, the iterative method can naturally compensate for absorption and dispersion effects during reconstruction. To demonstrate the compensation for those effects, images were reconstructed by use of the iterative method with experimental data obtained from a well-characterized phantom object that is displayed in Fig. 3.2. The phantom contained 6 optically absorbing structures (pencil leads with diameter 1 mm) embedded in agar. These structures were surrounded by an acrylic cylinder, which represents the acoustic heterogeneities and absorption in the experiments. The cylinder had inner and outer radii of 7.1 and 7.6 cm, respectively, and a height of 3 cm. The density and SOS of the acrylic were measured and found to be 1200 kg m^{-3} and 3100 m s^{-1}, and the estimated acoustic absorption parameters were found to be $\alpha_0 = 1.3$ dB MHz^{-y} cm^{-1} and $y = 0.9$ [53]. These values were assigned to the the annular region occupied by the acrylic in the 2D SOS maps $c_0(\mathbf{r})$, density map $\rho_0(\mathbf{r})$ and attenuation coefficient $\alpha_0(\mathbf{r})$, respectively. The SOS value 1480 m s^{-1} and density value 1000 kg m^{-3} of water were assigned elsewhere. Since we neglected the relatively weak acoustic attenuation due to the water bath and agar, $\alpha_0(\mathbf{r})$ was also set to zero elsewhere.

The experimental data were acquired from a cylindrically focused ultrasound transducer that had a central frequency of 2.25 MHz with a bandwidth of 70% [90]. The transducer was scanned along a circular trajectory of radius 95 mm, and 20,000 temporal samples were measured at each transducer location at a sampling rate of 20 MHz. More details about the data acquisition can be found in Ref. [53]. In this study, images were reconstructed by use of PA signals recorded at 200, 100 (over 180 degrees), and 50 transducer locations, which correspond to the full-view, limited-view, and few-view scanning geometry, respectively. The TR reconstruction method employed 20,000 temporal samples at each transducer location, while the iterative method employed 2,000 samples. The reference images were also reconstructed by use of the data obtained at 200 transducer locations when the acrylic cylinder was absent. Since the pencil lead phantom is expected to generate quasi-cylindrical waves and the morphology of the acoustic heterogeneity (the acrylic shell) was a cylinder, the cylindrical wave propagation can be approximated by the 2D PA wave equation. Accordingly, we employed a 2D imaging model in the experimental study, and all the reconstructions were performed on a grid of 512×512 pixels with a pitch of 0.5 mm. The effects of shear wave propagation in the acrylic cylinder were neglected, which we expected to be of second-order importance compared to wavefield perturbations that arise from inhomogeneties in the SOS and density distributions [122].

5.4 Simulation and experimental results

5.4.1 Computer-simulations corresponding to different scanning geometries

The reconstructed images corresponding to the three scanning geometries are displayed in Figs. 5.3 - 5.6. In each figure, the results in the top row correspond to use of the TR reconstruction method, while the bottom row shows the corresponding results obtained by use of the iterative method. The profiles shown in each figure are along the 'Y'-axis indicated by the arrow in Fig. 5.3(a). The red solid lines and blue dashed lines correspond to profiles through the phantom and reconstructed images, respectively. With the full-view scanning geometry, the TR method and the iterative method both produce accurate reconstructed images. However, with the few-view and the limited-view scanning geometries, the images reconstructed from the iterative method contain fewer artifacts and less noise than the TR results Also, the values of the images reconstructed from the iterative method are much closer to the values of the phantom than those produced by the TR method. The root mean square error (RMSE) between the phantom and the reconstructed images were also computed. The RMSE of images reconstructed by use of the TR method and the iterative method corresponding to noisy pressure data with the full-view, few-view, and limited-view scanning geometries are 0.011, 0.042, 0.081 and 0.003, 0.007, 0.008, respectively. The computational time of the TR method was 1.7 minutes, while the iterative method took approximately 10 minutes to finish 20 iterations.

5.4.2 Simulation results with errors in SOS and density maps

Figure 5.7 shows the images reconstructed from noisy pressure data corresponding to the low contrast disc phantom in the case where SOS and density maps have no error. The results corresponding to TR and iterative image reconstruction algorithms are shown in the top and bottom row, respectively. The RMSE corresponding to the time-reversal and the iterative results are 0.026 and 0.007, respectively. These results suggest that the iterative algorithm can more effectively reduce the noise level in the reconstructed images than the time-reversal algorithm.

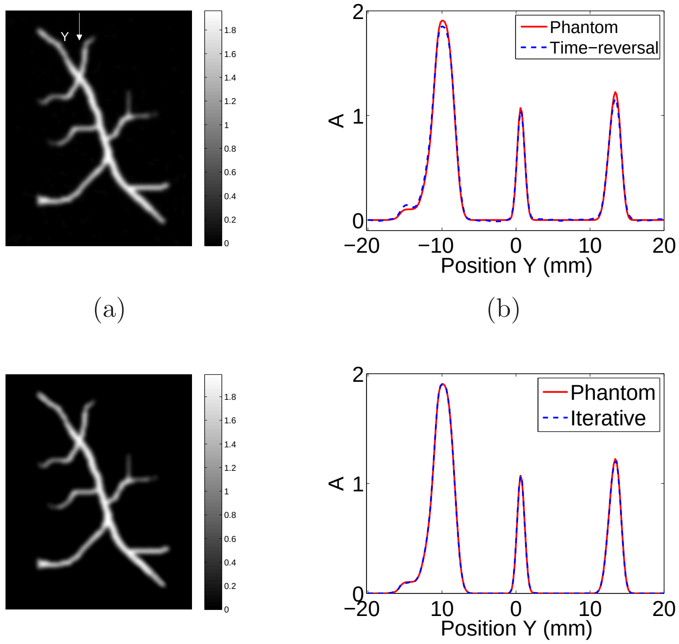

(a) (b)

(c) (d)

Figure 5.3: (a) and (c) are reconstructed images from noiseless data with full-view scanning geometry by use of the TR method and iterative method, respectively. (b) and (d) are the corresponding profiles along the 'Y'-axis indicated in panel (a).

The images reconstructed by use of the SOS and density maps with errors are shown in Fig. 5.8. The image produced by the iterative method has cleaner background than the TR result, and the RMSE corresponding to the TR and the iterative results are 0.086 and 0.034, respectively. The boundaries of the disc phantoms also appear sharper in the image reconstructed by the iterative method as compared to the TR result. This can be attributed to the TV regularization employed in the iterative method. These results suggest that appropriately regularized iterative reconstruction methods can be more robust to the errors in the SOS and density maps than the TR method.

5.4.3 3D simulation results

The 3D blood vessel phantom and the reconstructed images were visualized by the maximum intensity projection (MIP) method. Figure 5.9(a) shows the phantom image, and Fig. 5.9(b) and (c) display the images reconstructed by use of the TR method and the iterative method,

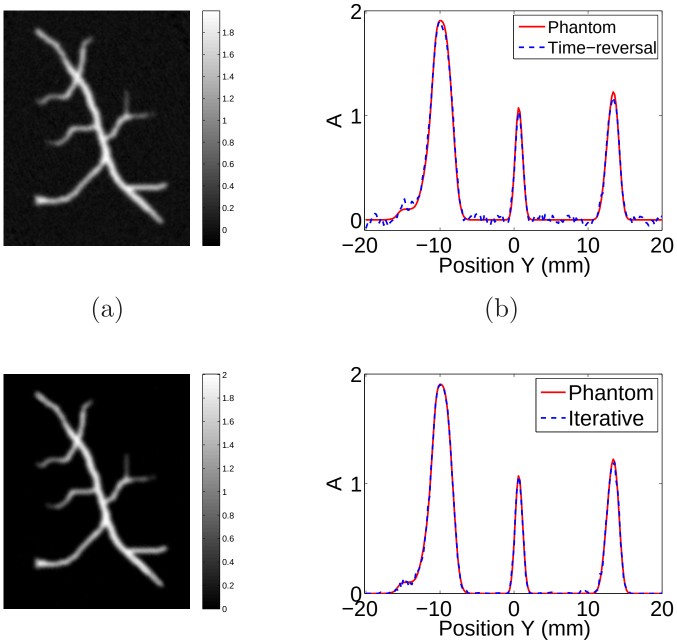

(a) (b)

(c) (d)

Figure 5.4: (a) and (c) are reconstructed images from the noisy pressure data with 3% AWGN corresponding to the full-view scanning geometry by use of the TR method and iterative method, respectively. (b) and (d) are the corresponding profiles.

respectively. They are all displayed in the same grey scale window. The RMSE corresponding to the TR and the iterative results are 0.018 and 0.003, respectively. These results suggest that the iterative method is robust to the data incompleteness and the noise in the pressure data. The computational time of the TR method was approximately 6 minutes, while the iterative method with 10 iterations required 110 minutes.

5.4.4 Experimental results

The images reconstructed from the experimental data are shown in Figs. 5.10 - 5.13. Figure 5.10 shows the image reconstructed with the full-view scanning geometry by use of the TR method (top row) and the iterative method (bottom row). Figure 5.10(a) and (c) display the reference images produced by each of the methods when the acrylic shell was absent. Figure 5.10(b) and (e) show the reconstructed images for the case when the acrylic shell was present. The RMSE between Fig. 5.10(b), (d) and the reference images 5.10(a), (c) are

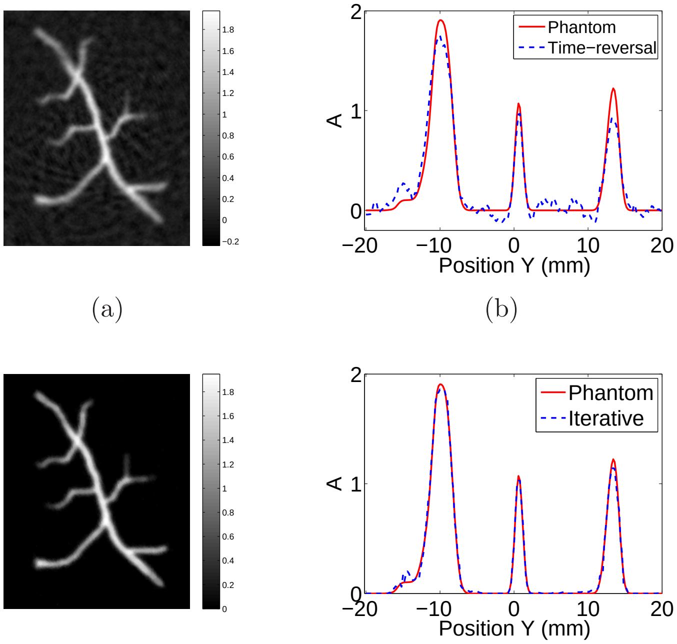

(a) (b)

(c) (d)

Figure 5.5: (a) and (c) are reconstructed images from the noisy pressure data with 3% AWGN corresponding to the few-view scanning geometry by use of the TR method and iterative method, respectively. (b) and (d) are the corresponding profiles.

0.003 and 0.002, respectively. Figure 5.11(a) and (c) show the images reconstructed with the few-view scanning geometry when the acrylic shell was present. The corresponding image profiles are displayed in Figure 5.11(b) and (d). The profiles of Fig. 5.11(a) and (c) along the 'Y'-axis were shown in Fig. 5.12, which shows that the iterative method produced higher resolution images than the TR method. This can be attritubed to the TV regularization that mitigates model errors that arise, for example, by neglecting the shear wave and finite transducer aperture effects. The RMSE between Fig. 5.11(b), (d) and their reference images are 0.005 and 0.002, respectively. Figure 5.13 displays the images reconstructed with the limited-view scanning geometry when the acrylic shell was present. The RMSE between Fig. 5.13(a), (c) and their reference images are 0.007 and 0.003, respectively. These results show that the iterative algorithm can effectively compensate for the acoustic attenuation and mitigate artifacts and distortions due to incomplete measurement data.

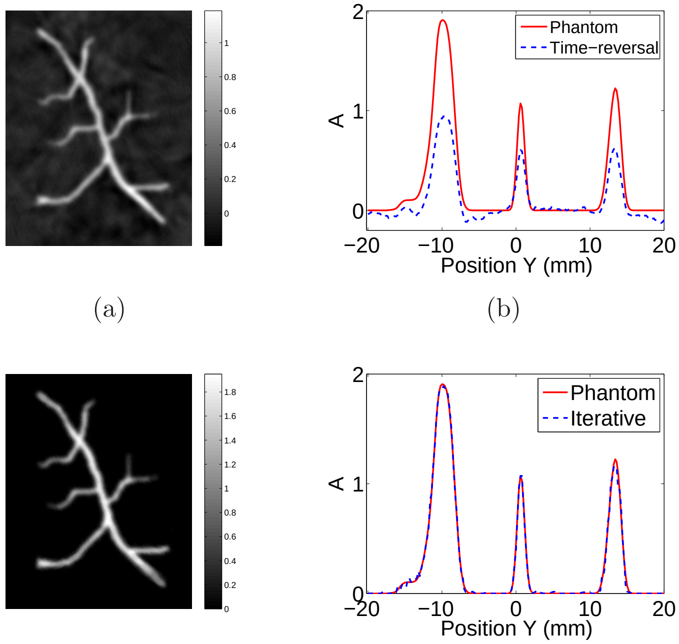

(a) (b) (c) (d)

Figure 5.6: (a) and (c) are reconstructed images from the noisy pressure data with 3% AWGN corresponding to the limited-view scanning geometry by use of the TR method and iterative method, respectively. (b) and (d) are the corresponding profiles.

5.5 Conclusion and discussion

In this chapter, we proposed and investigated a full-wave approach to iterative image reconstruction in PACT with acoustically inhomogeneous lossy media. An explicit formulation of the discrete imaging model based on the k-space pseudospectral method was described and the details of implementing the forward and backprojection operators were provided. The matched operator pair was employed in an iterative image reconstruction algorithm that sought to minimize a TV-regularized PLS cost function. The developed reconstruction methodology was investigated by use of both computer-simulated and experimental PACT measurement data, and the results demonstrated that the reconstruction methodology can effectively mitigate image artifacts due to data incompleteness, noise, finite sampling, and modeling errors. This suggests that the proposed image reconstruction method has the potential to be adopted in preclinical and clinical PACT applications.

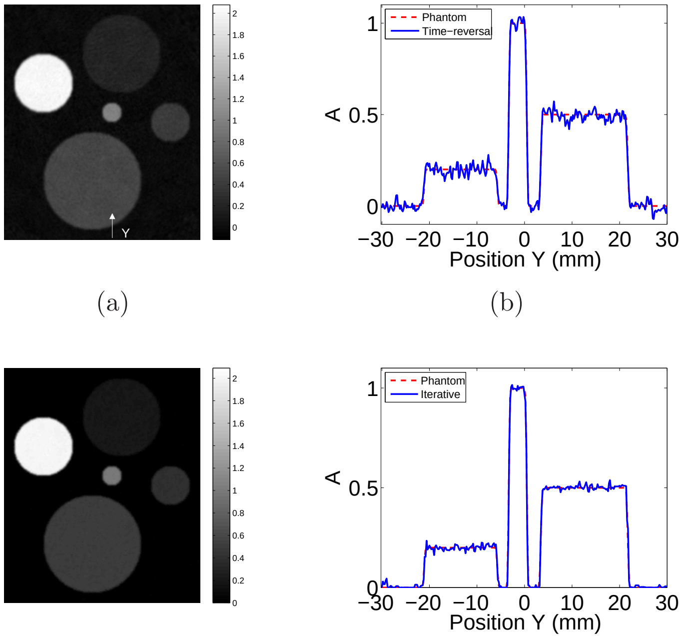

(a) (b)

(c) (d)

Figure 5.7: (a) and (c) are reconstructed images with actual SOS and density maps by use of the TR method and iterative method, respectively. (b) and (d) are the corresponding profiles along the 'Y'-axis indicated in panel (a).

There remain several important topics to further investigate and validate the proposed iterative reconstruction method. It has been shown [50, 113] that the performance of reconstruction methods can be degraded when the SOS distribution satisfies a trapping condition [50,113]. Therefore, future studies may include the investigation of numerical properties of the proposed image reconstruction method for cases in which the SOS distribution satisfies the trapping condition. Also, because the signal detectability is affected by the noise properties of an image reconstruction method, investigation of statistical properties of the iterative image reconstruction method is another important topic for future studies. Moreover, the proposed image reconstruction method can be further validated through additional experimental studies, and the quality of the produced images will be assessed by use of objective and quantitative measures.

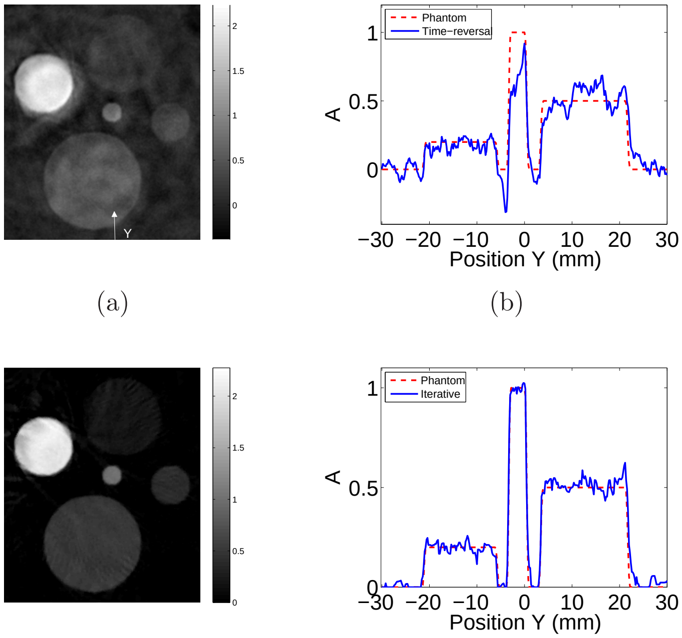

(a) (b)

(c) (d)

Figure 5.8: (a) and (c) are reconstructed images with SOS and density maps with errors by use of the TR method and iterative method, respectively. (b) and (d) are the corresponding profiles along the ‘Y’-axis indicated in panel (a).

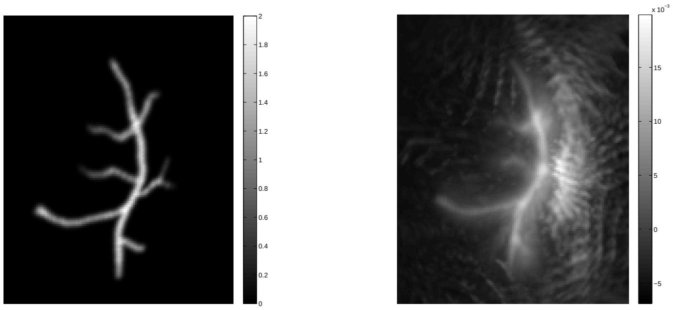

(a) (b) (c)

Figure 5.9: Maximum intensity projection renderings of the 3D phantom (a), and the reconstructed 3D images by use of the TR method (b) and the iterative method (c).

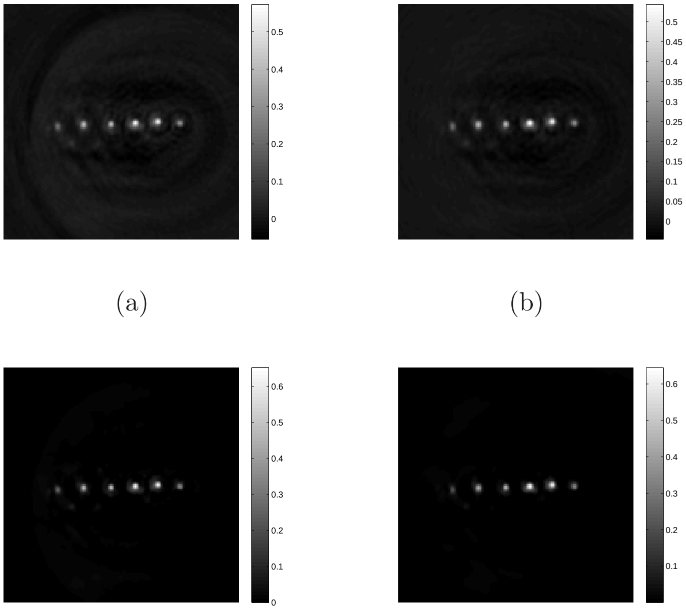

(a) (b)

(c) (d)

Figure 5.10: (a) and (b) are reconstructed images by use of the TR method from 200 views with acrylic shell absent and present, respectively. (c) and (d) are reconstructed images by use of the iterative method from 200 views with acrylic shell absent and present, respectively.

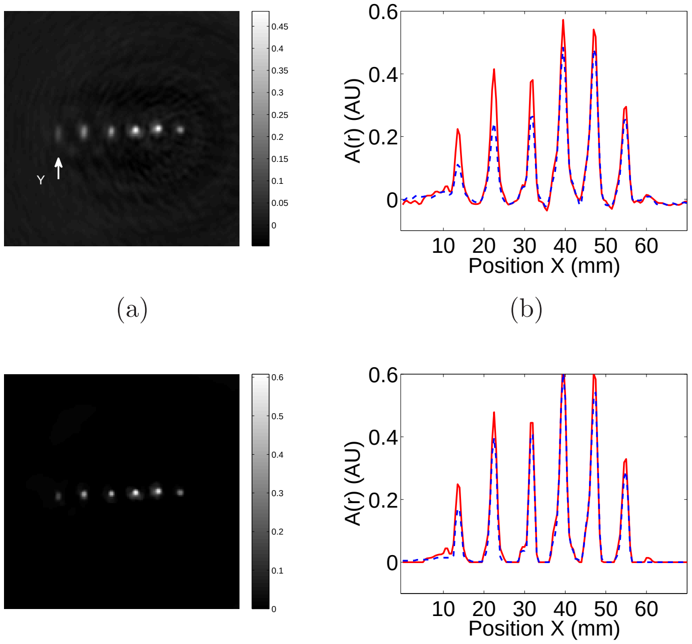

(a) (b)

(c) (d)

Figure 5.11: (a) and (c) are reconstructed images with data from 50 view angles over 360 degrees (acrylic shell present) by use of the TR method and iterative method, respectively. (b) and (d) are their corresponding profiles (dashed blue lines), where red solid lines are the profiles of the reference images in Fig. 5.10 (a) and (c).

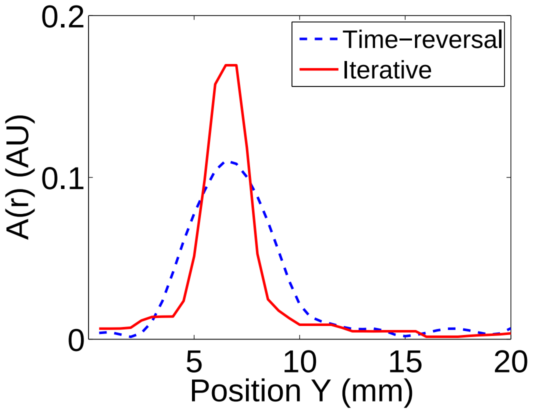

Figure 5.12: The profiles of the reconstructed images in Fig. 5.11 along the ‘Y’-axis indicated in Fig. 5.11(a).

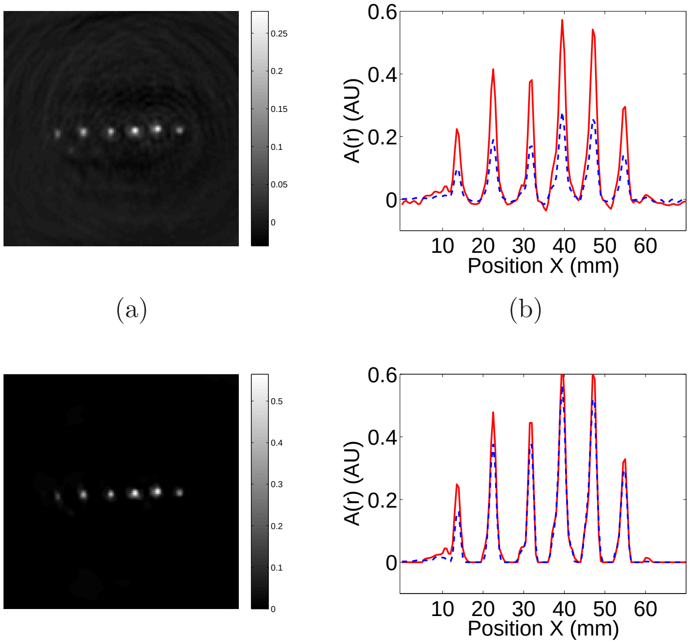

(a) (b)

(c) (d)

Figure 5.13: (a) and (c) are reconstructed images with data from 100 view angles over 180 degrees (acrylic shell present) by use of the TR method and iterative method, respectively. (b) and (d) are their corresponding profiles (dashed blue lines), where red solid lines are the profiles of the reference images in Fig. 5.10 (a) and (c).

Chapter 6

Joint Reconstruction of $A(\mathbf{r})$ and $c(\mathbf{r})$ in PACT

6.1 Introduction

Because variations in the SOS distribution induce the PA wavefield aberrations, certain information regarding an object's SOS distribution is encoded in the PACT measurement data. Based on this observation, it is natural to question whether $A(\mathbf{r})$ and $c(\mathbf{r})$ can both be accurately determined *from the PACT measurement data alone* [18, 58, 177, 179]. This will be referred to as the joint reconstruction (JR) problem and is the topic of this chapter.

Theoretical and computational studies of the JR problem have been conducted, but all are limited currently in scope. Theoretical work on the JR problem that neglects discrete sampling effects has established that $A(\mathbf{r})$ and $c(\mathbf{r})$ can be uniquely determined from the measured data for certain special cases [48, 50]. However, the uniqueness of the JR problem for more general cases has not been established. Another study established that the linearized JR problem, in which a geometrical acoustics propagation model was employed, is generally unstable [135] and suggested that the same conclusion would hold for the general case where wavefield propagation modeling was based on the full wave equation.

Other works have addressed the development of computational methods for solving the JR problem by use of discretely sampled measurement data [58, 177, 179]. In [179], an iterative reconstruction method was proposed to jointly estimate both $A(\mathbf{r})$ and $c(\mathbf{r})$. That study employed a geometrical acoustics propagation model and assumed *a priori* information regarding the singular support of $c(\mathbf{r})$. In [58, 177], a JR method based on the Helmholtz equation was proposed, which was solved by the finite element method (FEM). While this method is grounded in a accurate model of the imaging physics, it suffers from an intensive computational burden. A similar JR approach was proposed [18] that employed a time-reversal (TR) adjoint method. All of these works were preliminary in nature in the sense that they did not systematically explore the numerical properties of the JR problem. This fact coupled with the scarcity of theoretical works suggests that there remains an important need to elucidate the practical feasibility of JR.

The primary objective of this chapter is to demonstrate and investigate practical limitations of JR that are caused by the ill-conditioned nature of the problem. An optimization-based approach to the JR of $A(\mathbf{r})$ and $c(\mathbf{r})$ is developed for this purpose. The developed reconstruction method is based on an alternating optimization scheme, where $A(\mathbf{r})$ is reconstructed by use of a previously-developed full-wave iterative method [51], while $c(\mathbf{r})$ is reconstructed by use of a nonlinear optimization algorithm based on the Fréchet derivative of an objective function with respect to $c(\mathbf{r})$ [15, 96]. Computer-simulation studies are conducted to reveal insights into how the relative spatial frquency contents of $A(\mathbf{r})$ and $c(\mathbf{r})$, along with their geometric configurations, influence the ability to accomplish accurate JR. We also investigate the effects of model errors, including neglecting acoustic attenuation and transducer impulse reponses, on the accuracy of JR.

This chapter is organized as follows. In Section 6.2, the imaging physics of PACT in heterogeneous media is reviewed briefly. The derivation of the Fréchet derivative of a pertinent objective function with respect to $c(\mathbf{r})$ is also provided. Section 6.3 contains the formulation of the alternating optimization approach to the JR of $A(\mathbf{r})$ and $c(\mathbf{r})$ in PACT. The numerical studies and results are given in Section 6.4. This chapter concludes with a summary and discussion in Section 6.5.

6.2 Background

6.2.1 Photoacoustic wavefield propagation in heterogeneous media

We consider PA wavefield propagation in lossless fluid media where the variation of mass density can be neglected. Let $p(\mathbf{r}, t)$ denote the photoacoustically-induced pressure wavefield at location $\mathbf{r} \in \mathbb{R}^3$ and time $t \geq 0$. The photoacoustic wavefield $p(\mathbf{r}, t)$ satisfies [155]:

$$\nabla^2 p(\mathbf{r}, t) - \frac{1}{c(\mathbf{r})^2} \frac{\partial^2 p(\mathbf{r}, t)}{\partial t^2} = 0, \tag{6.1}$$

subject to initial conditions

$$p(\mathbf{r}, 0) = \Gamma(\mathbf{r}) A(\mathbf{r}), \qquad \left. \frac{\partial p(\mathbf{r}, t)}{\partial t} \right|_{t=0} = 0, \tag{6.2}$$

where $\Gamma(\mathbf{r})$ is the Grueneisen parameter that is assumed to be known.

6.2.2 Fréchet derivative with respect to $c(\mathbf{r})$

Here, for simplicity, we neglect the acousto-electrical impulse response (EIR) and the spatial impulse response (SIR) of the ultrasonic transducers. However, we will investigate the impact of EIR and SIR on the JR results in Secion 6.4.5. The quantity $\tilde{p}(\mathbf{r}^m, t)$ represents the PA data recorded by the m-th transducer at location $\mathbf{r}^m$ ($m = 1, \cdots, M$). For the sake of notational clarity, we represent the measured PA data as continuous functions of t, but the continuous results that follow can be readily discretized as described in Section 6.3.

For a given $A(\mathbf{r})$, the inverse problem of reconstructing $c(\mathbf{r})$ can be formulated as an optimization problem in which the following objective functional is minimized with respect to $c(\mathbf{r})$:

$$\mathcal{E}[c(\mathbf{r})] = \sum_{m=1}^{M} \int_0^T \mathrm{d}t [p(\mathbf{r}^m, t) - \tilde{p}(\mathbf{r}^m, t)]^2, \tag{6.3}$$

subject to the constraint that $p(\mathbf{r}^m, t)$ satisfies (6.1), where T denotes the maximum time at which the PA data were recorded.

Gradient-based iterative algorithms can be utilized to minimize the nonlinear functional (6.3). Such methods require the functional gradient, or Fréchet derivative, of $\mathcal{E}$ with respect to $c(\mathbf{r})$, which can be calculated by use of the adjoint method [15,96]. In the adjoint method, the adjoint wave equation is defined as

$$\nabla^2 q(\mathbf{r}, t) - \frac{1}{c(\mathbf{r})^2} \frac{\partial^2 q(\mathbf{r}, t)}{\partial t^2} = -s(\mathbf{r}, t), \tag{6.4}$$

subject to terminal conditions

$$q(\mathbf{r}, T) = 0, \qquad \left.\frac{\partial q(\mathbf{r}, t)}{\partial t}\right|_{t=T} = 0. \tag{6.5}$$

The source term $s(\mathbf{r}, t)$ is defined as

$$s(\mathbf{r}, t) = \sum_{m=1}^{M} [p(\mathbf{r}^m, t) - \tilde{p}(\mathbf{r}^m, t)] \delta(\mathbf{r} - \mathbf{r}^m). \tag{6.6}$$

Upon solving (6.1) and (6.4), the Fréchet derivative of $\mathcal{E}$ with respect to $c(\mathbf{r})$ can be determined as [15, 96],

$$\nabla_c \mathcal{E} = -\frac{4}{c(\mathbf{r})^3} \int_0^T \mathrm{d}t \frac{\partial p(\mathbf{r}, t)}{\partial t} \frac{\partial q(\mathbf{r}, t)}{\partial t}. \tag{6.7}$$

Once the Fréchet derivative is obtained, it can be utilized by any gradient method as the search direction to iteratively reduce the functional value of (6.3). The numerical implementation of the Fréchet derivative is described below.

6.3 Optimization-based joint image reconstruction

Based on the discrete imaging model (5.13), the JR problem can be formulated as

$$\hat{\mathbf{A}}, \hat{\mathbf{c}} = \underset{\mathbf{A} \geq 0, \mathbf{c} > 0}{\arg\min} \|\mathbf{H}(\mathbf{c})\mathbf{A} - \tilde{\mathbf{p}}\|^2 + \lambda_1 \mathrm{R}(\mathbf{A}) + \lambda_2 \mathrm{R}(\mathbf{c}), \tag{6.8}$$

where R($\mathbf{A}$) and R($\mathbf{c}$) are penalty functions that impose regularity on the estimates of $\mathbf{A}$ and $\mathbf{c}$, respectively, and λ_1, λ_2 are the corresponding regularization parameters. To the authors' best knowledge, the convexity of the objective function in (6.8) is still unknown. Although the data fidelity term is convex with respect to $\mathbf{A}$, the convexity with respect to $\mathbf{c}$ is unknow. Even if it is convex with respect to $\mathbf{c}$, the biconvex data fidelity term is not convex in general [39]. A heuristic alternating optimization approach can be employed to find solutions that approximately satisify (6.8). This approach consists of two sub-problems: reconstruction of $\mathbf{A}$ given $\mathbf{c}$ and reconstruction of $\mathbf{c}$ given $\mathbf{A}$.

Reconstruction of $A(\mathbf{r})$ *given* $c(\mathbf{r})$: The inverse problem of reconstructing $\mathbf{A}$ for a given $\mathbf{c}$ can be formulated as the penalized least squares problem

$$\hat{\mathbf{A}} = \arg\min_{\mathbf{A}\geq 0} \|\mathbf{H}(\mathbf{c})\mathbf{A} - \tilde{\mathbf{p}}\|^2 + \lambda_A \mathrm{R}(\mathbf{A}), \tag{6.9}$$

where λ_A is the regularization parameter, which is different from λ_1 in (6.8) in general. Several reconstruction methods have been proposed for solving problems of this form [51,144].

Reconstruction of $c(\mathbf{r})$ *given* $A(\mathbf{r})$: For a given $\mathbf{A}$, an estimate of $\mathbf{c}$ can be formed as

$$\hat{\mathbf{c}} = \arg\min_{\mathbf{c}>0} \|\mathbf{H}(\mathbf{c})\mathbf{A} - \tilde{\mathbf{p}}\|^2 + \lambda_c \mathrm{R}(\mathbf{c}), \tag{6.10}$$

where λ_c is the regularization parameter, which is different from λ_2 in (6.8) in general. Equation (6.10) can be solved by use of gradient-based methods, which require computation of the gradient of the objective function in (6.10) with respect to $\mathbf{c}$. Details regarding this gradient computation are provided in the Appendix D.

Alternating optimization algorithm: Based on (6.9) and (6.10), JR of $\mathbf{A}$ and $\mathbf{c}$ can be accomplished by alternately solving (6.9) and (6.10), which is described in Algorithm 1. $\mathbf{A}^{(0)}$ and $\mathbf{c}^{(0)}$ are the initial guesses of $\mathbf{A}$ and $\mathbf{c}$, respectively, and ϵ_A and ϵ_c are convergence tolerances. The functions '$\mathrm{F_A}$' and '$\mathrm{F_c}$' compute the solutions of (6.9) and (6.10), respectively, and are described below in Section 6.4.1. The function 'Dist' measures the metric (e.g. Euclidean metric) between $\mathbf{A}^{(i)}$ and $\mathbf{A}^{(i+1)}$ (or between $\mathbf{c}^{(i)}$ and $\mathbf{c}^{(i+1)}$).

Algorithm 1 Alternating optimization approach to JR of $\mathbf{A}$ and $\mathbf{c}$

```
Input: $\tilde{\mathbf{p}}$, $\mathbf{A}^{(0)}$, $\mathbf{c}^{(0)}$, $\epsilon_A$, $\epsilon_c$, $\lambda_A$, $\lambda_c$
Output: $\hat{\mathbf{A}}$, $\hat{\mathbf{c}}$
$i = 0$
while $\epsilon_1 < \epsilon_A$ and $\epsilon_2 < \epsilon_c$ do
    $\mathbf{c}^{(i+1)} \leftarrow \mathrm{F_c}\big(\mathbf{c}^{(\mathrm{i})}, \mathbf{A}^{(\mathrm{i})}, \tilde{\mathbf{p}}, \lambda_\mathrm{c}\big)$
    $\mathbf{A}^{(i+1)} \leftarrow \mathrm{F_A}\big(\mathbf{A}^{(\mathrm{i})}, \mathbf{c}^{(\mathrm{i+1})}, \tilde{\mathbf{p}}, \lambda_\mathrm{A}\big)$
    $\epsilon_1 \leftarrow \mathrm{Dist}(\mathbf{A}^{(\mathrm{i})}, \mathbf{A}^{(\mathrm{i+1})})$
    $\epsilon_2 \leftarrow \mathrm{Dist}(\mathbf{c}^{(\mathrm{i})}, \mathbf{c}^{(\mathrm{i+1})})$
    $i \leftarrow i + 1$
end while
$\hat{\mathbf{A}} \leftarrow \mathbf{A}^{(i)}$
$\hat{\mathbf{c}} \leftarrow \mathbf{c}^{(i)}$
```

6.4 Numerical studies and results

Computer simulations were conducted to investigate the numerical properties of the JR problem. Although the optimization approach to JR described above is based on the 3D wave equation, the 2D formulation is contained as a special case and is investigated in this section.

6.4.1 Descriptions of numerical studies

The implementation of the alternating optimization method shown in Algorithm 1 is described below. The function '$\mathrm{F_c}$' that computes the solution of (6.10) was implemented based on the MATLAB k-Wave toolbox [143]. Specifically, the wave equation (6.1) and the adjoint wave equation (6.4) were solved numerically by use of the k-space pseudospectral method. The computed PA wavefield and the adjoint wavefield were employed to compute the gradient of the objective function in (6.10) (see Appendix D). The gradient was subsequently utilized by the limited-memory BFGS (L-BFGS) algorithm to solve (6.10) [31,65,91]. The implementation of the function '$\mathrm{F_A}$' that solves (6.9) can be found in [51]. In this study, a total variation (TV) penalty was adopted. The 'Dist' function measured the difference in terms of root mean square error (RMSE), and the convergence tolerances ϵ_A and ϵ_c were empirically chosen to have a value of 10^{-2} throughout the studies. In all studies, the initial guesses of $\mathbf{A}$ and $\mathbf{c}$ were set to be $\mathbf{A}^{(0)} = 0$ and $\mathbf{c}^{(0)} = 1480$ m/s, which is the background SOS.

Both $\mathbf{A}$ and $\mathbf{c}$ were reconstructed on a uniform grid of 256×256 pixels with a pitch of 0.5 mm. A total of 800 transducers were evenly distributed on the sides of a square with side length 100 mm. The PA data were computed at transducer locations on a 512×512 grid with a pitch 0.25 mm. At each transducer location, 6000 temporal samples were recorded with time step $\Delta t = 50$ ns.

All simulations were computed in the MATLAB environment on a workstation that contained dual hexa-core Intel(R) Xeon(R) E5645 CPUs and a NVIDIA Tesla C2075 GPU. The GPU was equiped with 448 1.15 GHz CUDA Cores and 5 GB global memory. The Jacket toolbox [178] was employed to accelerate the computation of (6.1) and (6.4) on the GPU.

6.4.2 Conditions for accurate reconstruction of c given A (sub-problem (6.10))

In this study, we propose two heuristic conditions that, when satisified, suggest that $\mathbf{c}$ can be accurately estimated from PACT measurement data given known $\mathbf{A}$. One condition is with respect to to the support of $\mathbf{A}$, which will be referred as the support condition and described in Appendix-B. Another condition is related to the spatial frequency contents of $\mathbf{A}$, which will be referred as the k-space condition and discussed in Section **??**. The $\mathbf{A}$ satisfying the support condition will be called 'adequate' in this paper, otherwise it will be called 'defective'; the $\mathbf{A}$ satisfying both heuristic conditions will be called 'sufficient', otherwise it will be called 'deficient'. When $\mathbf{A}$ is sufficient, we will show that it is possible to achieve accurate JR in Section 6.4.4.

Note that the support condition is based on two assumptions and is only verified by computer simulations instead of rigorous mathematical proofs, so the condition is more an observation than a necessary/sufficient condition in mathematical sense; i.e. when the support condition is satisfied, it is more likely to achieve accurate reconstrution of **c** or accurate JR. Therefore, we call the support condion a heuristic condition. This also applies to the heuristic k-space condition described below.

Support condition: Numerical phantoms representing 'adequate' **A** (left column of Fig. 6.2) and 'defective' **A** (left column of Fig. 6.3) were chosen to verify the support condition given above. Figure 6.2(a) shows the 'adequate' **A** that corresponds to the case where supp(c) is enclosed by supp(A), and Fig. 6.2(c) corresponds the case where supp(c) $\subseteq$ supp(A). 'Defective' **A** in the left column of Fig. 6.3 correspond to different degrees of defectiveness of supp(A). In order to exclude the effect of the spatial frequency contents of **A**, both 'adequate' and 'defective' **A** employed here have sharp boundaries so that the k-space condition discussed below is satisfied. Figure 6.1 shows the numerical phantom that represents the SOS distribution, **c**, in a breast.

The reconstructed estimates of **c** corresponding to 'adequate' and 'defective' **A** are shown in the middle columns of Fig. 6.2 and 6.3, respectively. The profiles shown in both figures are along the 'X'-axis indicated by the arrow in Fig. 6.2(b). The images were reconstructed from noiseless data without regularization. The results in Fig. 6.2 corroborate that it is possible to accurately reconstruct **c** given an 'adequate' **A**, as suggested by the support condition given above. The results in Fig. 6.3 show that the reconstructed **c** could be either accurate (first and second rows) or inaccurate (third and fourth rows), which suggest that the support condition may not be a necessary condition for accurate image reconstruction.

K-space condition: The condition on supp(A) is not the only factor affecting the reconstruction of **c**. In this section, we use a series of computer simulations to show that the spatial frequency contents of **A** will also affect the accuracy of the reconstructed **c**.

Figure 6.4 shows the numerical phantoms that are employed to represent **A** and **c**. To exclude the effects of supp(A), the phantom of **A** was chosen such that supp(c) $\subseteq$ supp(A), i.e. the support condition was satisfied. The phantom depicting **A** was then convolved with different Gaussian kernels to generate additional phantoms that possessed different relative spatial bandwidth, which is defined as the full width at half maximum of the blurring kernel in k-space.

The reconstructed estimates of **c** obtained when **A** was given and possessed different degrees of relative spatial bandwidth are shown in Fig. 6.5. The images from the top to the bottom row correspond to the bandwidth ratio of **A** to **c** being 0.25, 0.44, and 1.0, respectively. Both noiseless and noisy data were employed to reconstruct **c**. The RMSE of the reconstructed **c** with respect to the bandwidth ratio of **A** to **c** for both noiseless and noisy cases were plotted in Fig. 6.6. These results show that the spatial frequency contents of **A** will affect the accuracy of reconstruction of **c**. To be specific, in order to accurately reconstruct **c**, these results suggest that spatial bandwidth of **A** should be larger than the spatial bandwidth of **c**, which is referred as the k-space condition.

6.4.3 Relative numerical instability of the sub-problems in (6.9) and (6.10)

Below, we investigate the relative numerical stability of the problems of reconstructing **A** given **c** (sub-problem (6.9)) and the problem of reconstructing **c** given **A** (sub-problem (6.10)). The phantoms of **A** and **c** used here are the same as the ones in Fig. 6.4. To investigate the numerical instability, **A** (resp. **c**) was perturbed by additive white Gaussian noise (AWGN) when reconstructing **c** (resp. **A**). The perturbation is measured by the relative error, which is defined as the ratio of the l_2 norm of the AWGN to the l_2 norm of **A** (or **c**). Figure 6.7 shows the reconstructed **A** (first and second columns) and **c** (third and fourth columns) corresponding to the perturbed **c** and **A**, respectively. The results from the top to the bottom row correspond to relative error of 0.2%, 1.0% and 5.0%, respectively. These results are summarized in Fig. 6.8, which shows that, for a fixed relative error, the reconstructed estimate of **c** has larger RMSE than does the reconstructed estimate of **A**. This demonstrates that the problem of of reconstructing **c** given **A** is more ill-conditioned than the problem of reconstructing **A** given **c**.

Figure 6.9 gives another example showing the numerical instability of reconstruction of **c**. Figure 6.9(a) and (c) are two similar numerical phantoms depicting **A**. The RMSE between these phantoms is 0.004. Figures 6.9(b) and (d) display the reconstructed estimates of **c** when the **A** specified in Fig. 6.9(a) and (c) was assumed, respectively. These results demonstrate that the problem of reconstructing **c** for a given **A** is ill-posed in the sense that small changes in **A** can produce large changes in the reconstructed estimate of **c**. This observation is consistent with the theoretical results in Ref. [135].

In fact, the (**A**, **c**) pair in the top row of Fig. 6.9 produces nearly identical PA data at all transducer locations considered (RMSE $= 3.2 \times 10^{-4}$) as the (**A**, **c**) pair in the bottom row, as shown in Fig. 6.10. These results suggest the solutions of the JR problem in PACT might not be unique. Consequently, it indicates that accurate JR of **A** and **c**, in general, may not be possible.

6.4.4 Joint reconstruction in idealized scenarios

The numerical instability of sub-problem (6.10) implies the general JR problem is also unstable, which can be seen from the JR results in first row of Fig. 6.11. These results correspond to the unsmoothed phantoms of **A** and **c** in Fig. 6.4, which satisfy both the support condition and the k-space condition. By use of those phantoms, noiseless PA data were generated for JR, which was conducted without regularization. To exclude the effects of representation error on the JR results, the data generation and JR were performed on the same grid with pixel size 0.5 mm. However, even in this idealized case where **A** was sufficient and inverse crime was committed, neither **A** nor **c** was accurately reconstructed. These results indicate the numerical instability of the JR problem.

In order to accurately reconstruct both **A** nor **c**, it is necessary to incorporate regularization into the reconstruction. The regularized JR results were generated without inverse crime and are displayed in the 2-4 row of Fig. 6.11, where the corresponding regularization parameters λ_A and λ_c are both 10^{-5}, 10^{-4}, 10^{-3}, respectively. Those results show that the numerical instability of the JR problem can be mitigated by incorporating appropriate regularization into the reconstruction.

Joint reconstruction was also performed with noisy data, where the simulated PA data were contaminated by 3% AWGN. The first and second rows of Fig. 6.12 show the noisy results obtained with regularization parameters $\lambda_A = 10^{-3}$ and $\lambda_c = 10^{-2}$. There results show that, by incorporating appropriate regularization, the proposed JR method is robust to the measurement noise. To compare with the JR results, **A** was also reconstructed by use of a full-wave iterative reconstruction method developed in a previous paper [51], and the results are displayed in the third row of Fig 6.12. The iterative method assumed a constant SOS of 1600 m/s in the medium, which was selected such that the RMSE of the reconstructed image was minimized compared to other choices for the SOS. The RMSE of the reconstructed $\mathbf{A}$ by use of the JR method and the iterative method are 0.01 and 0.21, respectively. These results also show that the jointly reconstructed $\mathbf{A}$ is more accurate than the one reconstructed with a constant SOS.

6.4.5 Joint reconstruction in practice

The above JR results show that, in an idealized scenario where $\mathbf{A}$ is sufficient and model errors can be neglected, it is possible to achieve accurate JR of $\mathbf{A}$ and $\mathbf{c}$ when appropriate regularization is employed. However, in practice, $\mathbf{A}$ may not be sufficient, and there always exist model errors. In this section, we will investigate the feasibility of accurate JR in practice. First, we consider the impact of different model errors on JR results, including neglecting acoustic attenuation, point-like transducer assumption and imperfect EIR deconvolution. We then show the impact of deficient $\mathbf{A}$ on the JR results. Finally, we will show the combining effects of model errors and deficient $\mathbf{A}$ on the JR results. In this section, all the JRs were conducted with noisy data, where 3% AWGN were added to the simulated PA data.

Effects of acoustic attenuation: In many applications, acoustic attenuation is not negligible [29,118,144]. To investigate the effects of model error of neglecting acoustic attenuation, the simulated PA data were generated in a lossy medium, where the the acoustic attenuation coefficient α can be described by a frequency power law of the form $\alpha(\mathbf{r}, f) = \alpha_0(\mathbf{r}) f^y$ [138]. The frequency-independent attenuation coefficient $\alpha_0 = 10$ dB MHz and the power law exponent $y = 2.0$ were employed in the data generation, which correspond to the values of α_0 and y in human kidneys that have the strongest acoustic attenuation among typical biological tissues [139]. To exclude the effects of defective $\mathbf{A}$, we employed the same phantoms of $\mathbf{A}$ and $\mathbf{c}$ as in Section 6.4.4 to generate simulated data. Those phantoms will also be employed below when we investigate the effects of other model errors on the JR results. Figure 6.13 shows the attenuated data from one transducer compared to the unattenuated data. By use of the attenuated data, JR was conducted with regularization parameters $\lambda_A = 10^{-3}$ and $\lambda_c = 10^{-2}$ but without compensation for the acoustic attenuation, and the results are displayed in Fig. 6.14. Those results show that the amplitude of the reconstructed $\mathbf{A}$ was reduced due to the model error of neglecting acoustic attenuation, which had little impact on the reconstruction of $\mathbf{c}$. This can be explained by the fact that acoustic attenuation has larger impact on the amplitude of the measured pressure data than the phase of the data [68], as shown in Fig. 6.13. Therefore, the reconstution of $\mathbf{c}$, which is mainly dependent on the phase of the data, is less affectd by the acoustic attenuation than the reconstruction of $\mathbf{A}$, which depends on both the phase and amplitude of the measured data.

Effects of SIR: In reality, ultrasonic transducers always have finite aperture size, and the finite size effects can be described by the SIR of the transducer, which accounts for the averaging effect over the transducer surface [45,149]. To investigate the effects of neglecting SIR, simulated PA data were first generated on a grid with a pitch of 0.1 mm and recorded by 4000 transducers that were evenly distributed on the sides of a square with side length 100 mm. The recorded data from every 20 consecutive transducers were then averaged to emulate the SIR effects of a 2 mm line transducer. By use of the averaged data, JR was conducted with regularization parameters $\lambda_A = 10^{-3}$ and $\lambda_c = 10^{-2}$. Figure 6.15 displays the JR results, which show that, when the transducer aperture size is small, the proposed JR method is robust to the model error of neglecting SIR.

Effects of EIR: In addition to the SIRs, ultrasonic transducers also have EIRs in practice, which model the the electrical responses of the piezoelectric transducers. Before performing JR, EIR needs to deconvolved from the measured voltage signals to recover the detected pressure data. However, the EIR of a transducer usually cannot be accurately measured. To investigate the effects of inaccurate EIR deconvolution, the simulated PA data were first convolved with an EIR of an actual transducer [23,149]. The convolved data were then deconvolved by use of a curvelet deconvolution technique [151] with an inaccurate EIR, which was produced by adding 2% Gaussian noise into the spectrum of the original EIR. Figure 6.16(a) and (b) show the inaccurate EIR compared to the original EIR and the deconvolved pressure data from one transducer compared to original pressure data, respectively. By use of the deconvolved data, JR was conducted with regularization parameters $\lambda_A = 10^{-2}$

and $\lambda_c = 10^{-1}$. Figure 6.17 displays the JR results, which show that the model error of inaccurate EIR deconvolution has larger impact on the JR results than acoustic attenuation or SIR effects. This can be explained by the fact that both the JR and EIR deconvolution are ill-conditioned problems, so small errors in the EIR measurment could be significantly amplified in the final JR results.

Effects of combined model errors: Usually, the model errors of neglecting acoustic attenuation, neglecting SIR and inaccurate EIR deconvolution all exist in practice. To investigate the effects of the combined model errors, the above procedures were repeated to first generate attenuated data, which were then averaged to emulate the SIR effects. The averaged, attenuated data were used to generate the inaccurately deconvolved data, which were employed for JR with regularization parameters $\lambda_A = 10^{-2}$ and $\lambda_c = 10^{-1}$. The JR results are displayed in the top and middle rows of Fig. 6.18. These results suggest that, even with sufficient **A**, accurate JR may not be feasible in practice due to its instability and the inevitable model errors. However, the jointly reconstructed **A** has smaller RMSE = 0.12 compared to the iterative results (the bottom row of Fig. 6.18) that was reconstructed with constant SOS of 1600 m/s and has RSME = 0.22. This shows that, even though accurate JR may not be feasible in practice, the accuracy of the reconstructed **A** can be improved by the JR method compared to the images reconstructed with a constant SOS.

Effects of deficient A : The accuracy of JR is not only affected by the model errors, but also the spatial properties of **A** and **c**. As we have seen in Section **??** and **??**, even with **A** assumed to be known exactly, the reconstructed **c** may not be accurate if **A** is deficient. Consequently, the JR may not be accurate if the heuristic conditions are not satisfied, which will be shown in this section. Figure 6.19 display a phantom of deficient **A**, which satisfies neither heuristic conditions. By use of this phantom, simulated PA data were generated, which were subsequently employed for JR with regularization parameters $\lambda_A = 10^{-3}$ and $\lambda_c = 10^{-2}$. No model error was considered here. Figure 6.20 displays the JR results, which show that, even though there are no model errors, accurate JR may not be feasible if the heuristic conditions are not satisfied.

Effects of combining model errors and deficient A : In practice, **A** could be deficient and model errors do exist. To investigate the effects of the model errors combined with deficient **A**, the above procedures were repeated to generate simulated PA data corresponding to combined model errors and deficient **A** in Fig. 6.20. By use of the simulated data, JR was conducted with regularization parameters $\lambda_A = 10^{-2}$ and $\lambda_c = 10^{-1}$. The JR results are displayed in the top and middle rows of Fig. 6.21. These JR results, again, suggest that accurate JR may not be feasible in practice due to the model errors and deficiency of **A**. The bottom row of Fig. 6.21 shows the iterative results, which were reconstructed with a constant SOS of 1600 m/s. The RMSE of the reconstructed **A** by use of the JR method and the iterative method are 0.01 and 0.02, respectively. Again, these results indicate that, even though accurate JR may not be feasible in practice, **A** can be more accurately reconstructed by the JR method than when SOS is assumed homogeneous.

6.5 Conclusion and discussion

In this chapter, we developed an optimization approach to JR of **A** and **c** in PACT that is based on the wave equation. This method was utilized to investigate the numerical properties of the JR problem and its feasibility in practice. The computer simulation results demonstrated numerical instability of the JR problem. Due to the instability, the accuracy of the JR results was strongly affected by the inevitable model errors, particularly by the inaccurate EIR deconvolution, which is also an ill-conditioned inverse problem. We also showed that the accuracy of JR results was affected by the the spatial properties of **A** and **c** as well; i.e. if **A** was deficient, the JR results might not be accurate even there was no model error. These results indicate that accurate JR in PACT may not be feasible in practice due to the model errors and deficiency of **A**. However, we also showed that the accuracy of the reconstructed **A** can still be improved by the JR method compared to the image reconstructed with a constant SOS.

Note that, although our observations and conclusions were drawn from the numerical results that were obtained by use of an alternating optimization algorithm to solve a wave-equation-based optimization problem, their validity may be independent of the apporaches employed to solve the JR problem. In previous theoretical work on the JR problem, Stefanov *et al* proved the instability of the linearized JR problem, which suggested instability of the JR problem as well [135]. This result corroborates our conclusion of the instability of the JR problem. In [134], they gave an uniqueness condition of reconstruction of $c(\mathbf{r})$ given $A(\mathbf{r})$, which is consistent with our support condition (see Therorem 3.3 therein). In previous work regarding the development of JR algorithms, Chen *et al* proposed a similar optimization-base approach to JR [18]. They solved the optimization problem by use of an optimiztion algorithm called time-reversal (TR) adjoint method. Although their algorithm was different from ours, they obtained similar results; accurate JR images were not produced when $\mathbf{A}$ is deficient, but the jointly reconstructed $\mathbf{A}$ is more accurate than the one reconstructed by use of the TR method with a constant SOS.

More similar and coherent results can be found in the works by Jiang *et al* [58, 177], in which the authors proposed an optimization approach to JR that is based on the Helmholtz equation instead of the wave equation. By use of that method, the authors observed that the accuracy of JR results was affected by the frequency band employed in the reconstruction. Specifically, the frequency ranges covering lower frequencies gave more accurate JR results than higher frequencies. This observation is implicitly contained in our heuristic k-space condition, where only low-pass filtered $\mathbf{A}$ is considered. Their observations and our k-space condition could be explained by the fact that band-pass or high-pass filted $\mathbf{A}$ is not physical because the non-negativity of $\mathbf{A}$ does not hold in those cases. Both results showed that the accuracy of JR is impacted by the spatial spectrum of $\mathbf{A}$. By employing phantoms of $\mathbf{A}$ and $\mathbf{c}$ that had the same structures and sharp boundaries (sufficient $\mathbf{A}$), the authors also showed that qualitatively accurate images of $\mathbf{A}$ and $\mathbf{c}$ can by jointly reconstructed by incorporating Marquardt and Tikhonov regularizions into reconstruction. By use of regularizations, the authors showed their algorithm was insensitive to random noise in the measurement, which is congruous with our observations. Although the reconstructed images were only qualitatively accurate, the authors showed that the jointly reconstructed $\mathbf{A}$ was more accurate than the image reconstructed with a homogeneous SOS, which is consistent with our results. In addition, they also observed that the jointly reconstructed $\mathbf{A}$ was more accurate than the jointly reconstructed $\mathbf{c}$, which, again, indicated the inverse problem of reconstructing $\mathbf{c}$ is more unstable compared to reconstruction of $\mathbf{A}$.

However, in the works mentioned above, the authors only showed the JR results produced by their proposed methods; they did not investigate how the numerical properties of the JR problem. Specifically, how the accuracy of JR results were affected by deficiency of $\mathbf{A}$ was not studied in those works. In this work, we showed that, even if there are no model errors, the accurate JR may not be achievable if $\mathbf{A}$ is deficient. Furthermore, those works did not investigate the numerical instability of the JR problem and its implication of the feasibility of accurate JR in practice. In this work, we demonstrated the numerical instability of the JR problem, and systematically studied the practical limitations of JR due to its instability and inevitable model errors.

There remain several important topics to further evaluate the proposed JR method and investigate the JR problem. In addition to computer simulations, the proposed method can be further evaluated through experimental studies, in which the JR method could be based on 3D wave equation instead of 2D wave equation. Since line search is inevitable in any nonlinear optimization algorithm that is employed to reconstruct $\mathbf{c}$ given $\mathbf{A}$, the intensive computational burden is a challenge for 3D JR. Also, in this study, the proposed JR method is based on the wave equation in lossless fluid media where the mass density is assumed to be homogenous. However, in many applications, density variation and/or acoustic absorption is not negligible [52, 53]. In some cases, for example transcranial PACT brain imaging of primates, shear wave mode conversion needs to be taken into account as well. The development of the JR method, which is based on the wave equation that describes density variation, acoustic absorption and/or shear wave mode conversion, is another important topic for future studies. Finally, due to the instability of the JR problem, additional priori information besides the regularization terms needs to be incorporated into reconstruction in order to achieve accurate JR. Ultrasound computed tomography (USCT) is a natural candidate to provide such information since the USCT signals can be acquired by the same system used in PACT. The investigation of the JR problem by combining PACT and USCT is underway.

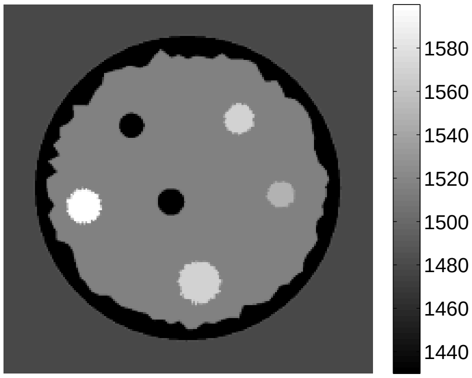

Figure 6.1: The numerical phantom representing the SOS distribution $\mathbf{c}$ in a breast.

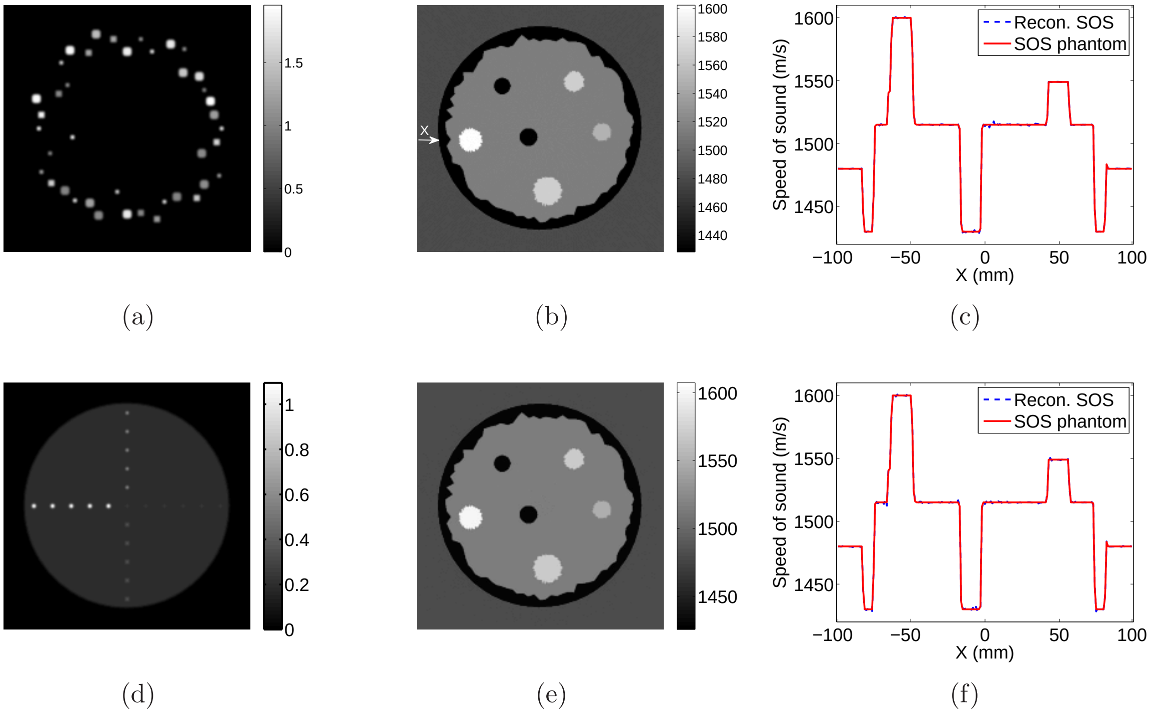

(a) (b) (c)

(d) (e) (f)

Figure 6.2: Given ‘adequate’ $\mathbf{A}$ in the left column, the reconstructed $\mathbf{c}$ are shown in the middle column. Right column are the corresponding profiles.

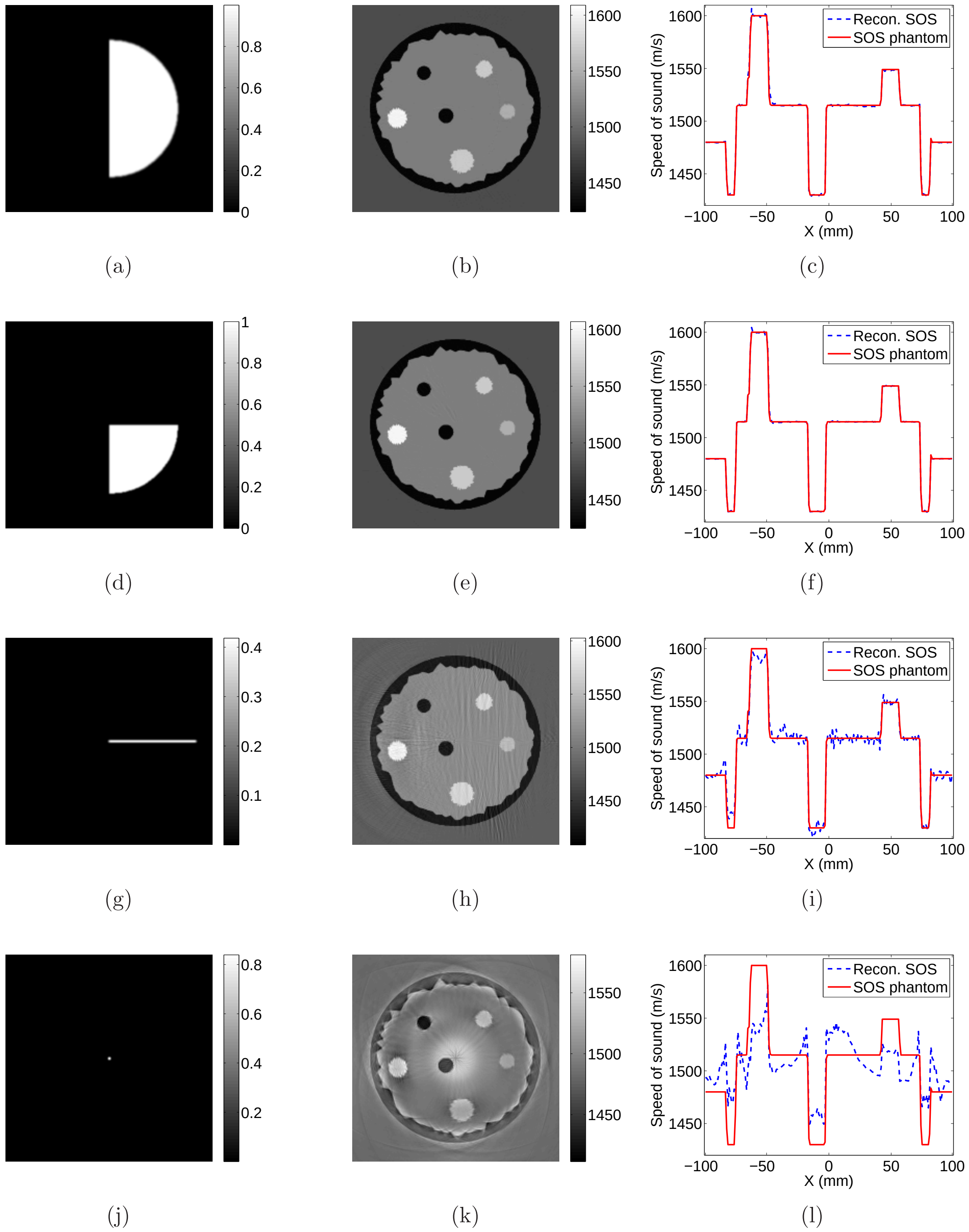

Figure 6.3: Given ‘defective’ **A** in the left column, the reconstructed **c** are shown in the middle column. Right column are the corresponding profiles.

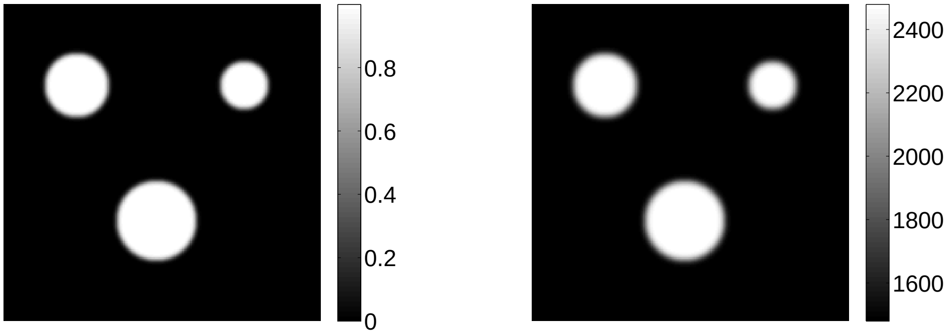

(a) (b)

Figure 6.4: Numerical phantom of **A** (panel (a)) and **c** (panel (c)) used to investigate the effects of spatial frequency contents of **A** on the reconstruction of **c**.

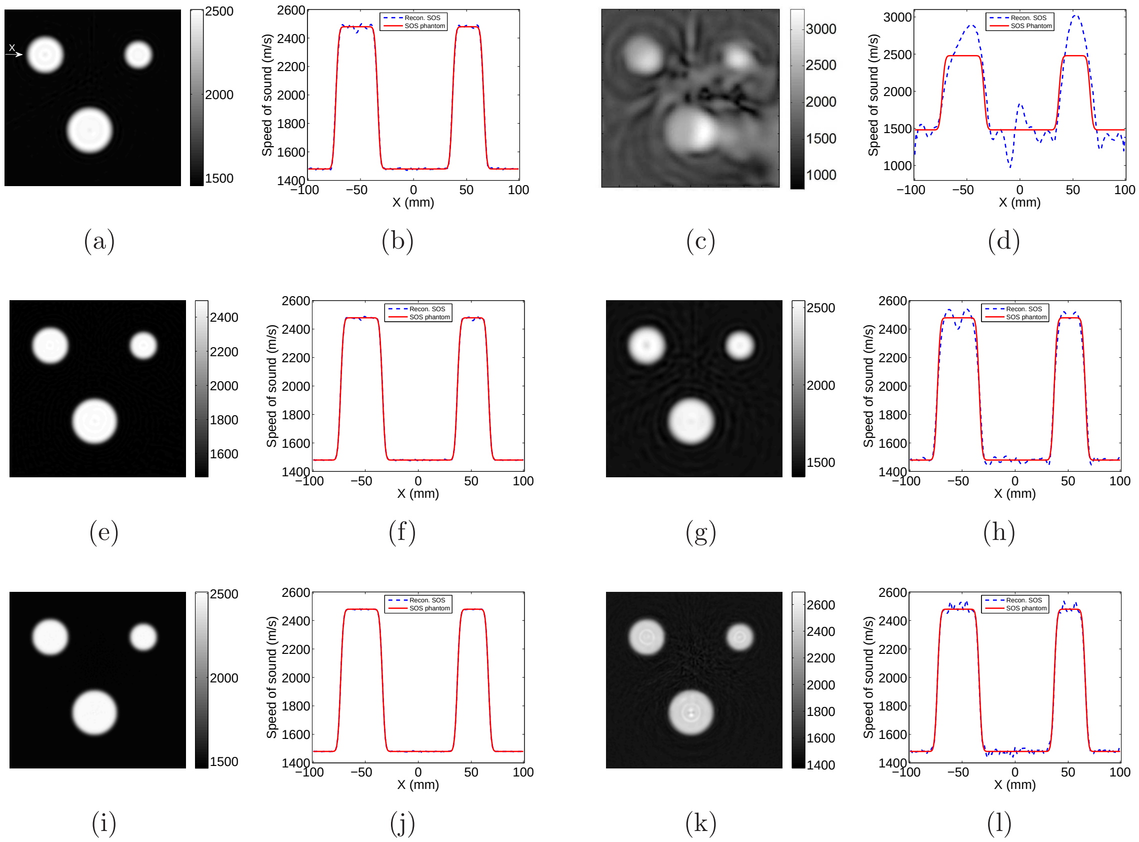

(a) (b) (c) (d)

(e) (f) (g) (h)

(i) (j) (k) (l)

Figure 6.5: Each row is reconstructed **c** and their profiles corresponds to different bandwidth ratios of **A** to **c**. From top to bottom, the ratios are 0.25, 0.44, and 1.0, respectively. The first and second columns are the noiseless results and the third and fourth columns are noisy results.

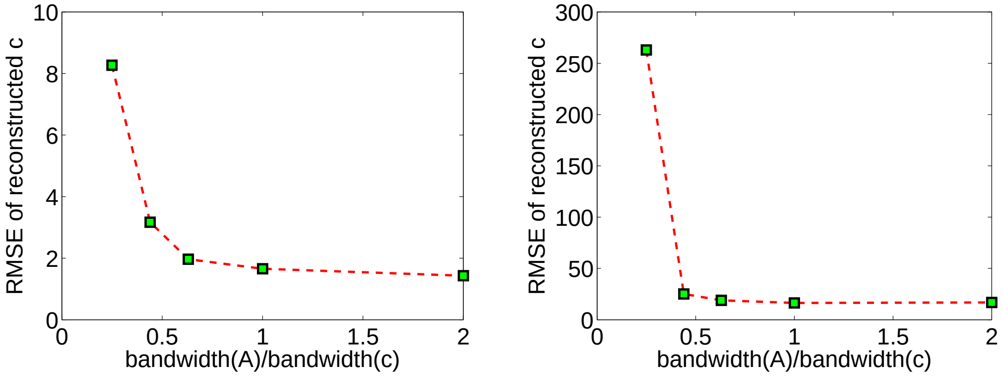

(a) (b)

Figure 6.6: RMSE of reconstructed $\mathbf{c}$ versus bandwidth ratio of $\mathbf{A}$ to $\mathbf{c}$ curves. Panel (a) and (b) correspond to the noiseless and noisy results, repectively.

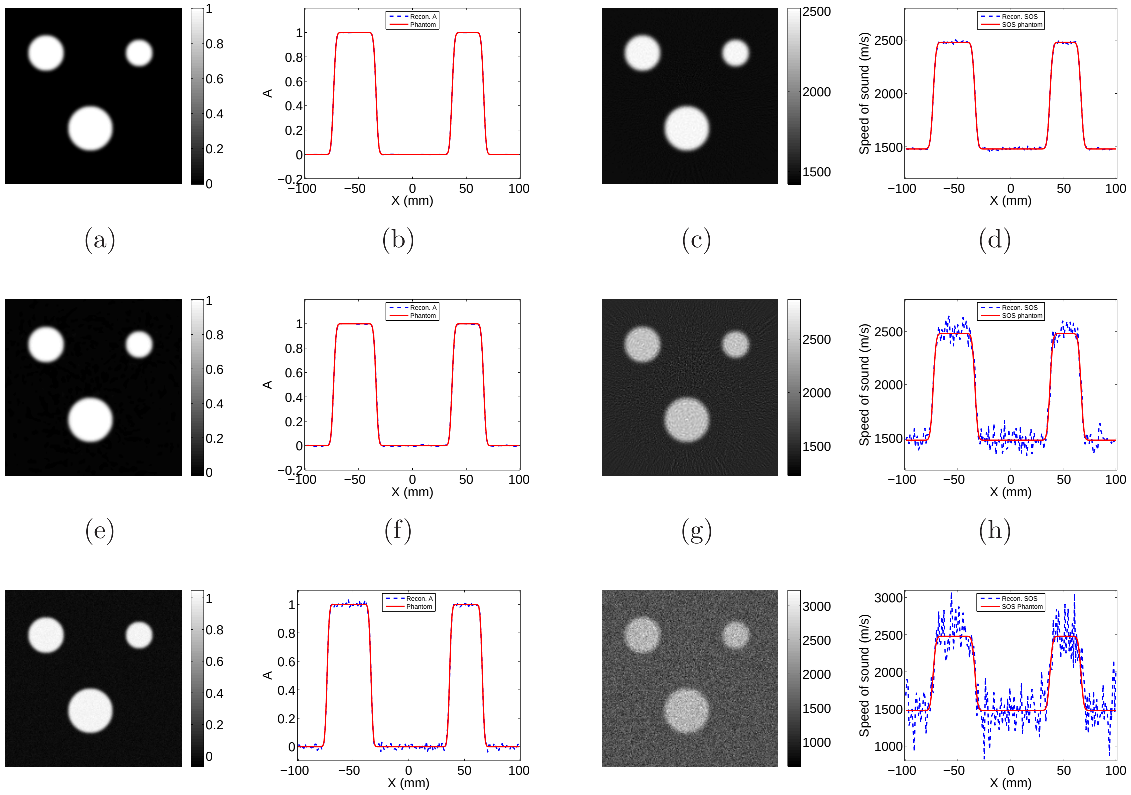

(a) (b) (c) (d)

(e) (f) (g) (h)

(i) (j) (k) (l)

Figure 6.7: The first and second columns are reconstructed **A** corresponding to perturbed **c**, and the third and fourth columns are reconstructed **c** corresponding to perturbed **A**. From the top to the bottom row, the perturbation, which is measured as relative error, is 0.2%, 1.0% and 5.0%, respectively.

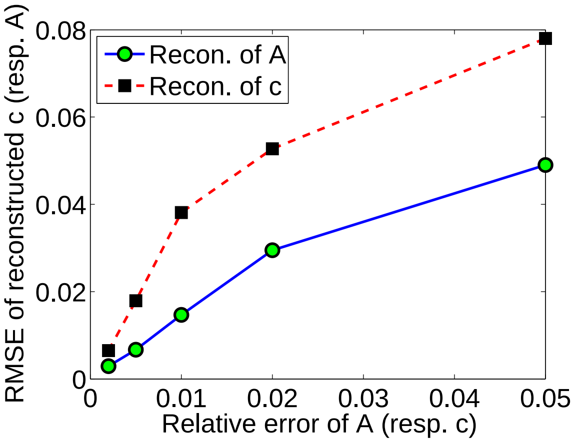

Figure 6.8: RMSE of reconstructed $\mathbf{A}$ (resp. $\mathbf{c}$) versus relative error of $\mathbf{c}$ (resp. $\mathbf{A}$).

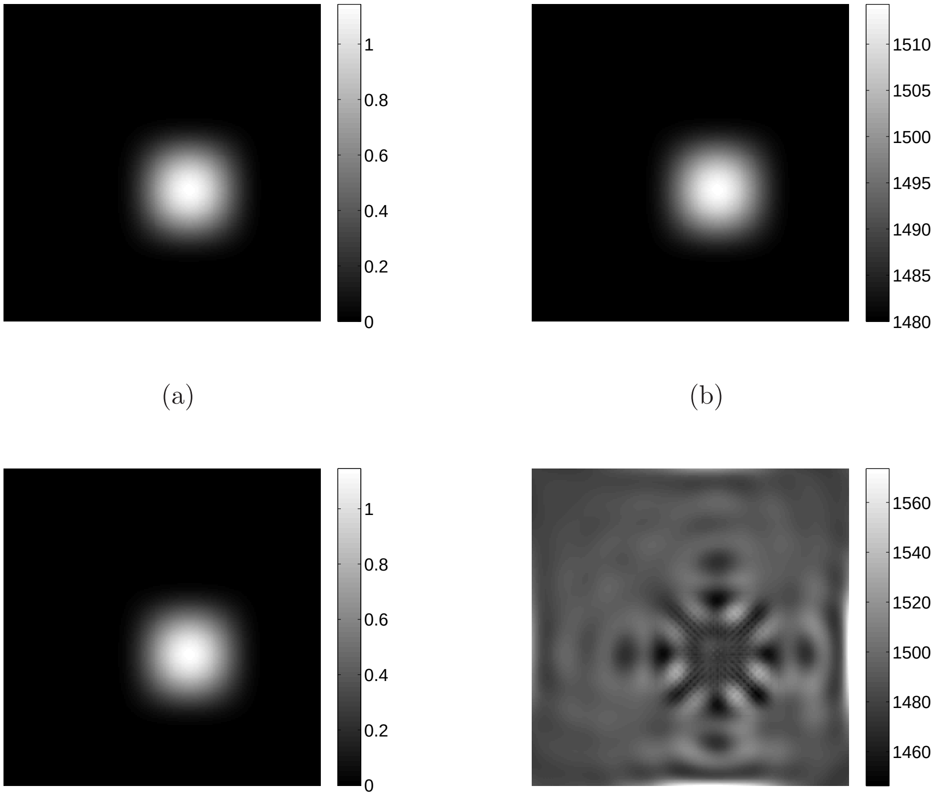

(a) (b)

(c) (d)

Figure 6.9: Numerical phantoms of $\mathbf{A}$, $\mathbf{A}_1$ in panel (a) and $\mathbf{A}_2$ in panel (c), are used to reconstruct $\mathbf{c}$, $\mathbf{c}_1$ in panel (b) and $\mathbf{c}_2$ panel (d), from identical measured data. While $\mathbf{A}_1$ and $\mathbf{A}_2$ are similar, the reconstructed $\mathbf{c}_1$ and $\mathbf{c}_2$ are quite different.

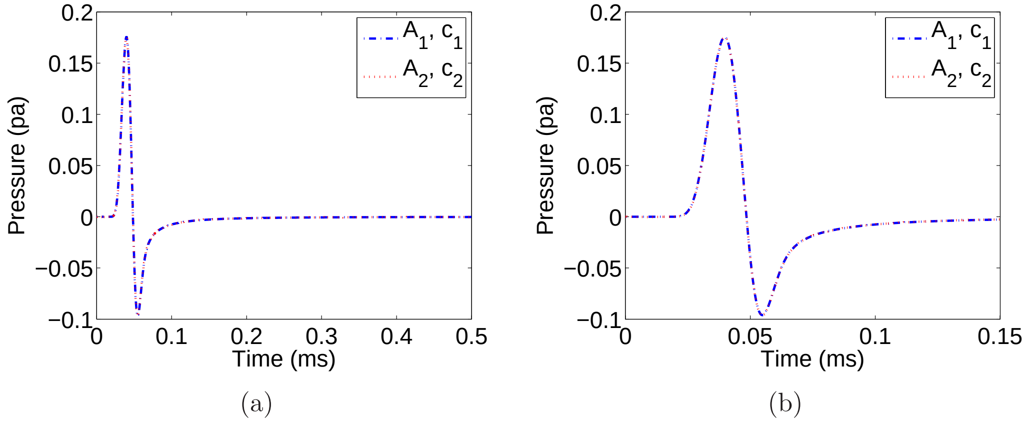

(a) (b)

Figure 6.10: Identical pressure data (from one transducer) generated from the phanatoms in Fig. 6.9. Panel (b) is the zoomed-in detail of panel (a).

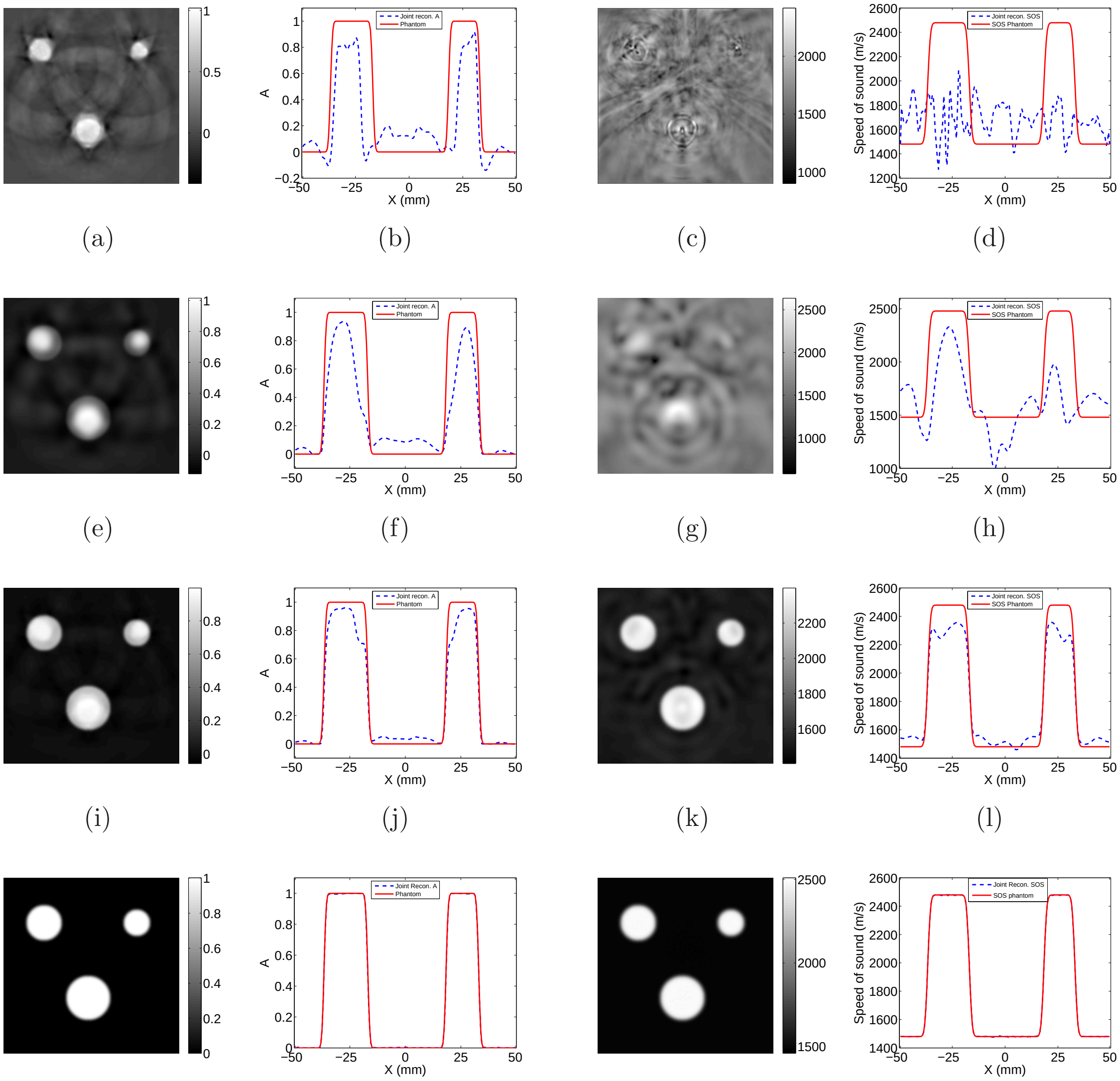

(a) (b) (c) (d)

(e) (f) (g) (h)

(i) (j) (k) (l)

(m) (n) (o) (p)

Figure 6.11: Jointly reconstructed images corresponding to noiseless data. Each row corresponds to different regularization parameters λ_A and λ_c. From top to bottom, λ_A and λ_c are 0, 10^{-5}, 10^{-4}, 10^{-3}, and 0, 10^{-4}, 10^{-3}, 10^{-2}, respectively. The first and second columns are reconstructed $\mathbf{A}$ and the third and fourth columns are reconstructed $\mathbf{c}$.

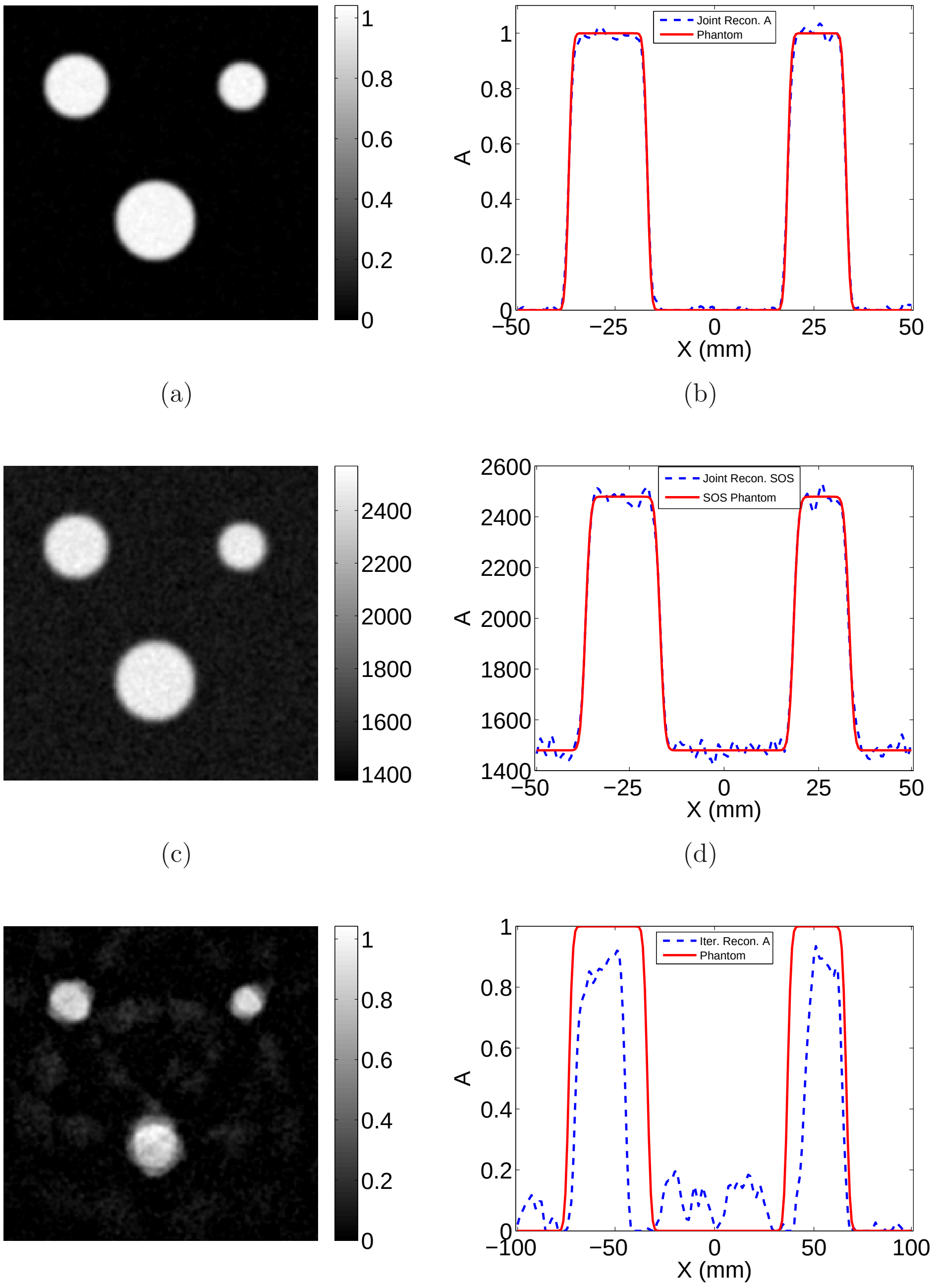

(a) (b)

(c) (d)

(e) (f)

Figure 6.12: Reconstructed images corresponding to noisy data. The top and middle rows are the jointly reconstructed $\mathbf{A}$ and $\mathbf{c}$, respectively. The bottom row is the $\mathbf{A}$ reconstructed by an iterative method assuming a constant SOS.

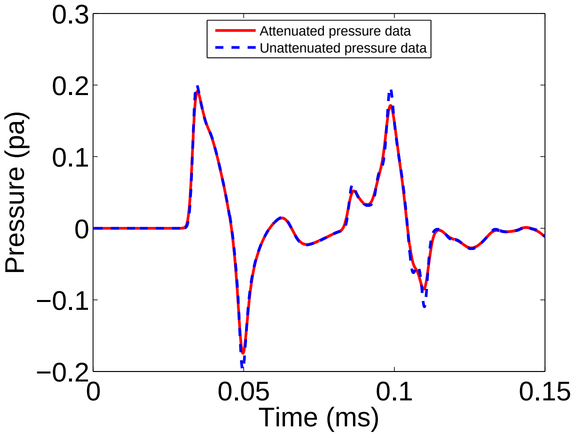

Figure 6.13: Attenuated pressure data from one transducer compared to the unattenuated data.

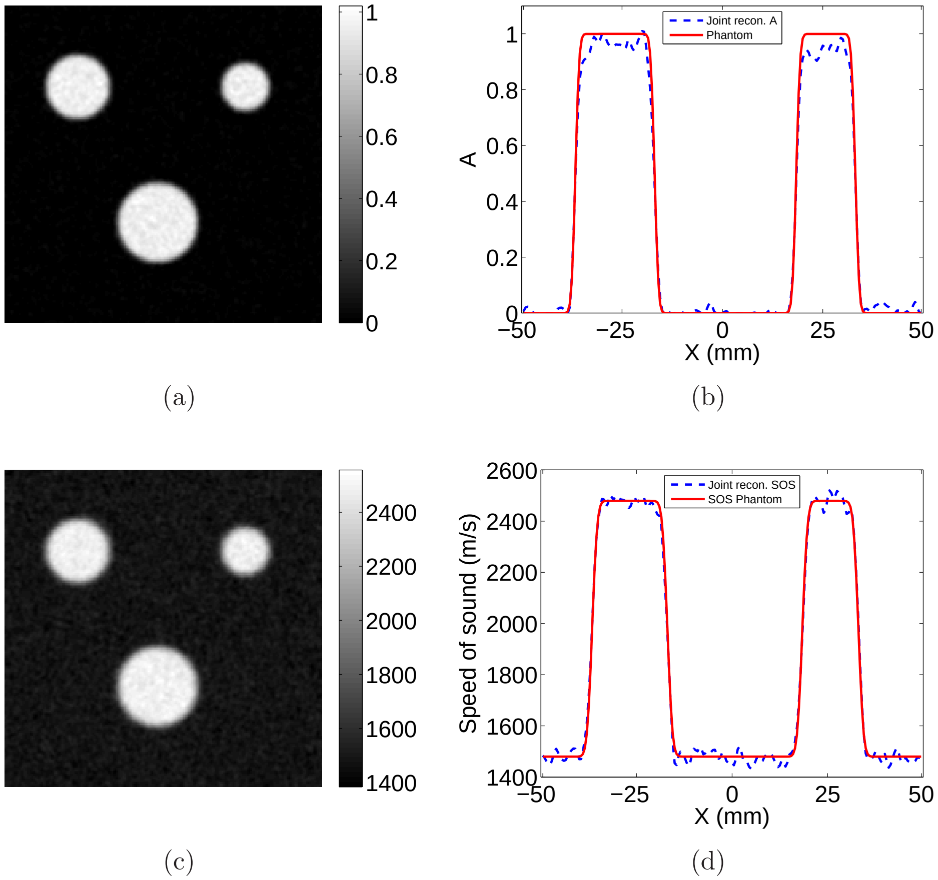

(a) (b)

(c) (d)

Figure 6.14: Jointly reconstructed images corresponding to model error of neglecting acoustic attenuation. The top and bottom rows are the reconstructed **A** and **c**, respectively.

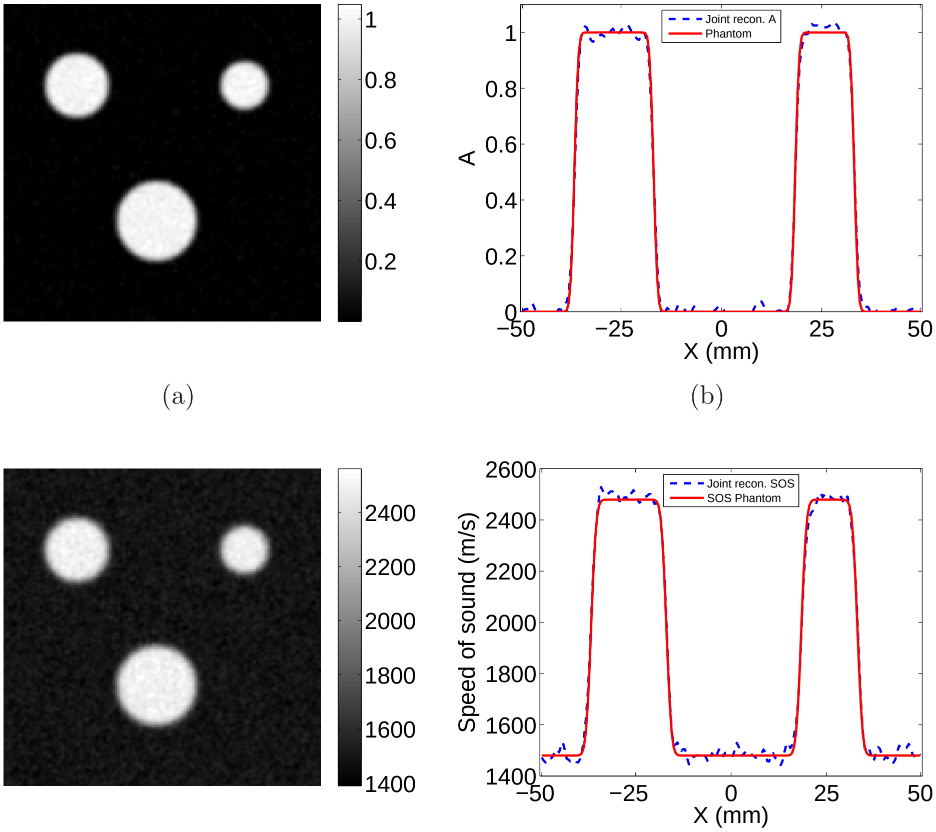

(a) (b)

(c) (d)

Figure 6.15: Jointly reconstructed images corresponding to model error of neglecting SIR. The top and bottom rows are the reconstructed **A** and **c**, respectively.

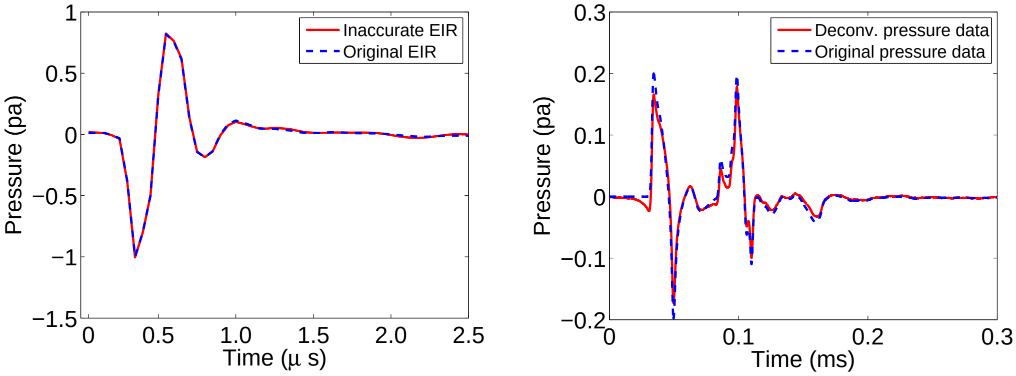

(a) (b)

Figure 6.16: Panel (a): inaccurate EIR compared to the original EIR. Panel (b): deconvolved pressure data by use of the inaccurate EIR compared to original pressure data.

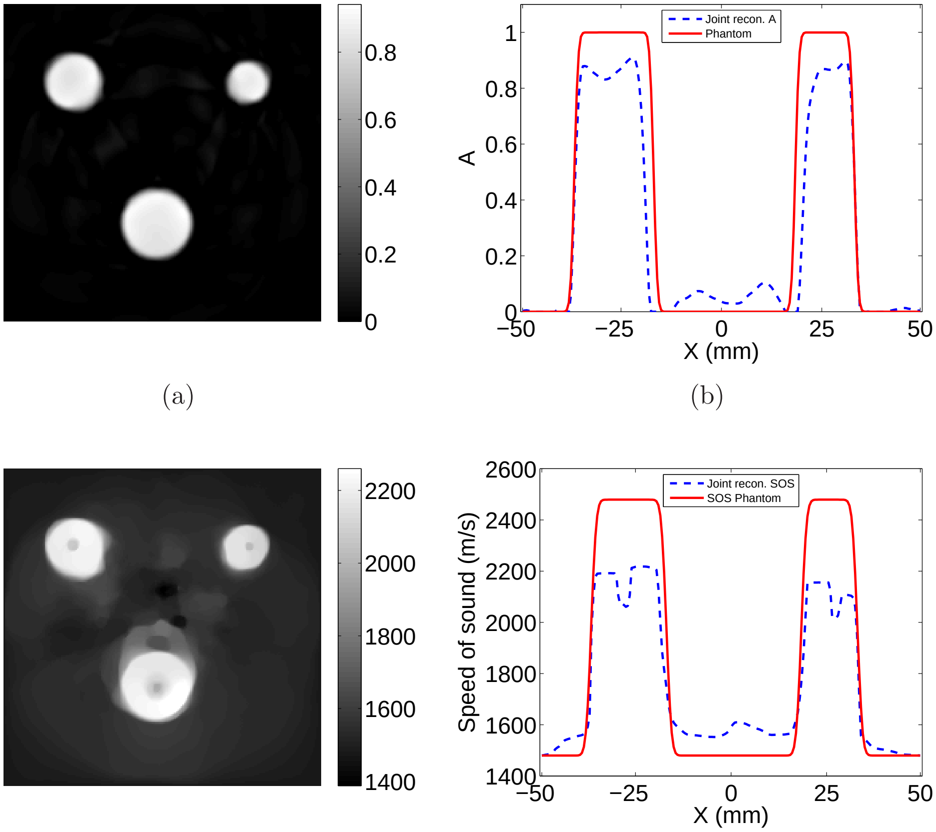

(a) (b)

(c) (d)

Figure 6.17: Jointly reconstructed images corresponding to model error of inaccurate EIR deconvolution. The top and bottom rows are the reconstructed **A** and **c**, respectively.

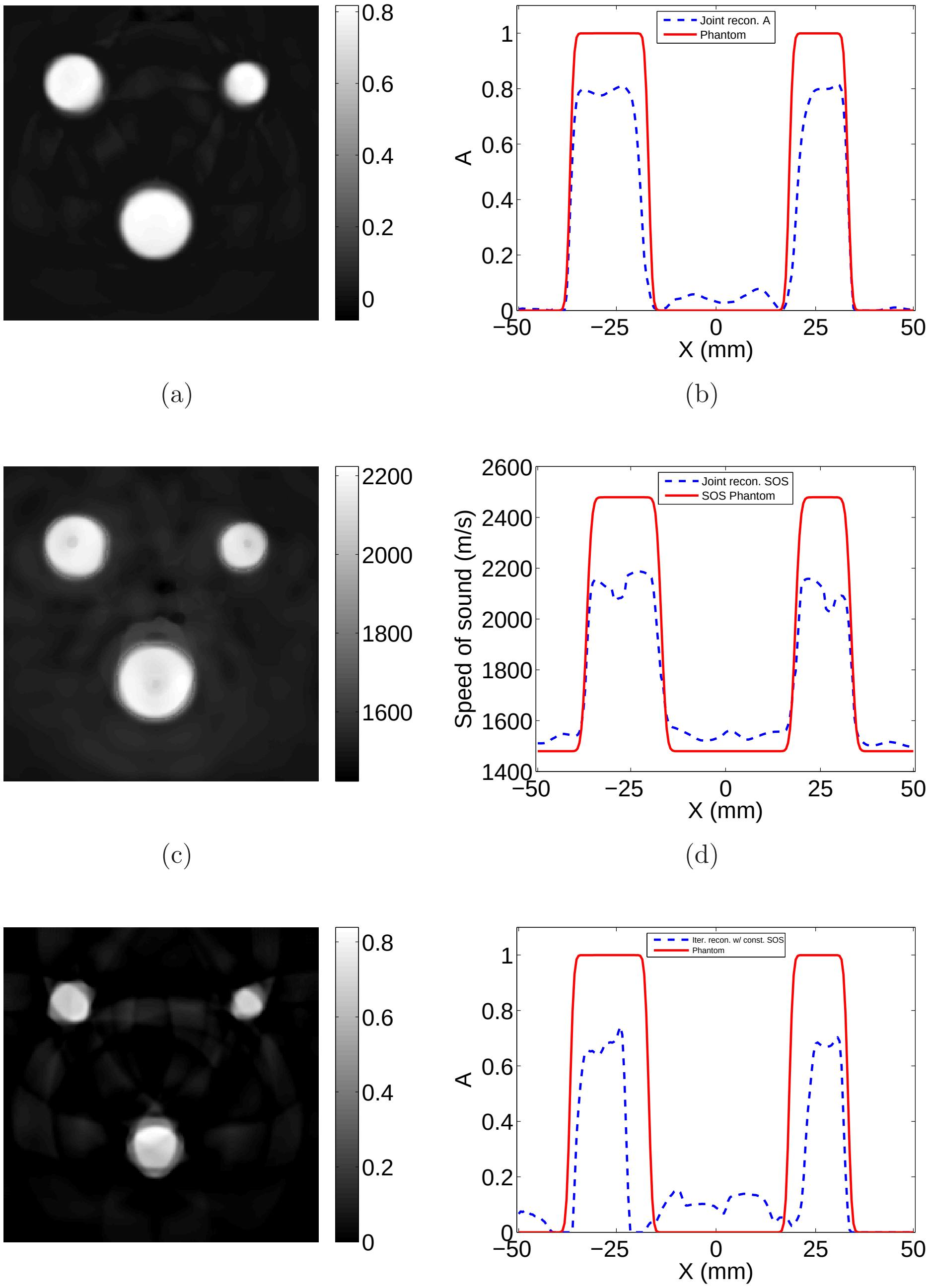

(a) (b)

(c) (d)

(e) (f)

Figure 6.18: Jointly reconstructed images corresponding to combined model errors of neglecting acoustic attenuation, SIR and inaccurate EIR deconvolution. The top and bottom rows are the reconstructed **A** and **c**, respectively.

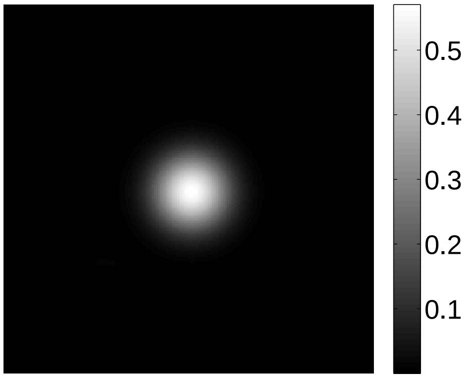

Figure 6.19: The numerical phantom representing a deficient **A**.

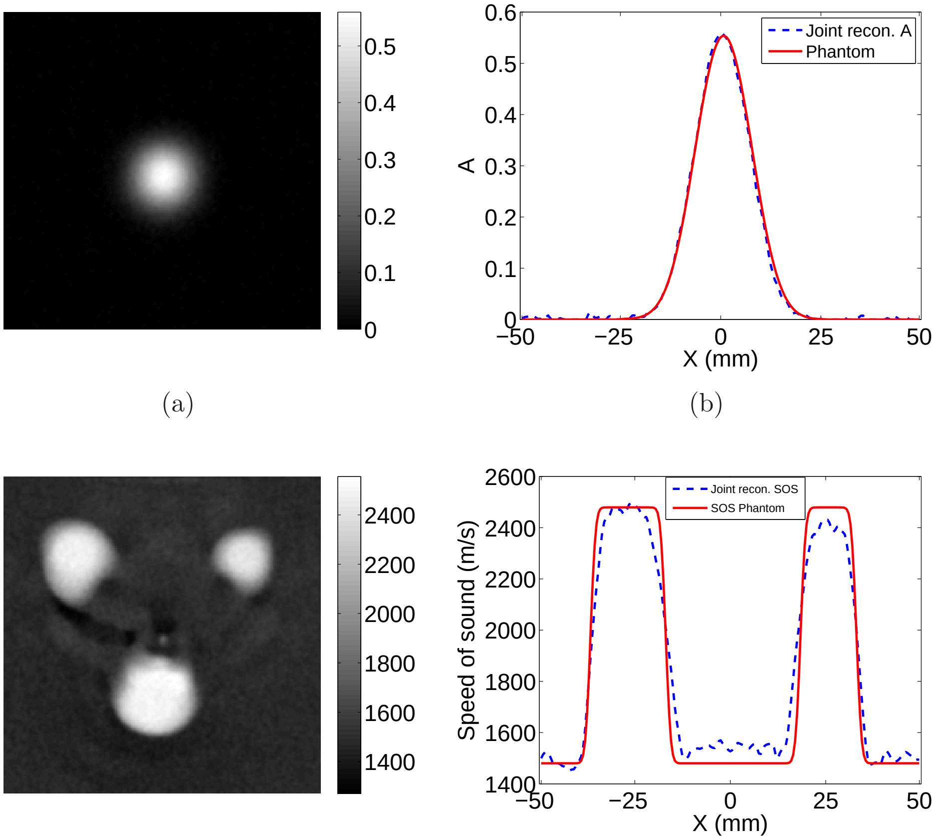

(a) (b)

(c) (d)

Figure 6.20: Jointly reconstructed images corresponding to deficient **A** in Fig. 6.19. The top and bottom rows are the reconstructed **A** and **c**, respectively.

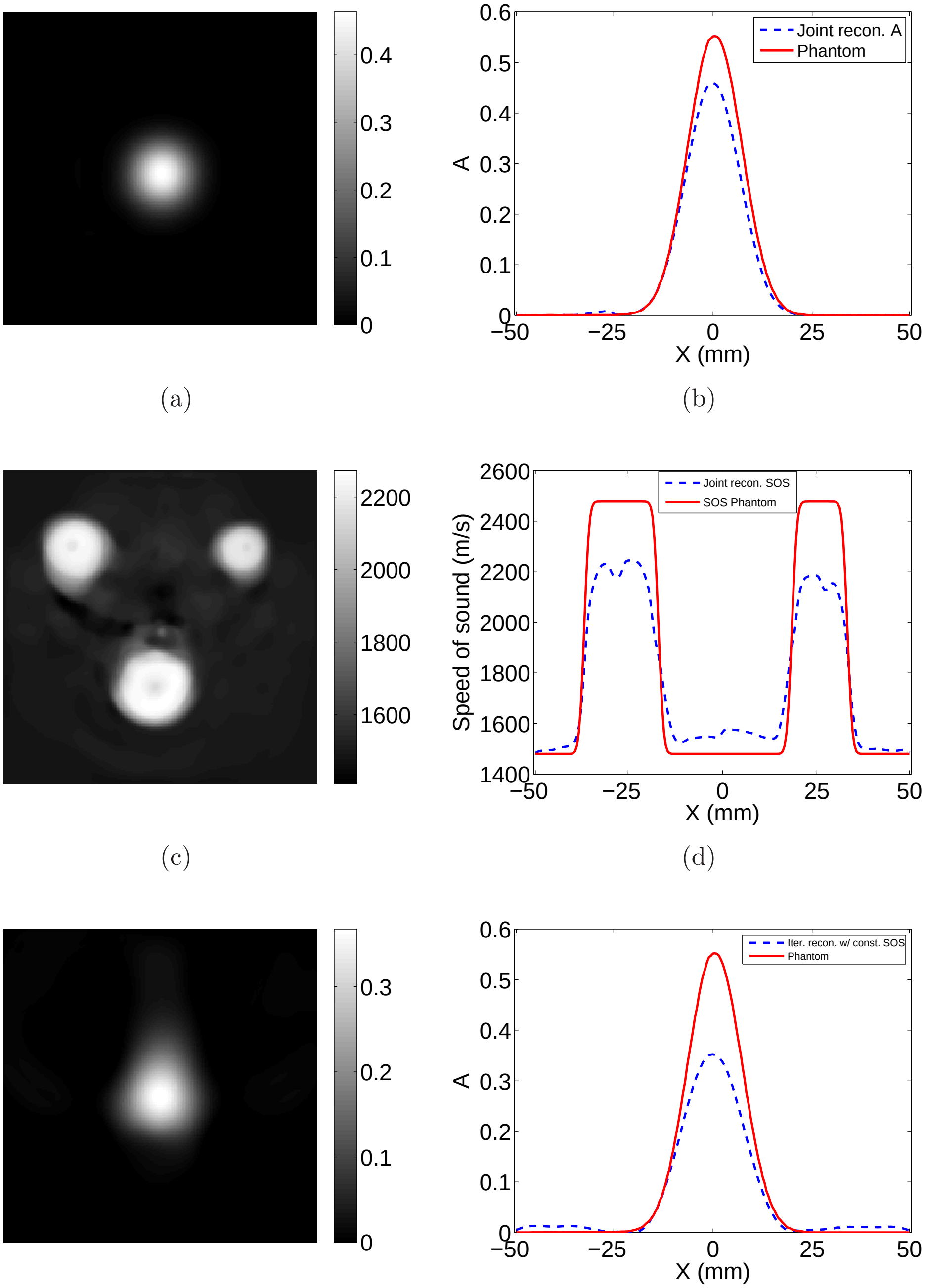

(a) (b)

(c) (d)

(e) (f)

Figure 6.21: Reconstructed images corresponding to $\mathbf{A}$ in Fig. 6.19. The top and middle rows are the jointly reconstructed $\mathbf{c}$ and $\mathbf{A}$, respectively. The bottom row is the $\mathbf{A}$ reconstructed by an iterative method assuming a constant SOS.

Chapter 7

Summary

In the dissertation, we have developed and investigated image reconstruction methods for photoacoustic computed tomography (PACT) with acoustically heterogeneous media. The contributions are summarized as following.

1. We have investigated the use of a time-reversal algorithm for PACT image reconstruction that can compensate for acoustic attenuation in heterogeneous lossy acoustic media [53].
2. We have developed a subject-specific image reconstruction methodology for transcranial PACT to compensate for aberrations in the measured PA data induced by the skull. Adjunct x-ray CT data are employed to infer the spatially variant SOS and density distributions of the skull, which are subsequently utizlied by the TR image reconstruction algorithm to mitigate skull-induced distortions in the reconstructed image. Our preliminary experimental results show that employed a primate skull demonstrated that the reconstruction methodology can produce images with improved fidelity and reduced artifact levels as compared to a previously employed back-projection algorithm [52].
3. We have developed and investigated a discrete imaging model for PACT that is based on the exact PA wave equation. The k-space pseudospectral method is adopted for implementing the forward and backprojection operators associated with the discrete imaging model. By use of the projection operators, an iterative image reconstruction algorithm is implemented and investigated in computer-simulation and experimental studies of PACT in inhomogeneous acoustic media. The results demonstrated that

the reconstruction methodology can effectively mitigate image artifacts due to data incompleteness, noise, finite sampling, and modeling errors [51].

4. We have developed an optimization-based reconstruction approach to JR of $A(\mathbf{r})$ and $c(\mathbf{r})$ that is based on the wave equation. The developed reconstruction method was utilized to investigate the numerical properties of the JR problem and its feasibility in practice. The computer simulation results demonstrated numerical instability of the JR problem. Due to the instability, the accuracy of the JR results was strongly affected by the inevitable model errors. We also showed that the accuracy of JR results was affected by the the spatial properties of $A(\mathbf{r})$ and $c(\mathbf{r})$ as well. These results indicate that accurate JR in PACT may not be feasible in practice However, we also showed that the accuracy of the reconstructed $\mathbf{A}$ can still be improved by the JR method compared to the image reconstructed with a constant SOS.

Appendix A

Validation of Speed-of-Sound and Density Maps

The density and speed of sound of the skull were also directly measured to corrorborate the accuracy of the adopted method for estimating the skull's SOS and density distributions from X-ray CT data. By using the water displacement method, the measured average density of the monkey skull $\bar{\rho}_{wd}$ is 1890 kg/m^3. The average denisty of the skull $\bar{\rho}_{ct}$ can also be estimated from CT data:

$$\bar{\rho}_{ct} = \frac{\sum_k \Phi_k \rho^w + (1 - \Phi_k)\rho^s}{N}, \tag{A.1}$$

where $\rho^w = 1000$ kg/m^3 is the density of water, $\rho^s = 2100$ kg/m^3 is the density of skull [9,37], Φ_k is the porosity of the k^{th} pixel of the skull, and N is the total number of pixels of the skull in the CT image. The estimated average denisty of the skull $\bar{\rho}_{ct} = 1910$ kg/m^3, which is very close (about 1%) to the measured value $\bar{\rho}_{wd} = 1890$ kg/m^3.

The SOS in the skull was measured using a photoacoustic approach, as shown in Fig. 4.2-(b). A laser beam was split by use of a beam splitter and directed by mirrors to two convex lenses. The two convex lenses (NA≈0.04, depth of focus ∼300 mm) focused the laser beam on the inner and outer surface of the skull, and the line connecting the two focused beam spots (∼80 microns) was perpendicular to the skull surface. The ultrasonic transducer was placed coaxially with the laser spots; therefore, the average SOS $\bar{c}_{pa}$ between the two laser spots was calculated by:

$$\bar{c}_{pa} = \frac{h}{\frac{h}{c^w} - t_d}, \tag{A.2}$$

Table A.1: The measured average SOS $\bar{c}_{pa}$ via the PA experiment (column 2) and the estimated average SOS $\bar{c}_{ct}$ from the CT measurements (column 3) for the five measurement locations (see Fig. 4.1-(a)).

Position	SOS (PA) in m/s	SOS (CT) in m/s
1	2790 ± 90	2720
2	2740 ± 80	2830
3	2780 ± 60	2860
4	2620 ± 100	2720
5	2590 ± 160	2430

where t_d is the time delay between the PA signals from the inner and outer surfaces of the skull, $c^w = 1480$ m/s is the speed of sound in water, and h is the thickness of the skull at the laser spots. We measured $\bar{c}_{pa}$ at the 5 locations on the skull that are indicated in Fig. 4.1-(a). The measured SOS values are displayed in the second column of Table 1.

The corresponding average SOS values were also computed by use of the X-ray CT image data and compared to the measured values. In order to determine the 5 locations on the CT image that correspond the measurement locations described above, we measured the arc lengths between the fiducial markers and the measured locations. Then the average SOS $\bar{c}_{ct}$ at these locations can be estimated from CT data (derived from Eq. (4.3)):

$$\bar{c}_{ct} = \frac{h}{\sum_i \frac{d}{\Phi_i c^w + (1-\Phi_i) c^s}}, \tag{A.3}$$

where Φ_i is the porosity of the i^{th} pixels on the line connecting the two laser spots, and is calculated from bilinear interpolation of the neighbor pixel values in the CT image; $c^s = 2900$ m/s is the speed of sound of skull bone [9, 37], and $d = 0.1$ mm is the resolution of the CT image. The estimated SOS at these locations are shown in the last column of Table 1. The root mean square difference between the SOS inferred from the PA experiment and the SOS inferred from the CT data is 105 m/s.

Appendix B

Modeling transducer impulse responses

An important feature of the proposed discrete PACT imaging model is that the transducer's impulse responses, including the spatial impulse response (SIR) and the acousto-electrical impulse response (EIR), can be readily incorporated into the system matrix.

The SIR accounts for the averaging effect over the transducer surface [8, 45, 149], which can be described as

$$\hat{p}^{\mathrm{SIR}}(\mathbf{r}_l^d, m\Delta t) = \frac{\int_{S(\mathbf{r}_l^d)} \mathrm{d}S(\mathbf{r}_l')p(\mathbf{r}_l', m\Delta t)}{S(\mathbf{r}_l^d)}, \tag{B.1}$$

where $\hat{p}^{\mathrm{SIR}}(\mathbf{r}_l^d, m\Delta t)$ is the averaged pressure at time $t = m\Delta t$ over the surface of the l-th transducer, $S(\mathbf{r}_l^d)$ is the surface area of the l-th transducer centered at $\mathbf{r}_l^d$.

In order to incorporate the SIR into the system matrix, we can divide the transducer surface into K small patches with equal area ΔS that is much less than the acoustic wavelength, so the integral in Eqn. B.1 can be approximated by summation as

$$\hat{p}^{\mathrm{SIR}}(\mathbf{r}_l^d, m\Delta t) \simeq \sum_{k=1}^{K} p(\mathbf{r}_l^k, m\Delta t)\frac{\Delta S}{S(\mathbf{r}_l^d)}, \tag{B.2}$$

or in the equivalent matrix form

$$\hat{p}^{\mathrm{SIR}}(\mathbf{r}_l^d, m\Delta t) \simeq \boldsymbol{\gamma}^{\mathrm{SIR}}\hat{\mathbf{p}}_m^l \tag{B.3}$$

where $\mathbf{r}_l^k$ denotes the center of the k-th patch of the l-th transducer, ΔS is the patch area, $\boldsymbol{\gamma}^{\mathrm{SIR}} \equiv \frac{\Delta S}{S(\mathbf{r}_l^d)}(1, \cdots, 1)$ is a $1 \times K$ vector, $\hat{\mathbf{p}}_m^l = (p(\mathbf{r}_l^1, m\Delta t), \cdots, p(\mathbf{r}_l^K, m\Delta t))^{\mathrm{T}}$ denotes the acoustic pressure at patches of l-th transducer at time $m\Delta t$. Here for simplicity, we assume all the transducers are divided into K patches with equal area ΔS, and it is readily to extend to general cases where l-th transducer is divided into K_l patches with area of ΔS_{lk}.

Recalling the measured pressure data $\hat{\mathbf{p}}_m$ and $\hat{\mathbf{p}}$ defined for point-like transducer, we can redefine $\hat{\mathbf{p}}_m$ as a $KL \times 1$ vector that represents the acoustic pressure at patches of transducers with finite area at time $t = m\Delta t$ as

$$\hat{\mathbf{p}}_m \equiv \begin{bmatrix} \hat{\mathbf{p}}_m^1 \\ \vdots \\ \hat{\mathbf{p}}_m^L \end{bmatrix}. \tag{B.4}$$

The corresponding $\hat{\mathbf{p}}$ can be redefine as a $KLM \times 1$ vector denoting the measured pressure data corresponding to all transducer and temporal samples as

$$\hat{\mathbf{p}} \equiv \begin{bmatrix} \hat{\mathbf{p}}_0 \\ \vdots \\ \hat{\mathbf{p}}_{M-1} \end{bmatrix}. \tag{B.5}$$

The averaged pressure measured by all transducer and temporal samples can be defined as the $LM \times 1$ vector

$$\hat{\mathbf{p}}^{\mathrm{SIR}} \equiv \begin{bmatrix} \hat{\mathbf{p}}_0^{\mathrm{SIR}} \\ \vdots \\ \hat{\mathbf{p}}_{M-1}^{\mathrm{SIR}} \end{bmatrix}. \tag{B.6}$$

where the $L \times 1$ vector

$$\hat{\mathbf{p}}_m^{\mathrm{SIR}} \equiv \begin{bmatrix} \hat{p}^{\mathrm{SIR}}(\mathbf{r}_1^d, m\Delta t) \\ \vdots \\ \hat{p}^{\mathrm{SIR}}(\mathbf{r}_L^d, m\Delta t) \end{bmatrix}. \tag{B.7}$$

According to Eqn. B.3, $\hat{\mathbf{p}}$ and $\hat{\mathbf{p}}^{\mathrm{SIR}}$ can be related as

$$\hat{\mathbf{p}}^{\mathrm{SIR}} = \boldsymbol{\Gamma}^{\mathrm{SIR}} \hat{\mathbf{p}} \tag{B.8}$$

where the $KLM \times LM$ matrix

$$\mathbf{\Gamma}^{\mathrm{SIR}} \equiv \begin{bmatrix} \boldsymbol{\gamma}^{\mathrm{SIR}} & \mathbf{0}_{1\times K} & \cdots & \mathbf{0}_{1\times K} \\ \mathbf{0}_{1\times K} & \boldsymbol{\gamma}^{\mathrm{SIR}} & \cdots & \mathbf{0}_{1\times K} \\ \vdots & \vdots & \ddots & \vdots \\ \mathbf{0}_{1\times K} & \mathbf{0}_{1\times K} & \cdots & \boldsymbol{\gamma}^{\mathrm{SIR}} \end{bmatrix}. \tag{B.9}$$

The EIR models the electrical response of the piezoelectric transducer. With the assumption that the transducer is a linear shift invariant system with respect to the input averaged pressure time sequence, the output voltage signal is the convolution result of the input and the EIR.

For simplicity, the transducers are assumed to process identical EIR, and let $\mathbf{h}^e = (h_1^e, \cdots, h_J^e)^{\mathrm{T}}$ be the discrete samples of the EIR. The input averaged pressure time sequence of the l-th transducer can be defined as a $L \times 1$ vector $\hat{\mathbf{p}}_{\mathrm{SIR}}^l \equiv (\hat{p}^{\mathrm{SIR}}(\mathbf{r}_l^d, 0), \cdots, \hat{p}^{\mathrm{SIR}}(\mathbf{r}_l^d, (M-1)\Delta t))^{\mathrm{T}}$. Then the output voltage signal $\hat{\mathbf{p}}_l^{\mathrm{IR}}$ of the l-th transducer can be expressed as a $(J+M-1)\times 1$ vector

$$\hat{\mathbf{p}}_l^{\mathrm{IR}} = \mathbf{h}^e * \hat{\mathbf{p}}_{\mathrm{SIR}}^l, \tag{B.10}$$

where $*$ denotes discrete linear convolution operation, which can be constructed as a matrix multiplication by converting one of the operands into the corresponding Toeplitz matrix.

The output voltage signals of all transducers $\hat{\mathbf{p}}^{\mathrm{IR}} \equiv (\hat{\mathbf{p}}_1^{\mathrm{IR}}, \cdots, \hat{\mathbf{p}}_L^{\mathrm{IR}})^{\mathrm{T}}$ can then be computed as

$$\hat{\mathbf{p}}^{\mathrm{IR}} = \mathbf{\Gamma}^{\mathrm{EIR}} \hat{\mathbf{p}}^{\mathrm{SIR}} \tag{B.11}$$

where the $L(J+M-1) \times LM$ matrix

$$\mathbf{\Gamma}^{\mathrm{EIR}} \equiv \begin{bmatrix} \boldsymbol{\gamma}^{\mathrm{EIR}} \\ \vdots \\ \boldsymbol{\gamma}^{\mathrm{EIR}} \end{bmatrix} \tag{B.12}$$

and $\boldsymbol{\gamma}^{\mathrm{EIR}}$ is a $(J+M-1)\times LM$ Toeplitz-like matrix defined as

$$\boldsymbol{\gamma}^{\mathrm{EIR}} \equiv \begin{bmatrix} h_1^e & \mathbf{0}_{1\times(L-1)} & 0 & \cdots & 0 & \mathbf{0}_{1\times(L-1)} & 0 \\ \vdots & \vdots & h_1^e & \vdots & \vdots & \vdots & \vdots \\ h_J^e & \vdots & \vdots & \vdots & 0 & \mathbf{0}_{1\times(L-1)} & 0 \\ 0 & \mathbf{0}_{1\times(L-1)} & h_J^e & \cdots & h_1^e & \mathbf{0}_{1\times(L-1)} & 0 \\ 0 & \mathbf{0}_{1\times(L-1)} & 0 & \cdots & \vdots & \vdots & h_1^e \\ \vdots & \vdots & \vdots & \vdots & h_J^e & \vdots & \vdots \\ 0 & \mathbf{0}_{1\times(L-1)} & 0 & \cdots & 0 & \mathbf{0}_{1\times(L-1)} & h_J^e \end{bmatrix} \tag{B.13}$$

By use of Eqns. (**??**), (B.8), and (B.11), it is readily found that

$$\hat{\mathbf{p}}^{\mathrm{IR}} = \boldsymbol{\Gamma}^{\mathrm{EIR}}\boldsymbol{\Gamma}^{\mathrm{SIR}}\mathbf{S}\mathbf{T}_{M-1}\cdots\mathbf{T}_1\mathbf{T}_0\boldsymbol{\Gamma}\mathbf{A}, \tag{B.14}$$

and the corresponding system matrix that incorporates the transducer impulse responses is found to be

$$\mathbf{H}^{\mathrm{IR}} \equiv \boldsymbol{\Gamma}^{\mathrm{EIR}}\boldsymbol{\Gamma}^{\mathrm{SIR}}\mathbf{S}\mathbf{T}_{M-1}\cdots\mathbf{T}_1\mathbf{T}_0\boldsymbol{\Gamma}. \tag{B.15}$$

Appendix C

Implementation of the FISTA algorithm for PACT

Equation (5.20) was solved iteratively whose pseudocodes are provided in Alg. 2, where 'Lip' is the Lipschitz constant of the operator $2\mathbf{H}^{\mathrm{T}}\mathbf{H}$ [11].

Algorithm 2 Solver of the optimization problem defined by Eqn. (5.20)

```
Input: $\hat{\mathbf{p}}$, $\mathbf{p}_0^{(0)}$, $\lambda$, Lip
Output: $\hat{\mathbf{p}}_0$
1: $t^{(0)} \leftarrow 1$; $\boldsymbol{\sigma}_0^{(1)} \leftarrow \mathbf{p}_0^{(0)}$ {Set the initial guess (The zero initial guess was employed in all the studies in this article)}
2: for $\zeta = 1$ to $Z$ do
3:     $\mathbf{p}_0^{(\zeta)} \leftarrow \mathrm{F\_Dnoise}\big(\boldsymbol{\sigma}_0^{(\zeta)} - \frac{2}{\mathrm{Lip}}\mathbf{H}^{\mathrm{T}}(\mathbf{H}\boldsymbol{\sigma}_0^{(\zeta)} - \hat{\mathbf{p}}), 2\lambda/\mathrm{Lip}\big)$
4:     $t^{(\zeta+1)} \leftarrow 0.5 + 0.5\sqrt{1 + 4(t^{(\zeta)})^2}$
5:     $\boldsymbol{\sigma}_0^{(\zeta+1)} \leftarrow \mathbf{p}_0^{(\zeta)} + (t^{(\zeta)} - 1)(\mathbf{p}_0^{(\zeta)} - \mathbf{p}_0^{(\zeta-1)})/t^{(\zeta+1)}$
6: end for
7: $\hat{\mathbf{p}}_0 \leftarrow \mathbf{p}_0^{(Z)}$
```

Note that we extended the FISTA algorithm described in Ref. [**?**] to 3D. The function 'F_Dnoise' in Alg. 2-Line 3 solves a de-noising problem defined as:

$$\hat{\mathbf{x}} = \arg\min_{\mathbf{x}\geq 0}\|\mathbf{y} - \mathbf{x}\|^2 + \beta|\mathbf{x}|_{\mathrm{TV}}, \tag{C.1}$$

where $\beta = 2\lambda/\text{Lip}$ and

$$\mathbf{y} = \hat{\mathbf{p}} - \frac{2}{\text{Lip}}\mathbf{H}^{\mathrm{T}}(\mathbf{H}\boldsymbol{\sigma}_0^{(\zeta)} - \hat{\mathbf{p}}). \tag{C.2}$$

It has been demonstrated that Eqn. (C.1) can be solved efficiently [?], and the pseudocodes are provided in Alg. 3.

Algorithm 3 Solver of the de-noising problem defined by Eqn. (C.1)

```
Input: $\mathbf{y}$, $\beta$
Output: $\hat{\mathbf{x}}$
$\big[\mathbf{a}^{(1)}, \mathbf{b}^{(1)}, \mathbf{c}^{(1)}\big] \leftarrow$
    $\big[\mathbf{0}_{(N_1-1)\times N_2\times N_3}, \mathbf{0}_{N_1\times(N_2-1)\times N_3}, \mathbf{0}_{N_1\times N_2\times(N_3-1)}\big]$
$\big[\mathbf{d}^{(0)}, \mathbf{e}^{(0)}, \mathbf{f}^{(0)}\big] \leftarrow$
    $\big[\mathbf{0}_{(N_1-1)\times N_2\times N_3}, \mathbf{0}_{N_1\times(N_2-1)\times N_3}, \mathbf{0}_{N_1\times N_2\times(N_3-1)}\big]$
$t^{(1)} = 1$
for $\zeta = 1$ to $Z$ do
    $\big[\mathbf{d}^{(\zeta)}, \mathbf{e}^{(\zeta)}, \mathbf{f}^{(\zeta)}\big] \leftarrow \mathcal{P}_p\Big\{[\mathbf{a}^{(\zeta)}, \mathbf{b}^{(\zeta)}, \mathbf{c}^{(\zeta)}] + (6\beta)^{-1}\mathcal{P}_l^T\big\{\mathcal{P}_c\{\mathbf{y} - 0.5\beta\mathcal{P}_l\{\mathbf{a}^{(\zeta)}, \mathbf{b}^{(\zeta)}, \mathbf{c}^{(\zeta)}\}\}\big\}\Big\}$
    $t^{(\zeta+1)} \leftarrow 1 + 0.5\sqrt{1 + 4(t^{(\zeta)})^2}$
    $\big[\mathbf{a}^{(\zeta+1)}, \mathbf{b}^{(\zeta+1)}, \mathbf{c}^{(\zeta+1)}\big] \leftarrow (t^{(\zeta)} - 1)/t^{(\zeta+1)}\big[\mathbf{d}^{(\zeta)} - \mathbf{d}^{(\zeta-1)}, \mathbf{e}^{(\zeta)} - \mathbf{e}^{(\zeta-1)}, \mathbf{f}^{(\zeta)} - \mathbf{f}^{(\zeta-1)}\big]$
end for
$\hat{\mathbf{x}} \leftarrow \mathcal{P}_c\big\{\mathbf{y} - \lambda\mathcal{P}_l\{\mathbf{d}^{(Z)}, \mathbf{e}^{(Z)}, \mathbf{f}^{(Z)}\}\big\}$
```

The four operators $\mathcal{P}_l$ $\mathcal{P}_c$, $\mathcal{P}_l^T$ and $\mathcal{P}_p$ in Alg. 3 are defined as follows:

$\mathcal{P}_l : \mathbb{R}^{(N_1-1)\times N_2\times N_3} \times \mathbb{R}^{N_1\times(N_2-1)\times N_3} \times \mathbb{R}^{N_1\times N_2\times(N_3-1)} \longrightarrow \mathbb{R}^{N_1\times N_2\times N_3}$.

$$\begin{aligned}
&\big[\mathcal{P}_l\{\mathbf{a}, \mathbf{b}, \mathbf{c}\}\big]_{n_1,n_2,n_3} = \\
&[\mathbf{a}]_{n_1,n_2,n_3} + [\mathbf{b}]_{n_1,n_2,n_3} + [\mathbf{c}]_{n_1,n_2,n_3} - \\
&[\mathbf{a}]_{n_1-1,n_2,n_3} - [\mathbf{b}]_{n_1,n_2-1,n_3} - [\mathbf{c}]_{n_1,n_2,n_3-1} \\
&\text{for} \quad n_1 = 1, \cdots, N_1,\ n_2 = 1, \cdots, N_2,\ n_3 = 1, \cdots, N_3,
\end{aligned} \tag{C.3}$$

where we assume $[\mathbf{a}]_{0,n_2,n_3} = [\mathbf{a}]_{N_1,n_2,n_3} = [\mathbf{b}]_{n_1,0,n_3} = [\mathbf{b}]_{n_1,N_2,n_3} = [\mathbf{c}]_{n_1,n_2,0} = [\mathbf{c}]_{n_1,n_2,N_3} \equiv 0$.

$\mathcal{P}_c : \mathbb{R}^{N_1\times N_2\times N_3} \rightarrow \mathbb{R}^{N_1\times N_2\times N_3}$.

$$\left[\mathcal{P}_c\{\mathbf{x}\}\right]_{n_1,n_2,n_3} = \max\left\{0, [\mathbf{x}]_{n_1,n_2,n_3}.\right\} \tag{C.4}$$

$\mathcal{P}_l^T : \mathbb{R}^{N_1\times N_2\times N_3} \rightarrow \mathbb{R}^{(N_1-1)\times N_2\times N_3} \times \mathbb{R}^{N_1\times(N_2-1)\times N_3} \times \mathbb{R}^{N_1\times N_2\times(N_3-1)}$. If we denote the input and output matrices by $\mathbf{y}$ and $(\mathbf{a},\mathbf{b},\mathbf{c})$ respectively, we have

$$\begin{aligned}
&[\mathbf{a}]_{n_1,n_2,n_3} = [\mathbf{y}]_{n_1,n_2,n_3} - [\mathbf{y}]_{n_1+1,n_2,n_3},\\
&\text{for} \quad n_1 = 1,\cdots,N_1-1, n_2 = 1,\cdots,N_2, n_3 = 1,\cdots,N_3\\
&[\mathbf{b}]_{n_1,n_2,n_3} = [\mathbf{y}]_{n_1,n_2,n_3} - [\mathbf{y}]_{n_1,n_2+1,n_3},\\
&\text{for} \quad n_1 = 1,\cdots,N_1, n_2 = 1,\cdots,N_2-1, n_3 = 1,\cdots,N_3\\
&[\mathbf{c}]_{n_1,n_2,n_3} = [\mathbf{y}]_{n_1,n_2,n_3} - [\mathbf{y}]_{n_1,n_2,n_3+1},\\
&\text{for} \quad n_1 = 1,\cdots,N_1, n_2 = 1,\cdots,N_2, n_3 = 1,\cdots,N_3-1.
\end{aligned} \tag{C.5}$$

$\mathcal{P}_p : \mathbb{R}^{(N_1-1)\times N_2\times N_3} \times \mathbb{R}^{N_1\times(N_2-1)\times N_3} \times \mathbb{R}^{N_1\times N_2\times(N_3-1)} \rightarrow \mathbb{R}^{(N_1-1)\times N_2\times N_3} \times \mathbb{R}^{N_1\times(N_2-1)\times N_3} \times \mathbb{R}^{N_1\times N_2\times(N_3-1)}$. If we denote the input and output matrices by $(\mathbf{a},\mathbf{b},\mathbf{c})$ and $(\mathbf{d},\mathbf{e},\mathbf{f})$ respectively, we have

$$\begin{aligned}
[\mathbf{d}]_{n_1,n_2,n_3} &= \frac{[\mathbf{a}]_{n_1,n_2,n_3}}{\max\left\{1, \sqrt{[\mathbf{a}]^2_{n_1,n_2,n_3} + [\mathbf{b}]^2_{n_1,n_2,n_3} + [\mathbf{c}]^2_{n_1,n_2,n_3}}\right\}}\\
[\mathbf{e}]_{n_1,n_2,n_3} &= \frac{[\mathbf{b}]_{n_1,n_2,n_3}}{\max\left\{1, \sqrt{[\mathbf{a}]^2_{n_1,n_2,n_3} + [\mathbf{b}]^2_{n_1,n_2,n_3} + [\mathbf{c}]^2_{n_1,n_2,n_3}}\right\}}\\
[\mathbf{f}]_{n_1,n_2,n_3} &= \frac{[\mathbf{c}]_{n_1,n_2,n_3}}{\max\left\{1, \sqrt{[\mathbf{a}]^2_{n_1,n_2,n_3} + [\mathbf{b}]^2_{n_1,n_2,n_3} + [\mathbf{c}]^2_{n_1,n_2,n_3}}\right\}},
\end{aligned} \tag{C.6}$$

where $n_1 = 1,\cdots,N_1$, $n_2 = 1,\cdots,N_2$, $n_3 = 1,\cdots,N_3$, and we assume $[\mathbf{a}]_{0,n_2,n_3} = [\mathbf{a}]_{N_1,n_2,n_3} = [\mathbf{b}]_{n_1,0,n_3} = [\mathbf{b}]_{n_1,N_2,n_3} = [\mathbf{c}]_{n_1,n_2,0} = [\mathbf{c}]_{n_1,n_2,N_3} \equiv 0$.

Appendix D

Calculating the Gradient of (6.10)

The gradient of the first term in (6.10) can be calculated by discretizing the the Fréchet derivative (6.7)

$$\begin{aligned}\frac{\partial\|\mathbf{H}(\mathbf{c})\mathbf{A}-\tilde{\mathbf{p}}\|^2}{\partial\mathbf{c}} = -4\mathbf{C}^{-3}\circ\big\{\sum_{l=1}^{L-2}\frac{\mathbf{p}_{l+1}-\mathbf{p}_{l-1}}{2}\circ\frac{\mathbf{q}_{l+1}-\mathbf{q}_{l-1}}{2} \\ +(\mathbf{p}_1-\mathbf{p}_0)\circ(\mathbf{q}_1-\mathbf{q}_0)+(\mathbf{p}_{L-1}-\mathbf{p}_{L-2})\circ(\mathbf{q}_{L-1}-\mathbf{q}_{L-2})\big\}\end{aligned} \tag{D.1}$$

where $\circ$ denotes Hadamard product, $\mathbf{C}^{-3}$ is defined as

$$\mathbf{C}^{-3}\equiv[c(\mathbf{r}_1)^{-3},\cdots,c(\mathbf{r}_N)^{-3}]^{\mathrm{T}}, \tag{D.2}$$

$\mathbf{p}_l$ and $\mathbf{q}_l$ ($l=0,\cdots,L-1$) are defined as

$$\mathbf{p}_l\equiv[p(\mathbf{r}_1,l\Delta t),\cdots,p(\mathbf{r}_N,l\Delta t)]^{\mathrm{T}}, \tag{D.3}$$

and

$$\mathbf{q}_l\equiv[q(\mathbf{r}_1,l\Delta t),\cdots,q(\mathbf{r}_N,l\Delta t)]^{\mathrm{T}}, \tag{D.4}$$

representing the PA wavefield and the adjoint wavefield sampled at the 3D Cartesian grid vertices $\mathbf{r}_n$ ($n=1,\cdots,N$) and at time $t=l\Delta t$, respectively.

If TV-penalty is adopted, the gradient of the second term in (6.10) is given by [125]

$$\frac{\partial\lambda_c|\mathbf{c}|_{\mathrm{TV}}}{\partial\mathbf{c}}=\lambda_c[\dot{\mathbf{c}}_1,\cdots,\dot{\mathbf{c}}_n,\cdots,\dot{\mathbf{c}}_N]^{\mathrm{T}}, \tag{D.5}$$

and

$$\begin{aligned}\dot{\mathbf{c}}_n \equiv & \frac{([\mathbf{c}]_n - [\mathbf{c}]_{n_1^-}) + ([\mathbf{c}]_n - [\mathbf{c}]_{n_2^-}) + ([\mathbf{c}]_n - [\mathbf{c}]_{n_3^-})}{\epsilon + \{([\mathbf{c}]_n - [\mathbf{c}]_{n_1^-})^2 + ([\mathbf{c}]_n - [\mathbf{c}]_{n_2^-})^2 + ([\mathbf{c}]_n - [\mathbf{c}]_{n_3^-})^2\}^{\frac{1}{2}}} \\ & - \frac{[\mathbf{c}]_{n_1^+} - [\mathbf{c}]_n}{\epsilon + \{([\mathbf{c}]_{n_1^+} - [\mathbf{c}]_n)^2 + ([\mathbf{c}]_{n_1^+} - [\mathbf{c}]_{(n_1^+)_2^-})^2 + ([\mathbf{c}]_{n_1^+} - [\mathbf{c}]_{(n_1^+)_3^-})^2\}^{\frac{1}{2}}} \\ & - \frac{[\mathbf{c}]_{n_2^+} - [\mathbf{c}]_n}{\epsilon + \{([\mathbf{c}]_{n_2^+} - [\mathbf{c}]_{(n_2^+)_1^-})^2 + ([\mathbf{c}]_{n_2^+} - [\mathbf{c}]_n)^2 + ([\mathbf{c}]_{n_2^+} - [\mathbf{c}]_{(n_2^+)_3^-})^2\}^{\frac{1}{2}}} \\ & - \frac{[\mathbf{c}]_{n_3^+} - [\mathbf{c}]_n}{\epsilon + \{([\mathbf{c}]_{n_3^+} - [\mathbf{c}]_{(n_3^+)_1^-})^2 + ([\mathbf{c}]_{n_3^+} - [\mathbf{c}]_{(n_3^+)_2^-})^2 + ([\mathbf{c}]_{n_3^+} - [\mathbf{c}]_n)^2\}^{\frac{1}{2}}},\end{aligned} \tag{D.6}$$

where ϵ is a small positive number to prevent the denominators being zeros, and $[\mathbf{c}]_n$ denotes the n-th grid node of $\mathbf{c}$, and $[\mathbf{c}]_{n_i^-}$ and $[\mathbf{c}]_{n_i^+}$ are neighboring nodes before and after the n-th node along the i-th dimension ($i = 1, 2, 3$), respectively. Likewise, $[\mathbf{c}]_{(n_i^+)_j^-}$ denotes the neighboring node that is after the n-th node along the i-th dimension and before the n-th node along the j-th dimension.

The gradient of the objective function in (6.10) is then given by the sum of (D.1) and (D.5).

Appendix E

Support Condition for Accurate Reconstruction of $c(\mathbf{r})$

First, we define the supports of $A(\mathbf{r})$ and $c(\mathbf{r})$ being the regions where $A(\mathbf{r}) \neq 0$ and $c(\mathbf{r}) - c_0 \neq 0$, respectively. Here c_0 is the known SOS in the background (e.g. in water). We then assume both $A(\mathbf{r})$ and $c(\mathbf{r})$ possess compact supports, which is denoted as $\text{supp}(A)$ and $\text{supp}(c)$, respectively. Second, we assume weak variation in a medium's SOS distribution. Specifically, variations in the SOS distribution must occur on length scales that are large compared to the effective acoustic wavelength. Under this assumption, a straight ray model is utilized to approximate the wave equation. Third, we further assume that the PA signal generated at each point of $\text{supp}(A)$ can be recorded independently by transducers, which are densely distributed on a measurement surface that encloses $\text{supp}(A)$ and $\text{supp}(c)$.

Under the above assumptions, the reconstruction of the slowness $s(\mathbf{r}) \equiv \frac{1}{c(\mathbf{r})}$, which is equivalent to reconstructing $c(\mathbf{r})$, is analogous to the reconstruction of attenuation coefficients in X-ray computed tomography (CT). The 2D analogy is shown in Fig. E.1 and described below. First, consider the case where $\text{supp}(c) \subseteq \text{supp}(A)$. Without loss of generality, the measurement surface is assumed to be a circle with radius R that encloses $\text{supp}(A)$.

Consider the projection of $s(\mathbf{r})$ ($\mathbf{r} \in \text{supp}(A)$) in direction α, as shown in Fig. E.1. Since we assume that the PA signal generated at each point of $\text{supp}(A)$ can be independently recorded, we can compute the time of flight (TOF), which is denoted as $t_f(\beta, \mathbf{r})$, of the signal traveling from the point $\mathbf{r} \in \text{supp}(A)$ to the transducer located at $\mathbf{r}_\beta \equiv [R\cos(\beta), R\sin(\beta)]^{\mathrm{T}}$

$(\beta \in [\alpha - \frac{\pi}{2}, \alpha + \frac{\pi}{2}])$. We then define

$$t_0(\alpha, \beta) = \inf\{t_f(\beta, \mathbf{r}) : \mathbf{r} \cdot \hat{\mathbf{n}} = d, \mathbf{r} \in \mathrm{supp}(A)\} \tag{E.1}$$

and

$$t_1(\alpha, \beta) = \sup\{t_f(\beta, \mathbf{r}) : \mathbf{r} \cdot \hat{\mathbf{n}} = d, \mathbf{r} \in \mathrm{supp}(A)\}, \tag{E.2}$$

where $\hat{\mathbf{n}} = [\cos(\alpha - \frac{\pi}{2}), \sin(\alpha - \frac{\pi}{2})]^{\mathrm{T}}$ is the unit vector in direction $\alpha - \frac{\pi}{2}$, and $d = R\sin(\beta - \alpha)$, as shown in Fig. E.1. Geometrically, $t_0(\alpha, \beta)$ (resp. $t_1(\alpha, \beta)$) is the TOF of the signal traveling from point $\mathbf{r}_0$ (resp. point $\mathbf{r}_1$) to $\mathbf{r}_\beta$, where the line segment $\mathbf{r}_0\mathbf{r}_1$ is the intersection of the line $\mathbf{r} \cdot \hat{\mathbf{n}} = d$ and $\mathrm{supp}(A)$. If the line $\mathbf{r} \cdot \hat{\mathbf{n}} = d$ does not intersect with $\mathrm{supp}(A)$, we define $t_0(\alpha, \beta) = t_1(\alpha, \beta) = 0$ $(\beta \in [\alpha - \frac{\pi}{2}, \alpha + \frac{\pi}{2}])$.

Since the straight ray model is assumed, we then have

$$\tau(\alpha, \beta) \equiv t_1(\alpha, \beta) - t_0(\alpha, \beta) = \int_{L(\mathbf{r}_0, \mathbf{r}_1)} s(\mathbf{r})\mathrm{d}\mathbf{r}, \tag{E.3}$$

where the integral is along the line segment $\mathbf{r}_0\mathbf{r}_1$.

Therefore, the set $\tau(\alpha, \beta)$ for a fixed α and all $\beta \in [\alpha - \frac{\pi}{2}, \alpha + \frac{\pi}{2}]$ is the 1D projection of $s(\mathbf{r})$ $(\mathbf{r} \in \mathrm{supp}(A))$ in direction α, and the set $\tau(\alpha, \beta)$ for all α $(\alpha \in [0, 2\pi))$ and $\beta \in [\alpha - \frac{\pi}{2}, \alpha + \frac{\pi}{2}]$ is the 2D Radon transform of $s(\mathbf{r})$ $(\mathbf{r} \in \mathrm{supp}(A))$. Since the Radon transform is invertible, $s(\mathbf{r})$ $(\mathbf{r} \in \mathrm{supp}(A))$ can be accurately reconstructed from $\tau(\alpha, \beta)$, where $\alpha \in [0, 2\pi)$ and $\beta \in [\alpha - \frac{\pi}{2}, \alpha + \frac{\pi}{2}]$. Consequently, $c(\mathbf{r})$ $(\mathbf{r} \in \mathrm{supp}(c))$ can be accurately reconstructed as $\mathrm{supp}(c) \subseteq \mathrm{supp}(A)$ is considered here. It follows that $c(\mathbf{r})$ can be accurately reconstructed because the background SOS is assumed to be known. In fact, the requirement $\mathrm{supp}(c) \subseteq \mathrm{supp}(A)$ can be relaxed to $\mathrm{supp}(c)$ being enclosed by $\mathrm{supp}(A)$, as shown in Fig. E.2(a). This is because we only need the $t_f(\beta, \mathbf{r})$ $(\mathbf{r} \in \partial\,\mathrm{supp}(A))$, where $\partial\,\mathrm{supp}(A)$ is the boundary of $\mathrm{supp}(A)$, to compute $\tau(\alpha, \beta)$ according to (E.3).

Consider the case where $\mathrm{supp}(c)$ is not enclosed by $\mathrm{supp}(A)$, as shown in Fig. E.2(b). We can see that, for each projection angle α, the projections of a subset of $\mathrm{supp}(c)$ in this direction (indicated by C_α) are not measured because $A(\mathbf{r}) = 0$ in that subset. This is analogous to the interior problem in X-ray CT, which does not have a unique solution [89]. Therefore, $c(\mathbf{r})$ cannot be accurately reconstructed if $\mathrm{supp}(c)$ is not enclosed by $\mathrm{supp}(A)$.

Finally, the support condition for accurate reconstruction of $c(\mathbf{r})$ is $\mathrm{supp}(c)$ being enclosed by $\mathrm{supp}(A)$.

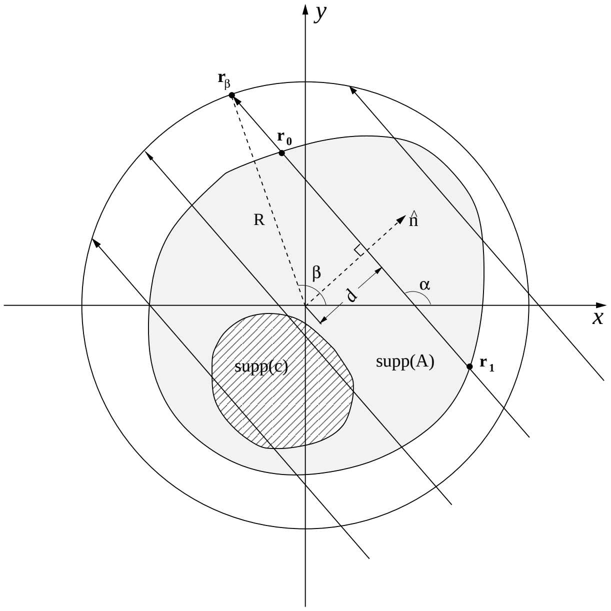

Figure E.1: Projection of the slowness in direction α and supp$(c) \subseteq$ supp(A). As an example, supp(A) can be seen as the area occupied by a breast, where the SOS is approximately the same as the background SOS in water, and supp(c) can be seen as the area occupied by a tumor, where the SOS is larger than the background SOS.

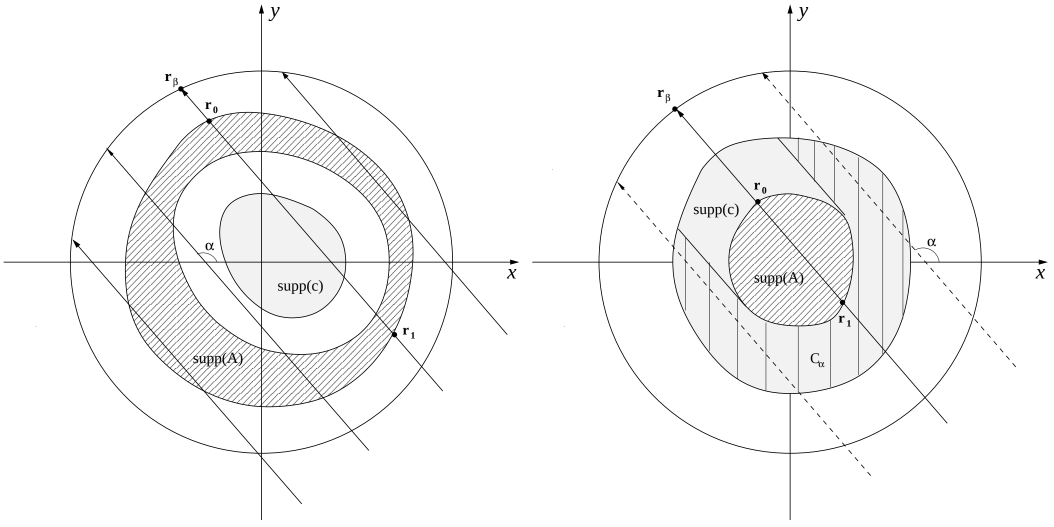

(a) (b)

Figure E.2: Projection of the slowness in direction α. Panel (a): supp(c) is enclosed by supp(A). Panel (b): supp(c) is not enclosed by supp(A), where the projections of the slowness in a subset of supp(c), covered by vertical lines and denoted as C_α, are not measured by transducers.

References

[1] M. Agranovsky and E. T. Quinto. Injectivity sets for the radon transform over circles and complete systems of radial functions.

[2] M. Agranovsky and E. T Quinto. Injectivity sts for the Radon transform over circles and complete systems of radial functions. *Journal of Functional Analysis*, 139:383–414, 1996.

[3] I. Akiyama, N. Takizawa, and A. Ohya. Narrow aperture phased array computed tomography. *Acoustical Imaging*, 25:163–170, 2000.

[4] I. Akiyama and K. Yano. Synthetic aperture computed tomography acoustical imaging. *Acoustical Imaging*, 23:575–581, 1997.

[5] Azzdine Y. Ammi, T. Douglas Mast, I.-Hua Huang, Todd A. Abruzzo, Constantin-C. Coussios, George J. Shaw, and Christy K. Holland. Characterization of ultrasound propagation through ex-vivo human temporal bone. *Ultrasound in Medicine and Biology*, 34(10):1578 – 1589, 2008.

[6] M. Anastasio, Y. Zou, and X. Pan. Reflectivity tomography using temporally truncated data. In *IEEE EMBS/BMES Conference Proceedings*, volume 2, pages 921–922. IEEE, 2002.

[7] M.A Anastasio, J. Zhang, X. Pan, Y Zou, G. Keng, and L.V Wang. Half-time image reconstruction in thermoacoustic tomography. *IEEE Transactions on Medical Imaging*, 24:199–210, 2005.

[8] Valeri G. Andreev, Alexander A. Karabutov, Anatoliy E. Ponomaryov, and Alexander A. Oraevsky. Detection of optoacoustic transients with a rectangular transducer of finite dimensions. In Alexander A. Oraevsky, editor, *Biomedical Optoacoustics III*, volume 4618, pages 153–162. SPIE, 2002.

[9] J.-F. Aubry, M. Tanter, M. Pernot, J.-L. Thomas, and M. Fink. Experimental demonstration of noninvasive transskull adaptive focusing based on prior computed tomography scans. *The Journal of the Acoustical Society of America*, 113(1):84–93, 2003.

[10] H. Barrett, D. Wilson, and B. Tsui. Noise properties of the EM algorithm I. theory. *Physics in Medicine and Biology*, 39:833–846, 1994.

[11] A. Beck and M. Teboulle. Fast gradient-based algorithms for constrained total variation image denoising and deblurring problems. *Image Processing, IEEE Transactions on*, 18(11):2419 –2434, nov. 2009.

[12] M. Bertero and P. Boccacci. *Inverse Problems in Imaging.* Institute of Physics Publishing, Bristol and Philadelphia, 1998.

[13] Hans-Peter Brecht, Richard Su, Matt Fronheiser, Sergey A. Ermilov, Andre Conjusteau, Anton Liopo, Massoud Motamedi, and Alexander A. Oraevsky. Optoacoustic 3d whole-body tomography: experiments in nude mice. volume 7177, page 71770E. SPIE, 2009.

[14] Hans-Peter Brecht, Richard Su, Matthew Fronheiser, Sergey A. Ermilov, Andre Conjusteau, and Alexander A. Oraevsky. Whole-body three-dimensional optoacoustic tomography system for small animals. *Journal of Biomedical Optics*, 14(6):064007, 2009.

[15] C. Bunks, F. Saleck, S. Zaleski, and G. Chavent. Multiscale seismic waveform inversion. *Geophysics*, 60(5):1457–1473, 1995.

[16] Peter Burgholzer, Hubert Grn, Markus Haltmeier, Robert Nuster, and Gnther Paltauf. Compensation of acoustic attenuation for high-resolution photoacoustic imaging with line detectors. *Proceedings of the SPIE*, 6437(1):643724, 2007.

[17] Dennis R. Cater and Wilson C. Hayes. The compressive behaviour of bone as a two phase porous material. *The Journal of Bone and Joint Surgery*, 59A:954–962, 1977.

[18] Guoping Chen, Xin Wang, Jinguo Wang, Zhiqin Zhao, Zaiping Nie, and Qinghuo Liu. Tr adjoint imaging method for mitat. *Progress In Electromagnetics Research B*, 46:41–57, 2013.

[19] W. Cheong, S. Prahl, and A. Welch. A review of the optical properties of biological tissues. *IEEE J. Quantum Elect.*, 26:2166–2185, 1990.

[20] P. Cho, R. Johnson, and T. Griffin. Cone-beam CT for radiotherapy applications. *Physics in Medicine and Biology*, 40:1863–1883, 1995.

[21] J. F. Claerbout. Earth Sounding Analysis: Processing Versus Inversion. 1992.

[22] G T Clement and K Hynynen. A non-invasive method for focusing ultrasound through the human skull. *Physics in Medicine and Biology*, 47(8):1219, 2002.

[23] Andr Conjusteau, Sergey A. Ermilov, Richard Su, Hans-Peter Brecht, Matthew P. Fronheiser, and Alexander A. Oraevsky. Measurement of the spectral directivity of optoacoustic and ultrasonic transducers with a laser ultrasonic source. *Review of Scientific Instruments*, 80(9):–, 2009.

[24] B. T. Cox, S. Kara, S. R. Arridge, and P. C. Beard. k-space propagation models for acoustically heterogeneous media: Application to biomedical photoacoustics. *The Journal of the Acoustical Society of America*, 121(6):3453–3464, 2007.

[25] Benjamin T. Cox, Simon R. Arridge, Kornel P. Köstli, and Paul C. Beard. Two-dimensional quantitative photoacoustic image reconstruction of absorption distributions in scattering media by use of a simple iterative method. *Appl. Opt.*, 45(8):1866–1875, Mar 2006.

[26] Charles J. Daly and N. A. H. K. Rao. Time- and frequency-domain descriptions of spatially averaged one-way diffraction for an unfocused piston transducer. *Ultrasonics*, 37(3):209 – 221, 1999.

[27] C. J. Dasch. One-dimensional tomography: a comparison of abel, onion-peeling and filtered backprojection methods. *Applied Optics*, 31:1146–1152, 1992.

[28] X. Luís Deán-Ben, Vasilis Ntziachristos, and Daniel Razansky. Statistical optoacoustic image reconstruction using a-priori knowledge on the location of acoustic distortions. *Applied Physics Letters*, 98(17):171110, 2011.

[29] X Lus Den-Ben, Daniel Razansky, and Vasilis Ntziachristos. The effects of acoustic attenuation in optoacoustic signals. *Physics in Medicine and Biology*, 56(18):6129, 2011.

[30] K. Dines and A. Goss. Computer ultrasonic reflection tomography. *IEEE Transactions on Ultrasonics, Ferroelectrics and Frequency Control*, 34:309–317, 1987.

[31] Daniel M. Dunlavy, Tamara G. Kolda, and Evrim Acar. Poblano v1.0: A matlab toolbox for gradient-based optimization. Technical Report SAND2010-1422, Sandia National Laboratories, Albuquerque, NM and Livermore, CA, March 2010.

[32] Pinhas Ephrat, Lynn Keenliside, Adam Seabrook, Frank S. Prato, and Jeffrey J. L. Carson. Three-dimensional photoacoustic imaging by sparse-array detection and iterative image reconstruction. *Journal of Biomedical Optics*, 13(5):054052, 2008.

[33] Sergey A. Ermilov, Matthew P. Fronheiser, Hans-Peter Brecht, Richard Su, Andre Conjusteau, Ketan Mehta, Pamela Otto, and Alexander A. Oraevsky. Development of laser optoacoustic and ultrasonic imaging system for breast cancer utilizing handheld array probes. volume 7177, page 717703. SPIE, 2009.

[34] Sergey A. Ermilov, Matthew P. Fronheiser, Hans-Peter Brecht, Richard Su, André Conjusteau, Ketan Mehta, Pamela Otto, and Alexander A. Oraevsky. Development of laser optoacoustic and ultrasonic imaging system for breast cancer utilizing handheld array probes. volume 7177, page 717703. SPIE, 2009.

[35] J A Fessler. Penalized weighted least-squares reconstruction for positron emission tomography. *IEEE Transactions on Medical Imaging*, 13:290–300, 1994.

[36] D. Finch, S. Patch, and Rakesh. Determining a function from its mean values over a family of spheres. *SIAM Journal of Mathematical Analysis*, 35:1213–1240, 2004.

[37] F. J. Fry and J. E. Barger. Acoustical properties of the human skull. *The Journal of the Acoustical Society of America*, 63(5):1576–1590, 1978.

[38] G.H. Golub and V. Pereyra. The differentiation of pseudoinverses and nonlinear least squares problems whose variables separate. *SIAM Journal of Numerical Analysis*, 10:413432, 1973.

[39] Jochen Gorski, Frank Pfeuffer, and Kathrin Klamroth. Biconvex sets and optimization with biconvex functions: a survey and extensions. *Mathematical Methods of Operations Research*, 66(3):373–407, 2007.

[40] V. Guillemin and S. Sternberg. Some problems in integral geometry and some related problems in micro-local analysis. *American Journal of Mathematics*, 101:915–955, 1979.

[41] Zijian Guo, Changhui Li, Liang Song, and Lihong V. Wang. Compressed sensing in photoacoustic tomography in vivo. *Journal of Biomedical Optics*, 15(2):021311, 2010.

[42] V. E. Gusev and A. A. Karabutov. Laser optoacoustic. In *Laser Optoacoustic*. AIP, 1993.

[43] M. Haltmeier, O. Scherzer, P. Burgholzer, R. Nuster, and G. Paltauf. Thermoacoustic tomography and the circular radon transform: exact inversion formula. *Mathematical Models and Methods in Applied Sciences*, 17:635–655, 2007.

[44] M Haltmeier, O Scherzer, P Burgholzer, and G Paltauf. Thermoacoustic computed tomography with large planar receivers. *Inverse Problems*, 20(5):1663–1673, 2004.

[45] Gerald R. Harris. Review of transient field theory for a baffled planar piston. *The Journal of the Acoustical Society of America*, 70(1):10–20, 1981.

[46] Mark Hayner and Kullervo Hynynen. Numerical analysis of ultrasonic transmission and absorption of oblique plane waves through the human skull. 110(6):3319–3330, 2001.

[47] P He. Determination of ultrasonic parameters based on attenuation and dispersion measurements. *Ultrasonic Imaging*, 20(4):275–287, 1998.

[48] Kyle Scott Hickmann. *Unique Determination of Acoustic Properties from Thermoacoustic Data.* PhD thesis, Oregon State University, 2010.

[49] J. Hong, J. A. Hipp, R. V. Mulkern, D. Jaramillo, and B. D. Snyder. Magnetic resonance imaging measurements of bone density and cross-sectional geometry. *Calcified Tissue International*, 66(1):74–78, 2000.

[50] Yulia Hristova, Peter Kuchment, and Linh Nguyen. Reconstruction and time reversal in thermoacoustic tomography in acoustically homogeneous and inhomogeneous media. *Inverse Problems*, 24(5):055006, 2008.

[51] C. Huang, K. Wang, L. Nie, L.V. Wang, and M.A. Anastasio. Full-wave iterative image reconstruction in photoacoustic tomography with acoustically inhomogeneous media. *Medical Imaging, IEEE Transactions on*, 32(6):1097–1110, 2013.

[52] Chao Huang, Liming Nie, Robert W. Schoonover, Zijian Guo, Carsten O. Schirra, Mark A. Anastasio, and Lihong V. Wang. Aberration correction for transcranial photoacoustic tomography of primates employing adjunct image data. *Journal of Biomedical Optics*, 17(6):066016, 2012.

[53] Chao Huang, Liming Nie, Robert W. Schoonover, Lihong V. Wang, and Mark A. Anastasio. Photoacoustic computed tomography correcting for heterogeneity and attenuation. *Journal of Biomedical Optics*, 17(6):061211, 2012.

[54] Chao Huang, Alexander A. Oraevsky, and Mark A. Anastasio. Investigation of limited-view image reconstruction in optoacoustic tomography employing a priori structural information. In Philip J. Bones, Michael A. Fiddy, and Rick P. Millane, editors, *Image Reconstruction from Incomplete Data VI*, volume 7800, page 780004. SPIE, 2010.

[55] H. Hudson and R. Larkin. Accelerated image reconstruction using ordered subsets of projection data. *IEEE Transactions on Medical Imaging*, 13:601 –609, 1994.

[56] J.A. Jensen and N.B. Svendsen. Calculation of pressure fields from arbitrarily shaped, apodized, and excited ultrasound transducers. *Ultrasonics, Ferroelectrics and Frequency Control, IEEE Transactions on*, 39(2):262 –267, mar 1992.

[57] Jun Ji. An exact adjoint operation pair in time extrapolation and its application in least-squares reverse-time migration. *Geophysics*, 74(5):H27–H33, 2009.

[58] Huabei Jiang, Zhen Yuan, and Xuejun Gu. Spatially varying optical and acoustic property reconstruction using finite-element-based photoacoustic tomography. *J. Opt. Soc. Am. A*, 23(4):878–888, Apr 2006.

[59] Xing Jin, Changhui Li, and Lihong V. Wang. Effects of acoustic heterogeneities on transcranial brain imaging with microwave-induced thermoacoustic tomography. *Medical Physics*, 35(7):3205–3214, 2008.

[60] Xing Jin and Lihong V Wang. Thermoacoustic tomography with correction for acoustic speed variations. *Physics in Medicine and Biology*, 51(24):6437, 2006.

[61] W. Joines, R. Jirtle, M. Rafal, and D. Schaeffer. Microwave power absorption differences between normal and malignant tissue. *Radiation Oncology, Biology, Physics*, 6:681–687, 1980.

[62] J. Jose, R. G. H. Willemink, W. Steenbergen, T. G. Van Leeuwen, and S. Manohar. Speed-of-sound compensated photoacoustic tomography for high resolution imaging. 2012.

[63] Jithin Jose, Rene G. H. Willemink, Steffen Resink, Daniele Piras, J. C. G van Hespen, Cornelis H. Slump, Wiendelt Steenbergen, Ton G. van Leeuwen, and Srirang Manohar. Passive element enriched photoacoustic computed tomography (per pact) for simultaneous imaging of acoustic propagation properties and light absorption. *Optics Express*, 19(3):2093–2104, Jan 2011.

[64] Jithin Jose, Rene G. H. Willemink, Wiendelt Steenbergen, C. H. Slump, Ton G. van Leeuwen, and Srirang Manohar. Speed-of-sound compensated photoacoustic tomography for accurate imaging. *Medical Physics*, 39(12):7262–7271, 2012.

[65] J. E. Dennis Jr. and R. B. Schnabel. Numerical methods for unconstrained optimization and nonlinear equations. In *Numerical Methods for Unconstrained Optimization and Nonlinear Equations*. Society for Industrial and Applied Mathematics, 1996.

[66] Jari Kaipio and Erkki Somersalo. Statistical inverse problems: discretization, model reduction and inverse crimes. *J. Comput. Appl. Math.*, 198(2):493–504, January 2007.

[67] T.K. Katsibas and C.S. Antonopoulos. A general form of perfectly matched layers for for three-dimensional problems of acoustic scattering in lossless and lossy fluid media. *Ultrasonics, Ferroelectrics and Frequency Control, IEEE Transactions on*, 51(8):964 –972, aug. 2004.

[68] Lawrence E. Kinsler, Austin R. Frey, Alan B. Coppens, and James V. Sanders. Fundamentals of acoustics. In *Fundamentals of Acoustics*. Wiley, 1999.

[69] R. Kruger, P. Liu, R. Fang, and C. Appledorn. Photoacoustic ultrasound (PAUS) reconstruction tomography. *Medical Physics*, 22:1605–1609, 1995.

[70] R. Kruger, D. Reinecke, and G. Kruger. Thermoacoustic computed tomography- technical considerations. *Medical Physics*, 26:1832–1837, 1999.

[71] G. Ku, X. Wang, G. Stoica, and L.V Wang. Multiple-bandwidth photoacoustic tomography. *Physics in Medicine and Biology*, 49:1329–1338, 2004.

[72] Peter Kuchment and Leonid Kunyansky. Mathematics of thermoacoustic tomography. *European Journal of Applied Mathematics*, 19:191–224, 3 2008.

[73] L A Kunyansky. Explicit inversion formulae for the spherical mean radon transform. *Inverse Problems*, 23:373–383, 2007.

[74] R Lakes, H S Yoon, and J L Katz. Ultrasonic wave propagation and attenuation in wet bone. *Journal of Biomedical Engineering*, 8(2):143–148, 1986.

[75] C. Lan and W. Xiong. An iterative method of ultrasonic reflection mode tomography. *IEEE Transactions on Medical Imaging*, 13:2:419–425, 1994.

[76] D. T. Lee and B. J. Schachter. Two algorithms for constructing a delaunay triangulation. *International Journal of Parallel Programming*, 9:219–242, 1980. 10.1007/BF00977785.

[77] Changhui Li and Lihong V. Wang. High-numerical-aperture-based virtual point detectors for photoacoustic tomography. *Applied Physics Letters*, 93(3):033902, 2008.

[78] Meng-Lin Li, Hao F. Zhang, Konstantin Maslov, George Stoica, and Lihong V. Wang. Improved in vivo photoacoustic microscopy based on a virtual-detector concept. *Opt. Lett.*, 31(4):474–476, 2006.

[79] M.-L Li. Model-based reconstruction of photoacoustic tomography with finite aperture detectors. In *Ultrasonics Symposium, 2009 IEEE*, Sept. 2009 in press.

[80] A. K Louis and E. T Quinto. Local tomographic methods in sonar. In *Surveys on Solution Methods for Inverse Problems*. Springer-Verlag, To appear (2003).

[81] T. Mast. Wideband quantitative ultrasonic imaging by time-domain diffraction tomography. *Journal of the Acoustical Society of America*, 106:3061–3071, 1999.

[82] T.D. Mast, L.P. Souriau, D.-L.D. Liu, M. Tabei, A.I. Nachman, and R.C. Waag. A k-space method for large-scale models of wave propagation in tissue. *Ultrasonics, Ferroelectrics and Frequency Control, IEEE Transactions on*, 48(2):341 –354, march 2001.

[83] A. A. Oraevsky and A. A. Karabutov. Optoacoustic tomography. In Tuan Vo-Dinh, editor, *Biomedical Photonics Handbook*. CRC Press LLC, 2003.

[84] Wernick M. N. and J. N. Aarsvold. *Emission Tomography, the Fundamentals of PET and SPECT*. Elsevier Academic Press, San Diego, California, 2004.

[85] Dimple Modgil, Mark A. Anastasio, and Patrick J. La Rivire. Image reconstruction in photoacoustic tomography with variable speed of sound using a higher-order geometrical acoustics approximation. *Journal of Biomedical Optics*, 15(2):021308–021308–9, 2010.

[86] Dimple Modgil, Mark A. Anastasio, and Patrick J. La Riviere. Photoacoustic image reconstruction in an attenuating medium using singular value decomposition. *Proceedings of the SPIE*, 7177(1):71771B, 2009.

[87] Philip M. Morse. Theoretical acoustics. In *Theoretical Acoustics*. Princeton University Press, 1987.

[88] M. Moshfeghhi. Ultrasound reflection-mode tomography using fan-shaped-beam insonification. *IEEE Transactions on Ultrasonics, Ferroelectrics and Frequency Control*, 33:299–314, 1986.

[89] Frank Natterer. The mathematics of computerized tomography. In *The Mathematics of Computerized Tomography*. Society for Industrial and Applied Mathematics, 2001.

[90] Liming Nie, Zijian Guo, and Lihong V. Wang. Photoacoustic tomography of monkey brain using virtual point ultrasonic transducers. 16(7):076005, 2011.

[91] J. Nocedal and S. J. Wright. Numerical optimization. In *Numerical Optimization*. Springer, 1999.

[92] F. Noo and J. Wagner. Image reconstruction in 2d spect with 180° acquisition. *Inverse Problems*, 17:1357–1371, 2001.

[93] Stephen Norton. Reconstruction of a two-dimensional reflecting medium over a circular domain: Exact solution. *Journal of the Acoustical Society of America*, 67(4):1266–1273, 1980.

[94] Stephen Norton and Melvin Linzer. Ultrasonic reflectivity imaging in three dimensions: Reconstruction with spherical transducer arrays. *Ultrasonic Imaging*, 1:210–231, 1979.

[95] Stephen Norton and Melvin Linzer. Ultrasonic reflectivity imaging in three dimensions: Exact inverse scattering solutions for plane, cylindrical, and spherical apertures. *IEEE Transactions on Biomedical Engineering*, 28:202–220, 1981.

[96] Stephen J. Norton. Iterative inverse scattering algorithms: Methods of computing frchet derivatives. *The Journal of the Acoustical Society of America*, 106(5):2653–2660, 1999.

[97] G. Paltauf, J. Viator, S. Prahl, and S. Jacques. Iterative reconstruction algorithm for optoacoustic imaging. *Journal of the Acoustical Society of America*, 112:1536–1544, 2002.

[98] G. Paltauf, J. A. Viator, S. A. Prahl, and S. L. Jacques. Iterative reconstruction algorithm for optoacoustic imaging. *The Journal of the Acoustical Society of America*, 112(4):1536–1544, 2002.

[99] X. Pan and M. Anastasio. Minimal-scan filtered backpropagation algorithms for diffraction tomography. *Journal of the Optical Society of America A*, 16:2896–2903, 1999.

[100] X. Pan, C. M Kao, and C. E Metz. A family of -scheme exponential Radon transforms and the uniqueness of their inverses. *Inverse Problems*, 18:825–836, 2002.

[101] X. Pan and C. E Metz. Analysis of noise properties of a class of exact methods of inverting the 2D exponential Radon transform. *IEEE Transactions on Medical Imaging*, 14:659–668, 1995.

[102] X. Pan, E. Y. Sidky, C.-M. Kao, Y. Zou, and C. E. Metz. Image reconstruction in spect with non-uniform attenuation and 3d distance-dependent spatial resolution. *Phys. Med. Biol.*, 47:2811–2833, 2002.

[103] X. Pan, E. Y. Sidky, C-M Kao, Y. Zou, and C. E Metz. Image reconstruction in π-scheme spect with non-uniform attenuation. *IEEE Transactions on Nuclear Science, (accepted)*, 2003.

[104] X. Pan, Y. Zou, M. Anastasio, and E. Sidky. Data symmetries and reduced-scan image reconstruction in 3D reflectivity tomography. *Physics in Medicine and Biology (submitted)*, 2004.

[105] X. Pan, Y. Zou, and M. A Anastasio. Data redundany and reduced-scan reconstruction in reflectivity tomography. *IEEE Transactions on Image Processing*, 12:784–795, 2003.

[106] D. Parker. Optimal short scan convolution reconstruction for fanbeam CT. *Medical Physics*, 9:254–257, 1982.

[107] M. Pernot, J-F Aubry, M. Tanter, Jean-Louis Thomas, and M. Fink. Experimental validation of 3d finite differences simulations of ultrasonic wave propagation through the skull. In *Ultrasonics Symposium, 2001 IEEE*, volume 2, pages 1547–1550 vol.2, 2001.

[108] Samuel Pichardo, Vivian W Sin, and Kullervo Hynynen. Multi-frequency characterization of the speed of sound and attenuation coefficient for longitudinal transmission of freshly excised human skulls. *Physics in Medicine and Biology*, 56(1):219, 2011.

[109] B. Piwakowski and K. Sbai. A new approach to calculate the field radiated from arbitrarily structured transducer arrays. *Ultrasonics, Ferroelectrics and Frequency Control, IEEE Transactions on*, 46(2):422–440, Mar 1999.

[110] B. Piwakowski and K. Sbai. A new approach to calculate the field radiated from arbitrarily structured transducer arrays. *Ultrasonics, Ferroelectrics and Frequency Control, IEEE Transactions on*, 46(2):422 –440, mar 1999.

[111] J. Provost and F. Lesage. The application of compressed sensing for photo-acoustic tomography. *Medical Imaging, IEEE Transactions on*, 28(4):585 –594, 2009.

[112] J. Qi. A unified noise analysis for iterative image estimation. *Physics in Medicine and Biology*, 48:3505–3519, 2003.

[113] Jianliang Qian, Plamen Stefanov, Gunther Uhlmann, and Hongkai Zhao. An efficient neumann series-based algorithm for thermoacoustic and photoacoustic tomography with variable sound speed. *SIAM J. Img. Sci.*, 4(3):850–883, September 2011.

[114] E. T Quinto. Singularities of the x-ray transform and limited data tomography in $\mathbf{R}^2$ and $\mathbf{R}^3$. *SIAM Journal on Mathematical Analysis*, 24:1215–1225, 1993.

[115] E. T Quinto. Radon transforms, differential equations, and microlocal analysis. In E. T. Quinto, L. Ehrenpreis, A. Faridani, F. Gonzalez, and E. Grinberg, editors, *Radon Transforms and Tomography*, Contemporary Mathematics. American Mathematical Society, 2001.

[116] E. T Quinto, 2002. Department of Mathematics, Tufts University, Personal Communication.

[117] A. Raam and A. Katsevich. *The Radon transform and local tomography.* CRC Press, Inc., Boca Raton, FL, 1996.

[118] Patrick J. La Rivière, Jin Zhang, and Mark A. Anastasio. Image reconstruction in optoacoustic tomography for dispersive acoustic media. *Opt. Lett.*, 31(6):781–783, Mar 2006.

[119] P. La Riviere, X. Pan, D. Gilland, C. M. Kao, W. Chang, and R. Jaszczak. Transmission image reconstruction and redundant information in SPECT with asymmetric fanbeam collimation. *IEEE Transactions on Nuclear Science*, 48:1357–1363, 2001.

[120] Antoine Rosset, Luca Spadola, and Osman Ratib. Osirix: An open-source software for navigating in multidimensional dicom images. *J. Digital Imaging*, 17(3):205–216, 2004.

[121] J P Schlomka, E Roessl, R Dorscheid, S Dill, G Martens, T Istel, C Bumer, C Herrmann, R Steadman, G Zeitler, A Livne, and R Proksa. Experimental feasibility of multi-energy photon-counting k-edge imaging in pre-clinical computed tomography. *Physics in Medicine and Biology*, 53(15):4031, 2008.

[122] Robert W. Schoonover, Lihong V. Wang, and Mark A. Anastasio. Numerical investigation of the effects of shear waves in transcranial photoacoustic tomography with a planar geometry. *Journal of Biomedical Optics*, 17(6), 2012.

[123] T. Schwierz-Iosefzon, A. Notea, and M. Deutsch. Radiography of nonaxisymmetric objects: An onion-peeling inversion method. *Appl. Phys. Lett.*, 81:2121–2123, 2002.

[124] L. A. Shepp and Y. Vardi. Maximum likelihood reconstruction for emission tomography. *IEEE Transactions on Medical Imaging*, 1:113–122, 1982.

[125] E. Sidky, C. Kao, and X. Pan. Accurate image reconstruction from few-views and limited-angle data in divergent-beam ct. 2009.

[126] E. Y. Sidky and X. Pan. Variable sinograms and redundant information in spect with non-uniform attenuation. *Inverse Problems*, 18:1483–1497, 2002.

[127] E. Y. Sidky and X. Pan. Image reconstruction with a half-detector in single-photon emission computed tomography with non-uniform attenuation. *Optical Engineering*, 42:2506–2513, 2003.

[128] Emil Y Sidky, Chien-Min Kao, and Xiaochuan Pan. Accurate image reconstruction from few-views and limited-angle data in divergent-beam ct. *Journal of X-Ray Science and Technology*, 14(2):119, 2006.

[129] Emil Y Sidky and Xiaochuan Pan. Image reconstruction in circular cone-beam computed tomography by constrained, total-variation minimization. *Physics in Medicine and Biology*, 53(17):4777, 2008.

[130] Emil Y. Sidky, Xiaochuan Pan, Ingrid S. Reiser, Robert M. Nishikawa, Richard H. Moore, and Daniel B. Kopans. Enhanced imaging of microcalcifications in digital breast tomosynthesis through improved image-reconstruction algorithms. *Medical Physics*, 36(11):4920–4932, 2009.

[131] E. Somersalo, M. Cheney, D. Isaacson, and E. Isaacson. Layer stripping: a direct numerical method for impedence imaging. *Inverse Problems*, 7:899–926, 1991.

[132] J-L Starck, E.J. Candes, and D.L. Donoho. The curvelet transform for image denoising. *Image Processing, IEEE Transactions on*, 11(6):670–684, Jun 2002.

[133] Plamen Stefanov and Gunther Uhlmann. Thermoacoustic tomography with variable sound speed. *Inverse Problems*, 25(7):075011, 2009.

[134] Plamen Stefanov and Gunther Uhlmann. Recovery of a source term or a speed with one measurement and applications. 2011.

[135] Plamen Stefanov and Gunther Uhlmann. Instability of the linearized problem in multiwave tomography of recovery both the source and the speed. 2012.

[136] Peter R. Stepanishen. Transient radiation from pistons in an infinite planar baffle. *The Journal of the Acoustical Society of America*, 49(5B):1629–1638, 1971.

[137] Jie Sun and Kullervo Hynynen. Focusing of therapeutic ultrasound through a human skull: A numerical study. *The Journal of the Acoustical Society of America*, 104(3), 1998.

[138] Thomas L. Szabo. Time domain wave equations for lossy media obeying a frequency power law. *The Journal of the Acoustical Society of America*, 96(1):491–500, 1994.

[139] Thomas L. Szabo. Diagnostic ultrasound imaging. In *Diagnostic Ultrasound Imaging: Inside Out*. Elsevier, 2004.

[140] Makoto Tabei, T. Douglas Mast, and Robert C. Waag. A k-space method for coupled first-order acoustic propagation equations. *The Journal of the Acoustical Society of America*, 111(1):53–63, 2002.

[141] N. Takizawa, A. Ohya, and I. Akiyama. Ultrasonic tomography using arc focusing beam. In *IEEE Ultrasonics Symposium Proceedings*, pages 1659–1662. IEEE, 1998.

[142] Jean-Louis Thomas and M.A. Fink. Ultrasonic beam focusing through tissue inhomogeneities with a time reversal mirror: application to transskull therapy. *Ultrasonics, Ferroelectrics and Frequency Control, IEEE Transactions on*, 43(6):1122–1129, Nov 1996.

[143] B.E. Treeby and B.T. Cox. k-wave: MATLAB toolbox for the simulation and reconstruction of photoacoustic wave fields. *Journal of Biomedical Optics*, 15:021314, 2010.

[144] Bradley E Treeby, Edward Z Zhang, and B T Cox. Photoacoustic tomography in absorbing acoustic media using time reversal. *Inverse Problems*, 26(11):115003, 2010.

[145] Y. Vardi and D. Lee. From image deblurring to optimal investments: Maximum likelihood solutions for positive linear inverse problems. *Journal of the Royal Statistical Society B*, 55:569–612, 1993.

[146] K. Wang and M. A. Anastasio. Photoacoustic and thermoacoustic tomography: image formation principles. In Otmar Scherzer, editor, *Handbook of Mathematical Methods in Imaging*. Springer, 2011.

[147] K. Wang, S. A. Ermilov, R. Su, H.-P. Brecht, A. A. Oraevsky, and M. A. Anastasio. An imaging model incorporating ultrasonic transducer properties for three-dimensional optoacoustic tomography. *Medical Imaging, IEEE Transactions on*, 30(2):203 –214, 2011.

[148] Kun Wang and Mark A Anastasio. A simple fourier transform-based reconstruction formula for photoacoustic computed tomography with a circular or spherical measurement geometry. *Physics in Medicine and Biology*, 57(23):N493, 2012.

[149] Kun Wang, S.A. Ermilov, R. Su, H.-P. Brecht, A.A. Oraevsky, and M.A. Anastasio. An imaging model incorporating ultrasonic transducer properties for three-dimensional optoacoustic tomography. *Medical Imaging, IEEE Transactions on*, 30(2):203 –214, feb. 2011.

[150] Kun Wang, Richard Su, Alexander A Oraevsky, and Mark A Anastasio. Investigation of iterative image reconstruction in three-dimensional optoacoustic tomography. *Physics in Medicine and Biology*, 57(17):5399, 2012.

[151] Kun Wang, Richard Su, Alexander A. Oraevsky, and Mark A. Anastasio. Sparsity regularized data-space restoration in optoacoustic tomography, 2012.

[152] L. V Wang. Tutorial on photoacoustic microscopy and computed tomography. *IEEE Journal of Selected Topics in Quantum Electronics*, 14:171–179, 2008.

[153] L. V Wang and H-I Wu. *Biomedical Optics, Principles and Imaging.* Wiley, Hoboken, N.J., 2007.

[154] Lihong V. Wang. Prospects of photoacoustic tomography. 35(12):5758–5767, 2008.

[155] Lihong V. Wang. Photoacoustic imaging and spectroscopy. In *Photoacoustic Imaging and Spectroscopy.* CRC, 2009.

[156] Xueding Wang, Yongjiang Pang, Geng Ku, Xueyi Xie, George Stoica, and Lihong V. Wang. Noninvasive laser-induced photoacoustic tomography for structural and functional in vivo imaging of the brain. *Nature Biotechnology*, 21:803–806, 2003.

[157] V. H. Weston and B. L. G. Jonsson. Wave front layer stripping approach to inverse scattering for the wave equation. *J. Math. Phys.*, 43:5045–5059, 2002.

[158] W. H. Wong. On vardi's algorithm for positive integral equations. *Technical Report, Department of Statistics, The University of Chicago*, 1991.

[159] Ping Wu and Tadeusz Stepinski. A spatial impulse response based method for determining effective geometrical parameters for spherically focused transducers. *Ultrasonics*, 40(1-8):307 – 312, 2002.

[160] M. Xu and L. V. Wang. Photoacoustic imaging in biomedicine. *Review of Scientific Instruments*, 77(041101), 2006.

[161] M. Xu and L.V Wang. Limited-view thermoacoustic tomography. In *Proceedings of the Second Joint EMBS/BMES Conference*, volume 2, pages 937–938, 2002.

[162] M. Xu and L.V Wang. Time-domain reconstruction for thermoacoustic tomography in a spherical geometry. *IEEE Transactions on Medical Imaging*, 21:814–822, 2002.

[163] M. Xu, Y. Xu, and L.V Wang. Time-domain reconstruction algorithms and numerical simulations for thermoacoustic tomography in various geometries. *IEEE Transactions on Biomedical Engineering*, 50:1086–1099, 2003.

[164] Y. Xu, D. Feng, and L. V. Wang. Exact frequency-domain reconstruction for thermoacoustic tomography: I. Planar geometry. *IEEE Transactions on Medical Imaging*, 21:823–828, 2002.

[165] Y Xu and L. V. Wang. Universal back-projection algorithm for photoacoustic computed tomography. *Physical Review E*, 71(016706), 2005.

[166] Y. Xu and L.V Wang. Effects of acoustic heterogeneity in breast thermoacoustic tomography. *IEEE Transactions on Ultrasonics, Ferroelectrics, and Frequency Control*, 50:1134–1146, 2003.

[167] Yuan Xu and Wang L.V. Rhesus monkey brain imaging through intact skull with thermoacoustic tomography. *Ultrasonics, Ferroelectrics and Frequency Control, IEEE Transactions on*, 53(3):542 –548, march 2006.

[168] Yuan Xu and L.V. Wang. Effects of acoustic heterogeneity in breast thermoacoustic tomography. *Ultrasonics, Ferroelectrics and Frequency Control, IEEE Transactions on*, 50(9):1134 –1146, sept. 2003.

[169] Zhun Xu, Changhui Li, and Lihong V. Wang. Photoacoustic tomography of water in phantoms and tissue. *Journal of Biomedical Optics*, 15(3):036019–036019–6, 2010.

[170] Zhun Xu, Quing Zhu, and Lihong V. Wang. In vivo photoacoustic tomography of mouse cerebral edema induced by cold injury. *Journal of Biomedical Optics*, 16(6):066020–066020–4, 2011.

[171] Xinmai Yang, Meng-Lin Li, and Lihong V. Wang. Ring-based ultrasonic virtual point detector with applications to photoacoustic tomography. *Applied Physics Letters*, 90(25):251103, 2007.

[172] Xinmai Yang and Lihong V. Wang. Monkey brain cortex imaging by photoacoustic tomography. 13(4):044009, 2008.

[173] Lei Yao and Huabei Jiang. Enhancing finite element-based photoacoustic tomography using total variation minimization. *Appl. Opt.*, 50(25):5031–5041, Sep 2011.

[174] J. Ylitalo, J. Kaovukangas, and J. Oksman. Ultrasonic reflection mode computed tomography through a skullbone. *IEEE Transactions on Biomedical Engineering*, 37:1059–1065, 1990.

[175] J. Ylitalo, J. Koivukangas, and J. Oksman. Ultrasonic reflection mode computed tomography through a skullbone. *Biomedical Engineering, IEEE Transactions on*, 37(11):1059–1066, Nov 1990.

[176] Zhen Yuan and Huabei Jiang. Three-dimensional finite-element-based photoacoustic tomography: Reconstruction algorithm and simulations. *Medical Physics*, 34(2):538–546, 2007.

[177] Zhen Yuan, Qizhi Zhang, and Huabei Jiang. Simultaneous reconstruction of acoustic and optical properties of heterogeneous media by quantitative photoacoustic tomography. *Optics Express*, 14(15):6749–6754, Jul 2006.

[178] Baida Zhang, Shuai Xu, Feng Zhang, Yuan Bi, and Linqi Huang. Accelerating matlab code using gpu: A review of tools and strategies. In *Artificial Intelligence, Management Science and Electronic Commerce (AIMSEC), 2011 2nd International Conference on*, pages 1875 –1878, aug. 2011.

[179] Jin Zhang, Kun Wang, Yongyi Yang, and Mark A. Anastasio. Simultaneous reconstruction of speed-of-sound and optical absorption properties in photoacoustic tomography via a time-domain iterative algorithm. volume 6856. SPIE, 2008.

[180] Y. Zhulina. Optimal statistical approach to optoacoustic image reconstruction. *Applied Optics*, 39:5971–5977, 2000.

[181] Y. Zou, X. Pan, and M. Anastasio. Data truncation and the exterior reconstruction problem in reflection-mode tomography. In *IEEE Nuclear Science Symposium Conference Record*, volume 2, pages 726–730. IEEE, 2002.